LA-UR-15-28829
Approved for public release; distribution is unlimited.

Title: Fission Fragment Mass Distributions and Total Kinetic Energy Release of 235-Uranium and 238-Uranium in Neutron-Induced Fission at Intermediate and Fast Neutron Energies

Author(s): Duke, Dana Lynn

Intended for: Fission Fragment Mass Distributions and Total Kinetic Energy Release of 235-Uranium and 238-Uranium in Neutron-Induced Fission at Intermediate and Fast Neutron Energies, Colorado School of Mines PhD Thesis

Issued: 2015-11-12

FISSION FRAGMENT MASS DISTRIBUTIONS AND TOTAL KINETIC ENERGY RELEASE OF 235-URANIUM AND 238-URANIUM IN NEUTRON-INDUCED FISSION AT INTERMEDIATE AND FAST NEUTRON ENERGIES

by

Dana L. Duke

A thesis submitted to the Faculty and the Board of Trustees of the Colorado School of Mines in partial fulfillment of the requirements for the degree of Doctor of Philosophy (Applied Physics).

Golden, Colorado

Date _____

Signed: _____
Dana L. Duke

Signed: _____
Dr. Uwe Greife
Thesis Advisor

Signed: _____
Dr. Fredrik Tovesson
Thesis Advisor

Golden, Colorado

Date _____

Signed: _____
Dr. Jeff Squier
Professor and Head
Department of Physics

ABSTRACT

This Ph.D. dissertation describes a measurement of the change in mass distributions and average total kinetic energy ($\overline{TKE}$) release with increasing incident neutron energy for fission of ^{235}U and ^{238}U. Although fission was discovered over seventy-five years ago, open questions remain about the physics of the fission process. The energy of the incident neutron, E_n, changes the division of energy release in the resulting fission fragments, however, the details of energy partitioning remain ambiguous because the nucleus is a many-body quantum system. Creating a full theoretical model is difficult and experimental data to validate existing models are lacking. Additional fission measurements will lead to higher-quality models of the fission process, therefore improving applications such as the development of next-generation nuclear reactors and defense. This work also paves the way for precision experiments such as the Time Projection Chamber (TPC) for fission cross section measurements and the Spectrometer for Ion Determination in Fission (SPIDER) for precision mass yields.

The dissertation discusses the motivations and underlying theory behind the study of fission. It also contains a description of the detector, a twin Frisch-gridded ionization chamber, and the neutron source at the Los Alamos Neutron Science Center (LANSCE) Weapons Neutron Research (WNR), which provides neutrons from the intermediate to fast region (E_n = 100's of keV to 100's of MeV). The double energy (2E) analysis procedure is also described, which calculates fragment masses and energies pre- and post-prompt neutron emission. The results of these studies reveal clear structure in the energy-dependent $\overline{TKE}$ and its variance σ_{TKE} for both uranium isotopes that correlate to multi-chance fission in the cross section. A low E_n turnover in the $\overline{TKE}$ was observed for ^{235}U which had only been hinted at in previous experiments. Correlated TKE and masses are also presented.

TABLE OF CONTENTS

LIST OF FIGURES

LIST OF TABLES

ACKNOWLEDGMENTS

There's no "I" in team so I send a loud shout-out of thanks the the Fission Team: Fredrik, Rhiannon, Krista, Denise, Brett, Dan, Dmitriy, and Verena. Without their hard work and support, this work would not have been successful. Thanks for everything!

I also wish to thank the good people of Los Alamos National Laboratory, LANSCE, and my group, P-27, for the generous hospitality, ice cream, and the neutrons.

Thanks to my awesome parents for taking me on so many great adventures down the roads less traveled.

I am grateful to my teachers and mentors throughout my career, especially Joan Lachowsky, Bret Clark, Paul Choboter, and Jennifer Klay. My deepest gratitude from the bottom of my heart I owe to Fredrik Tovesson, my mentor and friend. Being your student has been an honor.

I would also like to thank the Pajarito Mountain Ski Patrol for the good company and the Los Alamos Historical Society for all the interesting old time Los Alamos stories.

Thanks to my many friends from the Colorado School of Mines. I look forward to many years of friendship with you all.

Finally, I thank my esteemed colleague, good friend, ski instructor, and power lifting coach - Verena Kleinrath. You're the bestest!

For the coolest parents: Terri and Don Duke

CHAPTER 1

INTRODUCTION

The process of nuclear fission, where a nucleus splits typically into two fragments, is important for many applications including energy, defense, non-proliferation, and nuclear medicine. Behind these applications are engineering codes that rely on accurate nuclear data evaluations of energy release, mass yields, cross sections and other observables [1]. Neutron-induced fission behavior evolves with increasing incident neutron energies. It is surprising that over seventy-five years after the initial discovery of fission [2], there is still a lack of experimental data for the major actinides at some neutron energies relevant to applications.

The reason to provide new fission data at high neutron energies is two-fold. First, twenty-first century fission models make predictions which require experimental validation, thereby increasing our understanding of the fission process which is a complex, many-body quantum problem. Second, we wish to add to and improve data for nuclear applications. For example, Generation IV fast nuclear reactor technology relies on increased energy output from fission induced by neutrons in the fast region (hundreds of keV to hundreds of MeV).

The average total kinetic energy release ($\overline{TKE}$), which is the sum of the kinetic energies of the two fission fragments, is an essential piece of nuclear data for determining the energy output in nuclear technology. It has been known for many years that the $\overline{TKE}$ carries away the largest amount of energy in fission, about 170 MeV for isotopes of uranium [3]. However the $\overline{TKE}$ changes with incident neutron energy. For ^{235}U, $\overline{TKE}$ measurements exist for incident neutron energies under 9 MeV plus recent measurements extending to high energies with unfortunately large uncertainties [4] [5] [6]. For ^{238}U, most published measurements available are at neutron energies below 7 MeV, however, one continuous data set exists in an unpublished Ph.D. thesis covering E_n =1-400 MeV [7] [8] [9]. The present work addresses

the gaps and uncertainties in the existing data by providing a continuous $\overline{TKE}$ measurement covering the neutron energy range from 0.2 - 30 MeV for both ^{235}U and ^{238}U.

The masses of the fission fragments are also an important quantity for applications and theoretical models. A mass yield is the probability of finding a particular fission product normalized over a large number of fission events. Since fission is a random quantum process, the mass splits over a range of values. The mass yield follows a double-humped distribution, typically displaying a heavy and a light peak. As incident neutron energy increases, a symmetric component in the distribution becomes more prominent, but the mechanisms by which this process evolves are not well measured or understood. For example, evaluations of fission product yields for ^{235}U are available at thermal, 1-2 MeV, and 14 MeV and for ^{238}U are available at 1-2 MeV, and 14 MeV [10]. These are based on radio-chemical methods using mass spectrometry, decay information, and half-life measurements to deduce earlier isotopic concentrations. Direct measurements using nuclear physics detectors exist at low incident neutron energies only. Again, this present work will provide an evolution of the mass yields for both uranium isotopes over neutron energies from 0.2 - 30 MeV. Finally, the correlations between the fission fragment masses and kinetic energies are discussed to try to establish a more complete picture of energy release in fission.

Chapter 2 is a presentation of the relevant aspects in fission theory as it relates to mass yields and average total kinetic energy release and a brief discussion of motivation for this study. Current models for $\overline{TKE}$ and masses are also discussed, including the experimental context for this work. The experimental method using a Frisch-gridded ionization chamber at a neutron source at Los Alamos National Laboratory is described in Chapter 3. The double energy (2E) method used to determine the final fission fragment masses and $\overline{TKE}$ is discussed in Chapter 4. While the 2E method has been used in previous work, it was expanded to include multi-chance fission and simulated neutron correction methods novel to this work. Chapter 5 contains the final physics results with a discussion and comparison to previous work. Chapter 6 summarizes what we learned from this overview study of the

evolution of fission observables with neutron energy.

CHAPTER 2
FISSION THEORY

Fission has been studied extensively for over seventy-five years and is used in many applications, but there is still much to learn about the fission process both from an experimental and theoretical standpoint. Section 2.1 presents how fission works, defines some vocabulary, and describes at how nuclear theory first explained fission. In Section 2.2, we will discuss more modern methods of fission theory developed after the 1970's. Section 2.3 focuses on empirical models of total kinetic energy in Subsection 2.3.1 and fission mass yields in Subsection 2.3.2. Throughout the chapter, the motivation for the work in this thesis emerges: fission models and theory need more exact data to validate theories and benchmark simulations.

Measurements of relevant fission observables are used as input in empirical fission models, to benchmark theories, and as parameters in nuclear data evaluations which are used in a wide array of applications. The need for greater accuracy in the modeling and simulations of both civil and defense fission applications calls for new experimental data to be generated [11]. The civil applications need improved nuclear data to drive more exact design parameters for nuclear reactors, increasing energy efficiency and decreasing the amount of waste. Advanced modeling of military nuclear devices helps to understand the aging stockpile.

The study of multiple chance fission is a particular area where additional data at high energies would serve fission models. First chance fission is the basic picture of neutron-induced fission described in Section 2.1. Second chance fission occurs at higher incident neutron energies when the incident neutron is evaporated during fission, causing a sudden jump in the cross section [1]. At higher energies, third and fourth chance fission are possible reaction channels. The thresholds for these reactions are dependent on the isotope and shape of the fission barrier. This work seeks to understand what influence multiple chance fission has on fission observables.

2.1 Fission Fundamentals

In 1939, Meitner and Frisch explained the experimental observations of their colleagues, Hahn and Strassman, where barium was discovered following the disintegration of a uranium nucleus [2] [12]. This process by which a nucleus divides typically into two heavy fragments was named fission [2]. A formal, theoretical treatment of the nucleus as a droplet of charged liquid was developed soon afterward by Bohr and Wheeler [13].

In neutron-induced fission, a neutron is absorbed into a nucleus, transferring energy into the system. The compound nucleus deforms and becomes unstable. At about 10^{-20} s after neutron impact, the nucleus divides typically into two excited fission fragments. This point in time is referred to as the scission point. The fragments accelerate away from each other due to Coulomb repulsion with a large amount of kinetic energy, on order of 200 MeV. Most of the energy released in fission is in the form of kinetic energy. The fragments deexcite further by emitting prompt neutrons and gamma rays, becoming primary fission products during the 10^{-18} to 10^{-7} s following neutron impact [14]. Prompt emission accounts for about 10 MeV of energy release. Further β-decay and occasional delayed neutron emission occurs as the fission products decay toward stability. These are called secondary fission products. Because of the very short time scales of scission and deexcitation, only the primary and secondary fission products can be directly detected with experimental equipment. A diagram of the fission process and associated vocabulary is shown in Figure 2.1.

The vast majority of the energy release in fission is transferred into kinetic energy of the light and heavy fragments, conserving energy and momentum. The rough partitioning of the energy is dependent on the mass split between the light and heavy fragment. The asymmetry of the fragments is explained by nuclear shell structure, which favors certain energy-minimizing nucleon configurations like nuclear magic numbers [14]. Furthermore, due to the large assembly of nucleons and the quantum mechanical nature of nucleon-nucleon interactions, a large number of fission exit channels are opened leading to a distribution of mass splits for fission of a given isotope at a specific excitation energy. As excitation energy

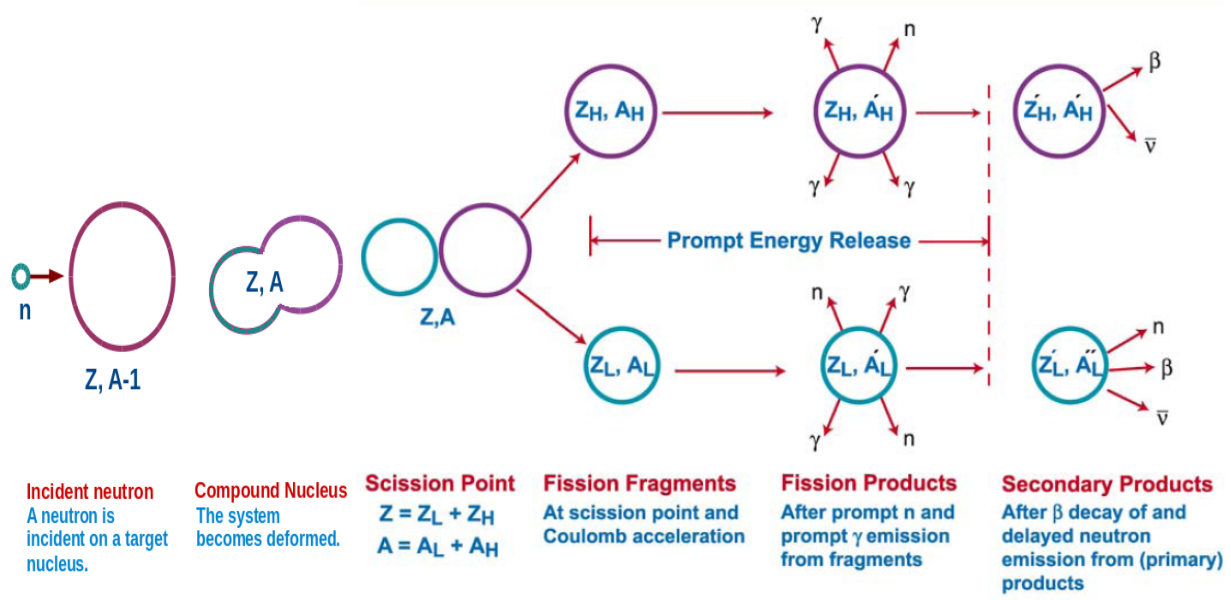

Figure 2.1: The evolution of energy release during the fission process is illustrated from the point of neutron impact to the decay into secondary fragments. Taken from [15] with additions made for incident neutron and compound nuclear stages.

increases, the mass splits become more symmetric because the nuclear shell effects that favor asymmetric exit channels become less important as shown in Figure 2.2. More information on the physics of mass splits is provided in Section 2.3.2.

As the fragment masses vary according to a probability distribution, so does the total kinetic energy release. The total kinetic energy is the sum of the light and heavy fragments' kinetic energies. The average total kinetic energy ($\overline{TKE}$) is an average over all possible mass splits. The $\overline{TKE}$ and fragment mass distributions are difficult to calculate theoretically, which is further explored in 2.3.1.

Before proceeding to modern fission theories, consider the following treatment of the distribution of energies and fission fragments based on simple energy conservation. The following derivation demonstrates how energy is partitioned in the compound nuclear system on to the fission fragments in first-chance neutron induced fission (adapted from [15] and [16]). Consider the reaction ${}^{A-1}_{Z}X(n,f)$. From conservation of charge and baryon number, we establish that $A = A_H + A_L$ and $Z = Z_H + Z_L$, where the subscripts represent the

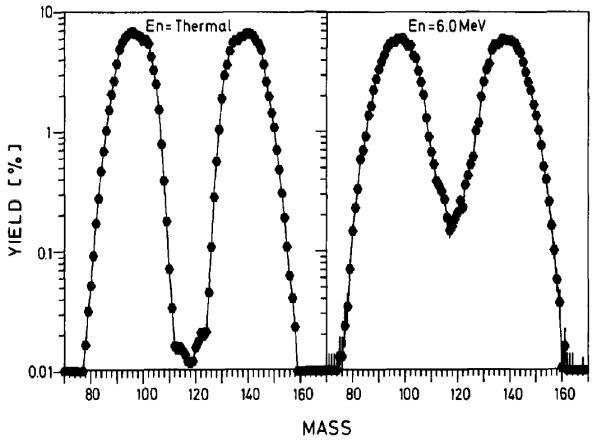

Figure 2.2: As the incident neutron energy increases, the model predicts the filling of the valley between the light and heavy mass peaks as the fission fragments become more symmetric [5].

number of nucleons and protons in the heavy and light fragments respectively. Also suppose that following scission the fully accelerated fragments have kinetic energy T_H and T_L. From conservation of energy between the neutron with mass m_n and kinetic energy E_n, target nucleus with mass $M(Z, A-1)$, and resulting compound nuclear system of kinetic energy T and excited state mass $M^*(Z, A)$, we write:

$$E_n + m_n + M(Z, A-1) = T + M^*(Z, A) = T_H + M^*_H(Z_H, A_H) + T_L + M^*_L(Z_L, A_L), \quad (2.1)$$

with the assumption that $c^2 = 1$. We can also write that the binding energy, B_n, of the neutron is equal to the Q-value of the neutron capture reaction in the form,

$$m_n + M(Z, A-1) = M(Z, A) + B_n. \quad (2.2)$$

Substituting into equation 2.1 we get,

$$E_n + B_n + M(Z, A) = T_H + M^*_H(Z_H, A_H) + T_L + M^*_L(Z_L, A_L), \quad (2.3)$$

where the masses are excited and can be expressed in terms of the ground state mass and the excitation energy i.e. $M^* = M + E^*$. Equation (3) can be modified into

$$E_n + B_n + M(Z,A) = T_H + M_H(Z_H, A_H) + E^*_H(Z_H, A_H) + T_L + M_L(Z_L, A_L) + E^*_L(Z_L, A_L). \tag{2.4}$$

We know the energy release in fission is due to breaking up the binding energy of the nucleons in the nucleus, which can be expressed mathematically as the difference between the ground state mass and the masses of the fission fragments,

$$E_r = M(Z,A) - M_H(Z_H, A_H) - M_L(Z_L, A_L) \tag{2.5}$$

Combining with the equation 2.4, we can recover the energy release in fission in terms of the properties of the fission fragments.

$$E_r = T_H(Z_H, A_H) + T_L(Z_L, A_L) + E^*_H(Z_H, A_H) + E^*_L(Z_L, A_L) - (E_n + B_n) \tag{2.6}$$

Thus, we have shown that the energy release in fission is distributed in the kinetic (TKE) and excitation energies (E^*) of the fission fragments,

$$TKE = T_H(Z_H, A_H) + T_L(Z_L, A_L), \tag{2.7}$$
$$E^* = E^*_H(Z_H, A_H) + E^*_L(Z_L, A_L). \tag{2.8}$$

Note that both of these equations depend on the $A_{H,L}$ and $Z_{H,L}$ of the light and heavy fragment, but because fission is a quantum mechanical process, for a single E_n, multiple $A_{H,L}$ and $Z_{H,L}$ are possible. Thus, TKE and E^* must be considered as an average over all possible mass splits, which are the physical observables. Then the average total kinetic energy, can be expressed mathematically as

$$\overline{TKE} = \frac{\sum[Y_f][T_L(Z_L, A_L) + T_H(Z_H, A_H)]}{\sum Y_f}, \tag{2.9}$$

where the sums are over the light and heavy fragment yields, Y_f. This experiment seeks to measure the total average kinetic energy ($\overline{TKE}$) part of the energy release along with the fragment masses, A_H and A_L. These quantities are difficult to calculate theoretically, but

many advances have been made since the discovery of fission, discussed in the next section.

2.2 Modern Fission Theory

Initially, fission was described theoretically by treating the nucleus as a charged liquid drop [13]. According to the liquid drop model, a spherical nucleus is deformed into an ellipsoid when excited, for example by absorbing a neutron, increasing the excitation energy of the compound nuclear system. The empirical binding energy is calculated for the new shape of the compound nucleus and compared to the initial state. If further deformation causes an energy gain, fission is expected to occur [17]. With this simple model, a rudimentary fission barrier can be predicted, which captures the behavior of many aspects of fission but ignores quantum mechanical effects. A schematic of the fission barrier predicted by the liquid drop model is shown to the left in Figure 2.3.

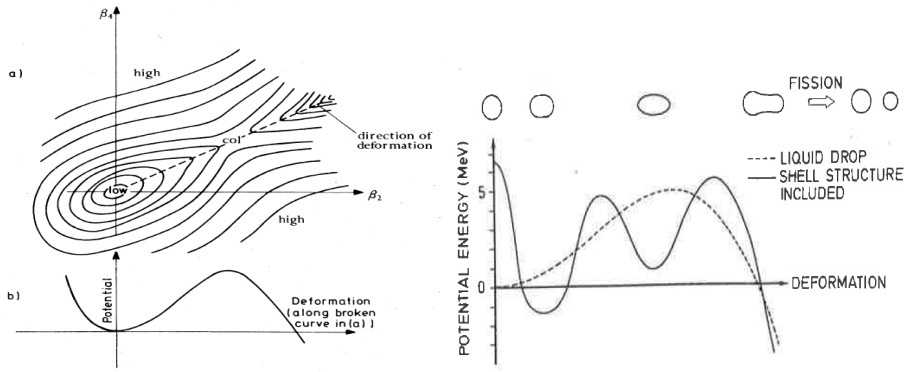

Figure 2.3: (Left) a) The potential energy contours of a fissionable nucleus as a function of the quadrupole and hexadecapole deformation parameters. These parameters are analogous to the lengths of two different axes for an ellipse of rotation. b) The potential energy along the minimum energy trajectory for increasing elongation. [18] (Right) The liquid drop model compared with the double hump fission barrier which arises when nuclear shell effects are considered. [14]

The Liquid-Drop Model fails to explain the asymmetry of fission fragments, revealing the need for a more complete theoretical description of fission. Many techniques have been developed to handle this complicated quantum problem. In 1953, a quantum description of fission was developed by Hill and Wheeler, which considered single-particle interactions us-

ing the generator-coordinate method [19]. A single-particle model for deformed nuclei that incorporated angular momentum and parity was developed by Nilsson in the mid 1950's [20], [21]. In the 1960's, Strutinsky found a way to extend this model to find a correction to the liquid-drop model which accounted for the quantum mechanics of a deformed potential [22],[23]. His methodology is referred to as a macroscopic-microscopic model because it combines bulk, macroscopic deformation energy of the compound nucleus as calculated by the liquid-drop model, with microscopic quantum effects from the individual nucleon wavefunctions. When both contributions are incorporated, one may deduce a double-humped fission barrier for elements like uranium and plutonium, as shown in Figure 2.3 [18]. This method is computationally involved and the partial consideration of two or three deformation degrees of freedom was all that was possible with the computing technology of the 60's and 70's. It was only in the 1990's that the macroscopic-microscopic method could be applied in a more complete way to several nuclear shape degrees of freedom.

The two main approaches of modern fission theories are macroscopic-microscopic and microscopic. Macroscopic theory incorporates bulk behaviors of nuclear systems, balancing repulsive electrostatics and attractive nuclear forces. Microscopic effects, as modeled by the Strutinsky procedure, add quantum effects such as the change of the nuclear level ordering and spacing as a function of nuclear deformation. The two approaches are combined to generate multi-dimensional potential-energy surfaces [24]. Recent developments of macroscopic-microscopic models led to a more detailed understanding of fission barriers, as shown in Figure 2.4 [25] [26]. Advances in computing have allowed further development of the generator coordinate methods of the 1950's in advanced macroscopic-microscopic models of today. Microscopic models have also been developed; examples are found in references [27] [28]. Both macroscopic-microscopic and fully microscopic models are in need of nuclear data to test predictions, particularly at a wide range of incident neutron energies to study how the fission process evolves with increasing excitation energy.

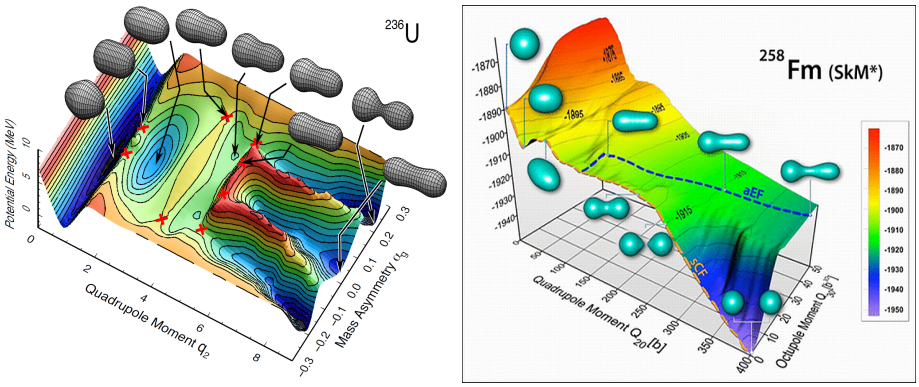

Figure 2.4: (Left) An example of a modern fission model using a combination macroscopic-microscopic technique to calculate potential fission surfaces from [25]. (Right) Microscopic models can also be used to predict potential surfaces [29]. `http://ascr-discovery.science.doe.gov/shared/ns_energy_surface.html`

The macroscopic-microscopic method provides potential-energy surfaces (PES) which can be combined with dynamical effects to lead to models which are practical to implement using modern computing technology. Such models can predict fission fragment mass and kinetic energy distributions. One particular model, the Los Alamos Dynamical Fission Model (LADFM), starts with a small number of physical parameters that can be tuned to match experimental yield data at low incident neutron energies, and can then be used to predict outcomes for increasing neutron energies. The necessary inputs for the calculation are are nuclear shape at the outermost saddle point, determined from the PES calculations, inertia and dissipation tensors, which lead to Langevin equations for the dynamics, and starting distributions for momenta at the saddle point, derived assuming thermodynamic equilibrium. Monte-Carlo solutions of the Langevin equations lead to an ensemble of trajectories, which may be evaluated statistically to predict correlated fragment masses and kinetic energies [30]. Extending this model, guided by new data, could improve predictive capabilities.

2.3 TKE and Yield Models

Modern theoretical models need experimental data to test their validity. Unfortunately, existing fission data for higher incident neutron energies is sparse or nonexistent, depend-

ing on the isotope. What data do exist are subject to uncertainties at a level which is unacceptably large for benchmarking twenty-first century models describing defense- and energy-related applications. A survey of nuclear data concluded that additional measurements were needed to support applications and theoretical advances [11], particularly average $\overline{TKE}$ and fission fragment yields.

2.3.1 Average Total Kinetic Energy

One goal of this work was to measure the $\overline{TKE}$ release in neutron-induced fission of ^{235}U and ^{238}U covering a broad range of incident neutron energies, from thermal to 30 MeV. In a 2006 paper on total prompt energy release in fission, D.G. Madland cited a need for more complete $\overline{TKE}$ measurements [15]. For ^{235}U(n,f), additional information was requested over the incident neutron energy range of 10 keV $\leq E_n \leq$ 30 MeV, as the existing $\overline{TKE}$ data stops at about 9 MeV and includes large uncertainties. The emipirical model is based on a linear fit to the data from sources [5] and [4]. Both these measurements were done with an ionization chamber at a quasi-monoenergetic Van de Graaf accelerator based neutron source.

While data exists across a wide incident neutron energy range (1 - 400 MeV) for ^{238}U, measurement with an ionization chamber detector will improve the energy resolution and test previous results. The existing measurements were made with silicon surface barrier detectors, which have a higher pulse height defect. This detector effect adds an additional uncertainty of around 1-3% [31] compared with an ionization chamber which has an uncertainty of about 0.5-1% [32]. Measurements available below $E_n = 7$ MeV were made with ionization chambers at quasi-monoenergetic neutron sources [33] [34] and deviate less than 2% from the data in [7]. Additional ^{238}U data will add new data to previous measurements and reduce uncertainties both in $\overline{TKE}$ by use of the ionization chamber and in E_n by operating at a white neutron source (100's keV to 100's MeV).

Due to the lack of available data and large uncertainties in the current ^{235}U $\overline{TKE}$ measurements, Madland fit the distribution linearly, though some structure is clearly discernible

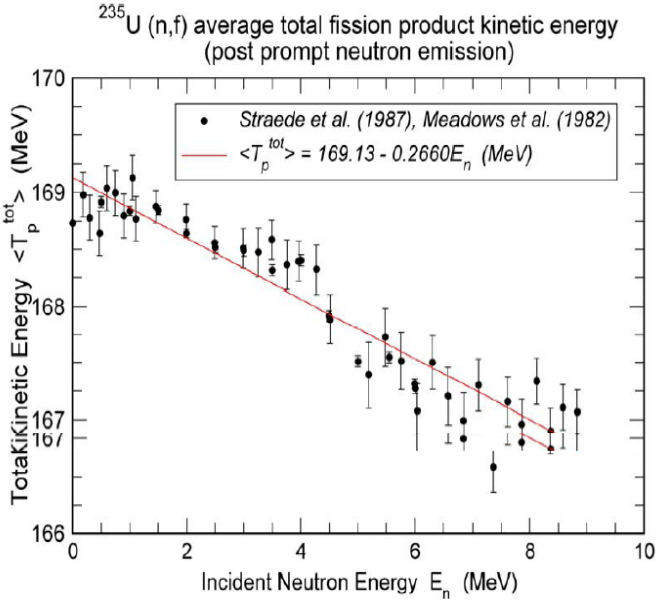

Figure 2.5: The existing average TKE data for ^{235}U is insufficent to model the behavior of multichance fission, though some structure is visible in the data [15] [5] [4].

in Figure 2.5. Recognizing that the linear fit was not ideal, Madland recommended that future users of his derived model restrict use to $E_n < 9$ MeV [15]. The ^{238}U data was fit with a quadratic, though the data set appeared to have some structure [7]. A more recent evaluation of the data by Lestone in [35] accounts for multi-chance fission by using the slope of the Madland line, but shifting the starting position in E_n to multi-chance fission thresholds. The idea behind this approach is that during multi-chance fission, one or more neutrons are emitted from the excited compound nucleus, lowering its excitation energy and causing the resulting fission fragments to behave as though they came from a much colder system, initially raising the TKE at the threshold, but then lowering it again until the next threshold is reached. This causes, Lestone assumed, structure in the TKE, but previous measurements were not sufficient to resolve any structure. By performing our $\overline{TKE}$ measurement, we have extended the energy range and thereby reveal more of the structure in the $\overline{TKE}$ distributions, ultimately contributing to a better understanding of multiple chance fission [35]. These data will also be used as input in current fission models [36].

2.3.2 Mass Yield Distributions

By measuring fission fragment mass distributions, we can add significantly to the existing data, which is only available at incident neutron energies in the thermal, 14 MeV region, and sparse points in between for the major actinides, as noted in the England and Rider fission product yield evaluation [10]. A global measurement of how these distributions evolve with increasing neutron energy does not exist. Rather, evaluations rely on many measurements made with both direct and radio-chemical methods. A study of mass distributions over the wide range of neutron energies considered by this experiment can provide a rigorous test of existing fission models [37], shown in Figure 2.6, which are tuned to the low neutron energy evaluations [1]. Modern attempts at fission models also base their predictions of mass yields [25] predominantly at lower incident neutron energy data and the lack of data at higher energies makes a test of their extrapolations difficult.

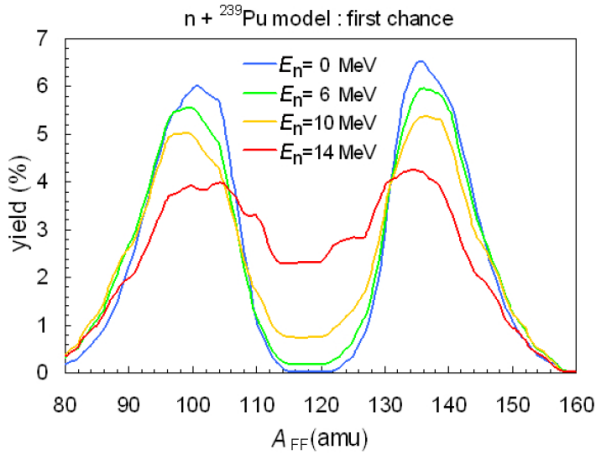

Figure 2.6: Existing measurements at thermal neutron energies are scaled up in this model of first-chance neutron-induced fission for ^{239}Pu from [37]. Independent yield data above 14 MeV is not available for Pu or U isotopes, so models at higher energies cannot be benchmarked.

Recent work on ^{238}U mass distributions has been done at the quasi-monoenergetic neutron beam of the Louvain-la-Neuve cyclotron facility, CYCLONE, at incident neutron energies of 33, 45, and 60 MeV using a gridded ionization chamber [38]. These results were compared

with data collected at the Los Alamos Weapons Neutron Research Facility (WNR) in 1995 using silicon surface barrier detectors, published in the Ph.D. thesis of Zöller [7]. Studies of ^{238}U fission properties were also performed using an ionization chamber in the low $E_n < 7$ MeV [34] [8].

2.3.3 Fission Data Efforts

This experiment using a Frisch-gridded ionization chamber (FGIC) has to be seen in context with other experimental approaches in fission research that are currently being pursued. To achieve a more complete understanding of the fission process, two major experimental campaigns are currently in place. Their goals are respectively:

- Low efficiency approach yielding high resolution mass measurements
- High efficiency approach yielding high precision fission cross sections and low resolution mass measurements

The SPectrometer for Ion DEteRmination (SPIDER) is the experimental effort to provide very precise measurements at particular incident neutron energies [39]. The second approach, this work combined with the fission Time Projection Chamber (fissionTPC) measurement, will provide a more general picture of how the fission process evolves with neutron energy [40]. The work with the FGIC constitutes a middle way using the unique beam capacities and energy range at LANSCE to produce results faster than they can be expected from the more complicated approaches. By operating the traditional ionization chamber under the same experimental conditions as the fissionTPC, the results will add credibility to future fissionTPC findings. By utilizing multiple detection methods, we increase our understanding of fission on both general and fine scales. The complementary detector approaches are shown in Figure 2.7.

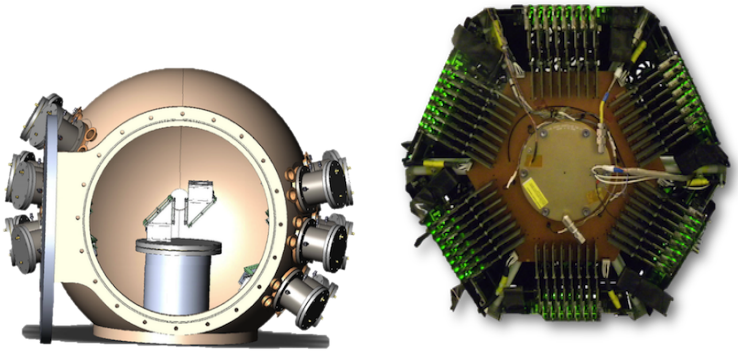

Figure 2.7: The fission Time Projection Chamber (right) and SPIDER (left) are two novel instruments being used to investigate fission cross sections and fission product yields to unprecedented precision. This work with established technology supports the missions of SPIDER and TPC's novel detection methods and adds credibility to their findings.

CHAPTER 3
EXPERIMENTAL METHOD

Measurements of uranium fission properties were made by impinging a beam of neutrons on an uranium target contained inside a Frisch-gridded ionization chamber (FGIC). Signals generated by the resulting uranium fission products were collected via a waveform digitizer data acquisition (DAQ) system. Two separate experiments were carried out, each using a different isotope of uranium and different DAQ configuration. Additional logistical details about the two experiments are provided in Section 3.1. The two uranium targets are described in 3.2. The FGIC operating principles and hardware design are discussed in Section 3.3. The neutron source and flight path are described in Section 3.5. Finally, digital data acquisition systems and waveform processing is described in 3.4.

3.1 Logistics

Two separate experiments were performed, each using a different isotope of uranium as the target and different digitizers in the DAQ. Both experiments used the same Frisch-gridded ionization chamber (FGIC), gas system, preamplifiers, and were operated at the same neutron source, Los Alamos Neutron Science Center - Weapons Neutron Research (LANSCE-WNR). Both experiments went through a selection process and were awarded beam time by the LANSCE Program Advisory Committee based on scientific merit.

The ^{238}U Frisch-gridded ionization chamber (238-FGIC) experiment ran from November 15$^{\text{th}}$ to December 15$^{\text{th}}$, 2012, under LANSCE Proposal number NS-2012-4063-A. The 238-FGIC experiment was done in collaboration with colleagues from Los Alamos National Laboratory and the Joint Research Centre Institute for Reference Materials and Measurements (IRMM-JRC) in Geel, Belgium. The IRMM-JRC collaborators provided the detector, supporting electronics, gas system, ^{238}U target, data acquisition (DAQ) system, and computers. The experiment was operated in Los Alamos at LANSCE-WNR flight path 90L.

After the experiment, the DAQ system and computers were shipped back to Belgium for other work. The FGIC and supporting hardware remained in Los Alamos.

The ^{235}U Frisch-gridded ionization chamber (235-FGIC) experiment ran from September 16$^{\text{th}}$ to October 14$^{\text{th}}$, 2013, under LANSCE Proposal number NS-2013-4720-A. It was operated at LANSCE-WNR by Los Alamos personnel. During this run, computers and a new DAQ system were provided by LANL. The cathode plate, a component of the FGIC, was redesigned and built by LANL to accommodate the ^{235}U target provided by Oregon State University. This version of the full experimental setup is described in our recent paper [41].

The FGIC and supporting hardware are discussed in the next section, which includes all modifications. Both configurations of the DAQ system are presented in 3.4. A suite of data analysis programs was developed for the 238-FGIC data and then applied to the 235-FGIC data with some modifications at Los Alamos from February 2013 to the present. The analysis is presented in detail in Chapter 4. Photos taken of the chamber during the 238-FGIC and 235-FGIC runs are shown in Figure 3.1.

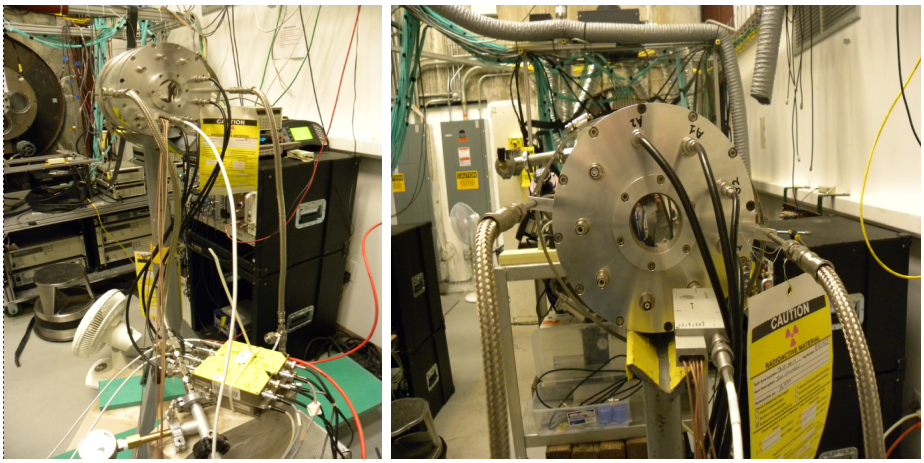

Figure 3.1: (Left) A photograph of the ionization chamber in the WNR flight path during FGIC-238. Preamp bundle and gas pressure gauge are also shown. This experiment was parasitic and ran behind the Time Projection Chamber (electronics stand and optical fibres pictured). Part of the steel shutter is pictured in the background. (Right) Face of the chamber during FGIC-235. The cathode preamp is attached directly to the BNC output at 5 o'clock. Gas lines protrude from the 3 o'clock and 9 o'clock positions.

3.2 Targets

Thin deposits of uranium were applied on thin backings via vacuum deposition. The targets and backings must be thin in order to 1) minimize energy loss and 2) allow both fission fragments to escape into the detector.

The ^{235}U target for 235-FGIC is similar in construction to the target design for the fissionTPC [42], and was made by collaborators at Oregon State University (OSU). A 99.9+% pure uranium oxide is converted to a tetrafluoride by dissolution in HF. An approximately 2 cm diameter spot of target material (1045 μg) is vacuum deposited onto a thin (100 μg/cm^2) carbon film mounted on a 4 cm diameter aluminum ring, which is attached to the cathode plate.

The 238-FGIC ^{238}U target was made by collaborators at the Joint Research Centre Institute for Reference Materials and Measurements (JRC - IRMM) and is similar to the target described in reference [9]. The ^{238}U target is 132 μg/cm^2 $^{238}UF_4$ deposited on a Au-coated (50 μg/cm^2) polyamide backing (35 μg/cm^2).

3.3 Frisch-gridded Ionization Chamber

The twin Frisch-gridded ionization chamber (FGIC) type was named for Otto Frisch, a pioneering fission researcher, and has been a standard tool in the field for decades. This detector type has been used previously for fission measurements with actinide targets [5] [33] [34]. The detector and supporting hardware will be discussed in Section 3.3.1. Details on the physics of its operation are presented in Section 3.3.2.

3.3.1 FGIC Hardware

The Frisch-gridded ionization chamber (FGIC) can measure both the energy and emission angle of the coincident fragments through the principles of a gas ionization detector, discussed in [43]. The FGIC design is described in [32], but will be further explained in this section. The FGIC was chosen for this work because it has a high efficiency and good energy resolution (0.5 - 1.0 %), is radiation hard, and has a nearly 4π solid angle coverage. A cartoon and a

photograph of the interior detector components are shown in Figure 3.2.

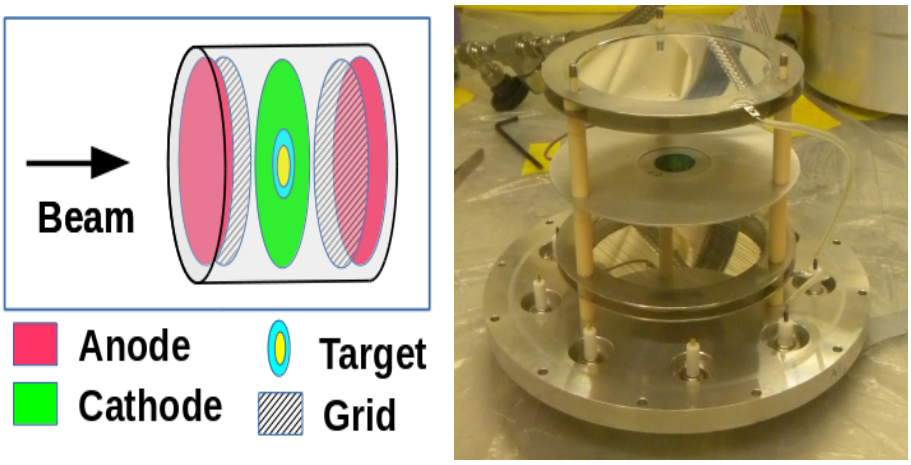

Figure 3.2: Left: Schematic showing the components of a Frisch-gridded ionization chamber (FGIC). Before placing the chamber in beam, a target is inserted into the cathode, the chamber filled with gas, and the appropriate voltage is applied to the anodes, grids, and cathode plates. During the experiment, a neutron beam passes through the chamber and target. Right: A photograph of the ionization chamber components with the mounted ^{235}U target taken inside the glovebox used for target insertion.

The gas-filled chamber contains an anode plate and Frisch grid on either end of the detector. A cathode plate separates the two halves, shown in Figure 3.4. The actinide target is placed in the center of the cathode. An electric field is generated on both sides of the cathode by applying the appropriate voltage to the plates while the grids are grounded. Fission products emitted into both sides of the chamber deposit their energy in the fill gas through ionization. The gas ionization produces charge clouds of ion-electron pairs that we separated by the field and move towards the cathode and grid plates, inducing a current on them which is dependent on the angle of the fission fragment track. When the electron cloud passes the grid, it induces charge on the anode proportional to the fragment's kinetic energy. Additionally, the moving electron cloud and the quasi-stationary ion cloud induce a signal on the Frisch grid which can be used for further analysis. The electrical signals from the plates and grids go to preamplifiers and are then recorded by the data acquisition system.

A schematic of the hardware is shown in Figure 3.3. This FGIC is operated with a P10 (90% argon and 10% methane) fill gas, at 950 torr with a flow rate of less than 100 sccm.

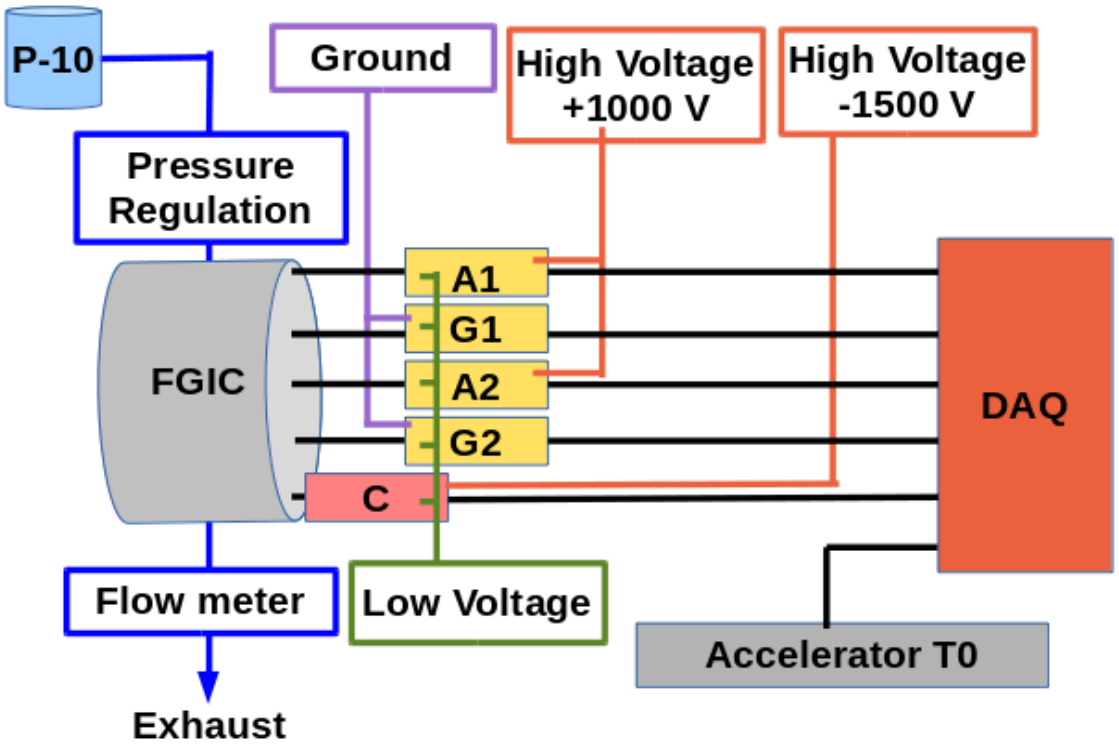

Figure 3.3: A schematic of the Frisch-gridded ionization chamber (FGIC) and supporting hardware. The gas system from P-10 bottle to exhaust is pictured. The power supplies, and preamps for the anodes (A1 and A2), grids (G1 and G2), and cathode (C), are shown with color coded connecting lines indicating where the voltages and signals go. The data acquisition system (DAQ) is shown as a single element which will be further described in Section 3.4.

These settings ensure that the products deposit all of their energy in the gas. The pressure was maintained with a pressure control unit on the inflow side of the chamber. The outflow was controlled with a needle valve on the outflow side. Both the inflow and outflow sides were equipped with one-way flow valves. The outer dimensions of the cylindrical chamber are about 18 cm in diameter and 15 cm in length.

The interior assembly of the detector, pictured in Figure 3.2, is from the bottom up, a stack of anode, grid, cathode, grid, and anode plates. The support pillars are Teflon rods with ceramic spacers separating the plates. Separation distances between the anode to grid and grid to cathode are 7 mm and 31 mm respectively and are shown in the schematic in Figure 3.4. There can be a variation on the order of 1 mm in either distance depending on

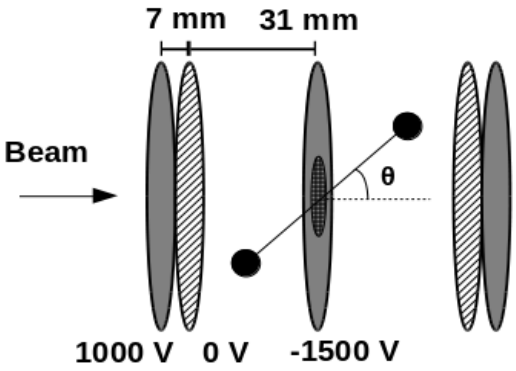

Figure 3.4: Left: A schematic of the ionization chamber interior. Separation distances and voltages of the anodes, grids, and cathode are shown. The beam direction is incident on the upstream sample side of the detector. The backing side is oriented towards the downstream side. The orientation of the fission fragment emission angles θ is indicated with respect to the beam axis.

how the spacers are inserted. The two anodes and center aluminum cathode have an 11 cm diameter. The Frisch grid is an 11 cm diameter outer ring which provides support for a 9 cm diameter wire grid. The parallel grid wires are 0.1 mm diameter with a spacing of about 1 mm. The target insertion and interior plate assembly work was performed inside a glovebox to prevent contamination and keep the system clean.

Two Ortec 495 power supplies provide high voltage through SHV cables to the anodes and cathode. They are operated at 1000V and -1500V respectively. Analog signals were collected off the grid and anode plates and are fed outside of the pressure vessel to BNC feedthroughs where they are connected to Mesytec MPR-1 charge integrating preamplifiers, pictured in Figure 3.5.

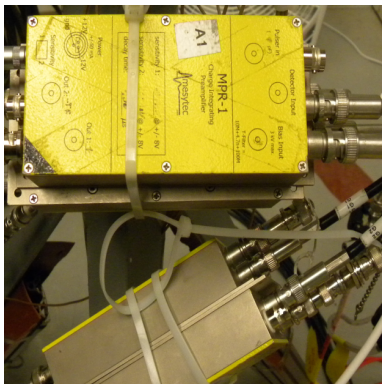

Figure 3.5: The Mesytec charge integrating preamp for an anode (A1), shown with BNC (black) cables, SHV (white) cables, and low voltage (grey) cables. There are four preamps in the bundle, two for the anodes and two for the grids. The grid preamps are terminated on the bias input, since they are at ground potential.

The cathode signal goes through a CSTA 2HV charge sensitive preamplifier, optimized for fast ($<$ 1 nanosecond level) timing. This small preamp is mounted directly to the detector BNC feedthrough. The amplified signals are sent through long BNC cables (about 20 m) to the data acquisition system described in Section 3.4. The preamps are powered by a low voltage (12 V) supply. In FGIC-238, we used the "energy" integrated output from the preamp. This is a large, fast signal which was easily processed by the DAQ. In FGIC-235, we used the "timing" output (short decay constant) from the preamp since the digitizers had a lower sampling rate. The small signal went through a Timing Filtering Amplifying module, shown in Figure 3.9. It increased the size of the bi-polar signal from 50 mV to 0.5 V. The larger amplitude makes it much easier to pick off the position of the cathode timing with will later be used to calculate neutron time of flight and subsequently incident neutron energy in Section 4.1.

The timing signal from the accelerator is also sent from the provided output in the flight path to the DAQ through a BNC cable and its use will be discussed in section 3.5.

3.3.2 FGIC Physics

Fundamental operations of a gridded ionization chamber is outlined in reference [43] and in depth in reference [32], whose notation we follow below to show how fission fragment energies and angles are deduced from the grid and anode signals.

When a fission event occurs, fragments are ejected on either side of the cathode into the fill gas. The fragments deposit most of their kinetic energy by ionizing the fill gas. Thus, higher energy fragments create more ion-electron pairs. Positive ions are attracted toward the cathode and negative electrons drift toward the anodes, which are shielded by the grid. This shield negates any influence of induced charge from the positively charged ions, which move about 1000 times slower than the electrons, and thus eliminates the angular and position dependence from the anode signal. Because of the grid shielding, all of the electrons produced in the gas arrive at the anode once the charge cloud has passed the grid on a very short time scale, less than a microsecond. The total charge on the anode, Q_a, is given by the equation,

$$Q_a = -ne, \tag{3.1}$$

n is the number of ion-electron pairs generated, and e is the fundamental charge. Therefore, Q_a is proportional to the fission fragment energy (E). The fission fragments are typically emitted at an angle producing different spacial orientations at varying distances from the cathode and grids. Therefore, the charge induced on the grid and cathode are angularly dependent. As the cloud drifts from the cathode toward the grid, the cathode has an induced charge of (ne) for the positive ions and ($-ne\frac{\overline{X}}{D}\cos\theta$) from the negative electrons. The total induced charge on the cathode (Q_c) is given by

$$Q_c = ne - ne\left(\frac{\overline{X}}{D}\cos\theta\right) = ne\left(1 - \frac{\overline{X}}{D}\cos\theta\right), \tag{3.2}$$

where $\overline{X}$ is the distance from the fragment origin to the center of mass of the electron drift cloud and D is the distance from the cathode to the grid. A diagram of a charge cloud drifting through the chamber is shown in Figure 3.6. The charge induced on the grid is a combination

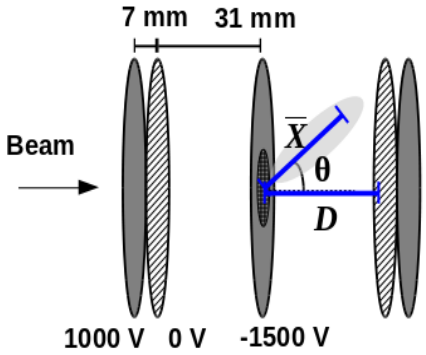

Figure 3.6: A schematic of the ionization chamber shows a schematic of the charge cloud following a fission fragment emitted at angle θ, the cathode to grid distance (D), and the distance to the center of mass $\overline{X}$ of the charge cloud.

of the negative angular-dependent induced charge due to the ions and electrons as they travel through the cathode-grid section of the detector ($-ne\left(1-\frac{\overline{X}}{D}\cos\theta\right)$) and positive induced charge from the ions and electrons once the cloud passes through the grid-anode (ne) section. The final form of the charge deposited on the grid (Q_g) is given by,

$$Q_g = -ne\left(1-\left(\frac{\overline{X}}{D}\cos\theta\right)\right)+ne = ne\frac{\overline{X}}{D}\cos\theta. \tag{3.3}$$

By carefully examining the ratio between the anode and grid signals, information about the angle of the fission product track can be extracted. Using Equations 3.1 and 3.3, notice that

$$\frac{Q_g}{Q_a} = \frac{\overline{X}}{D}\cos\theta. \tag{3.4}$$

The quantity $\overline{X}(E,A,Z)$ is the function of fragment energy (E), mass (A), and proton number (Z) and can be determined experimentally, described in reference [5] and later for 238-FGIC and 235-FGIC in Chapter 4.2.

We have shown that the charges on the grid and anode plates can be used to calculate the fragment energies and angles. Since we use charge integrating preamplifiers, described earlier in Section 3.3.1, we can show the charge on the anode (Q_a) is proportional to the anode signal pulse height (P_A) and likewise, the charge on the grid (Q_g) is proportional to the grid signal pulse height (P_G). The preamp signals are shown as a schematic in Figure 3.7. They have characteristic shapes, caused by the behavior of the charges drifting through the sections of the detector as discussed above. The signals from the preamps are read by

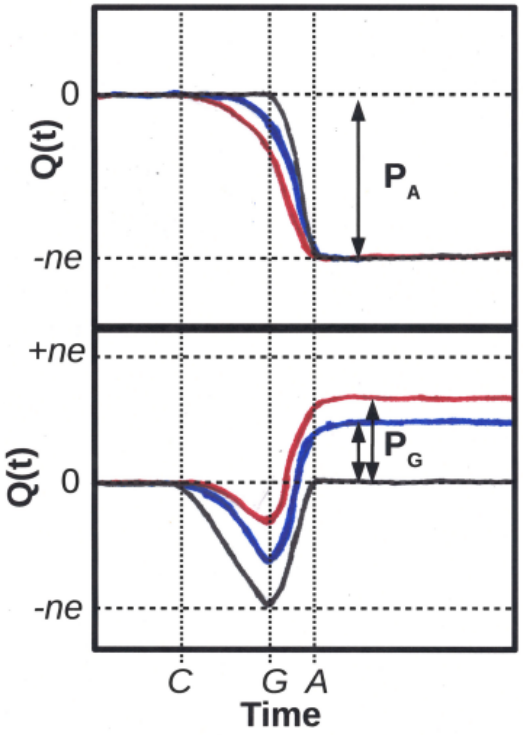

Figure 3.7: The integrated charge $Q(t)$ as a function of time on the anode (top) a grid (bottom) plates are shown for three different event angles: $\cos\theta = 0$ (red), $\cos\theta = 0.5$ (blue), $\cos\theta = 1$ (black). The times C, G, and A correspond to the points in time when the electrons begin drifting from the cathode, begin to reach the grid, and finally reach the anode. The corresponding pulse heights P_A and P_G are indicated. Note that P_G is angularly dependent.

waveform digitizers, discussed in 3.4.

The anode signals were also corrected for grid inefficiency, σ_{GI}. The grid inefficiency is a small correction that accounts for the imperfect shielding of the anode by the grid,

and accounts for on the order of 1% of the fragment's total energy. The purpose of the grid is to shield the anode from electron and ion induced charges while drifting between the grid and cathode. Thus, all the electrons seen by the anode appear to originate at the grid. However, while the electron cloud is drifting between the cathode and grid, some of the signal is detected [44]. This is seen in a small linear slope in the anode signal in Figure 3.8. By calculating the height of this small deformation and comparing it to the total

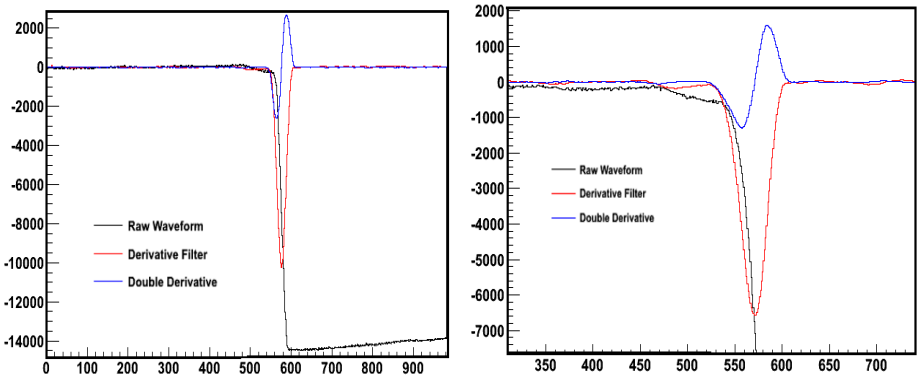

Figure 3.8: The anode signal (left) and zoomed-in anode signal (right) from the digitizers are shown with derivative filters used to calculate the grid inefficiency, a small correction inherent in gridded ionization chambers. The small slope in the anode signal before the steep drop is due to grid inefficiency. The y-axis is displaying arbitrary digitizer units (voltage), and the x-axis is digitizer samples (time).

signal height, the grid inefficiency can be measured. The measurement of this correction was performed using the method outlined by Khriachkov et al. [45], yielding a value of $\sigma_{GI} = 0.03135 \pm 0.0005$. The grid inefficiency can also be calculated using the equation:

$$\sigma = \frac{l}{l+p}. \tag{3.5}$$

Where $l = \frac{d}{2\pi}\left(\frac{\rho^2}{4} - \ln\rho\right)$ and $\rho = \frac{2\pi r}{d}$ with $r = 0.1$ mm, the grid wire radius, $d = 1$ mm, the grid spacing, and anode to grid distance $p = 7$ mm. This leads to a theoretical value of about 0.03, which agrees with the experimental method. The original anode signals P_a were corrected using the summing technique, following the equation

$$P_a^{cor} = \frac{P_a - \sigma_{GI}(P_a + P_g)}{1 - \sigma_{GI}}, \tag{3.6}$$

described in [46] [44].

Extraction of the anode (P_a) and grid (P_g) pulse heights is discussed in the next section. Because the expressions for the charge induced on the anode and the grid given in Equations 3.1 and 3.3 are written for the ideal case, the angular correction is performed using the pulse heights after correction for grid inefficiency. In Chapter 4, $\overline{X}/D$ is determined experimentally and the fission angles, θ, are calculated. Using the energies (from P_A) and emission angles (from P_G/P_A) of the two products, one can calculate the fission fragment mass distributions employing the double energy (2E) method with a resolution of 4-5 AMU as shown in chapter 4.

3.4 Data Acquisition

There are six signals that originate from the Frisch-gridded ionization chamber (FGIC) and flight path: two grids (G1 and G2), two anodes (A1 and A2), one cathode (C), and and one timing trigger from the accelerator (T0). All six signals are fed into the data acquisition system (DAQ) outside the flight path shielding. The channel mapping is shown in Table 3.1.

Table 3.1: The channel mappings for both DAQs.

-	A1	A2	G1	G2	C	T0
FGIC-238	5	7	9	11	3	1
FGIC-235	2	3	4	5	6	0

Both DAQ's consisted of a set of waveform digitizers to convert the analog signals to digital and a computer to store the data. A photo of the crate holding the digitizers is shown in Figure 3.9. The main setup difference in the 238-FGIC and 235-FGIC experiments was the DAQ system. In 238-FGIC, the waveforms were digitized with Acquiris 282 digitizers capable of a 4 GHz sample rate and stored for offline analysis. An example of the raw waveforms from the ^{238}U experiment is shown in Figure 3.10. For 235-FGIC, CAEN VX1720 VME based 12-bit digitizers collected the waveforms, which were then stored on a PC for offline analysis.

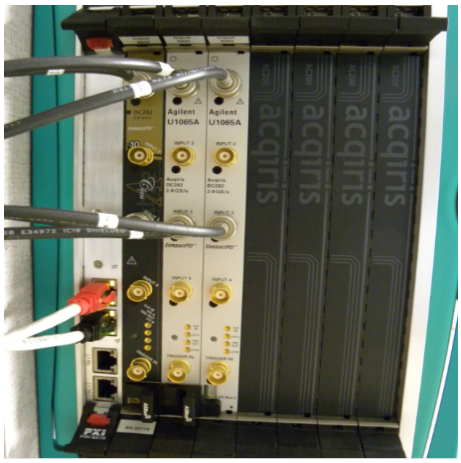

Figure 3.9: The digitizers used in 238-FGIC.

These self triggering 250 MHz digitizers have a lower sampling rate, but are still sufficient to resolve the timing structure of the beams at WNR. The 235-FGIC DAQ is explained in detail in reference [41].

To find the anode pulse height, the first part of the waveform is fit linearly to determine a baseline. The last part is fit with an exponential as the voltage recovers. These fits determine the limits where to measure the total change in height of the anode signal. For the grid signal, we measure the difference in the heights before and after the electrons pass through the mesh. The "T0" signal originates directly from the accelerator and indicates that a proton pulse is incident on the spallation target, providing the "start" for neutron Time-of-Flight (nToF) determination. The cathode signal utilizing fast amplifiers is used as the nToF "stop". Typical waveforms collected by the FGIC-235 DAQ are shown in Figure 3.11.

The difference in time between the accelerator pulse signal (T_0) and the cathode fission signal (C) indicates the nToF. The T_0 and C are converted to time signals by using the zero crossings of a derivative filter applied to the digitized waveforms and converted from units of channels to seconds using the combined waveform decimation factor (5 samples/channel) and the digitizer sample rate (4 GHz), 1.25 ns/ch.

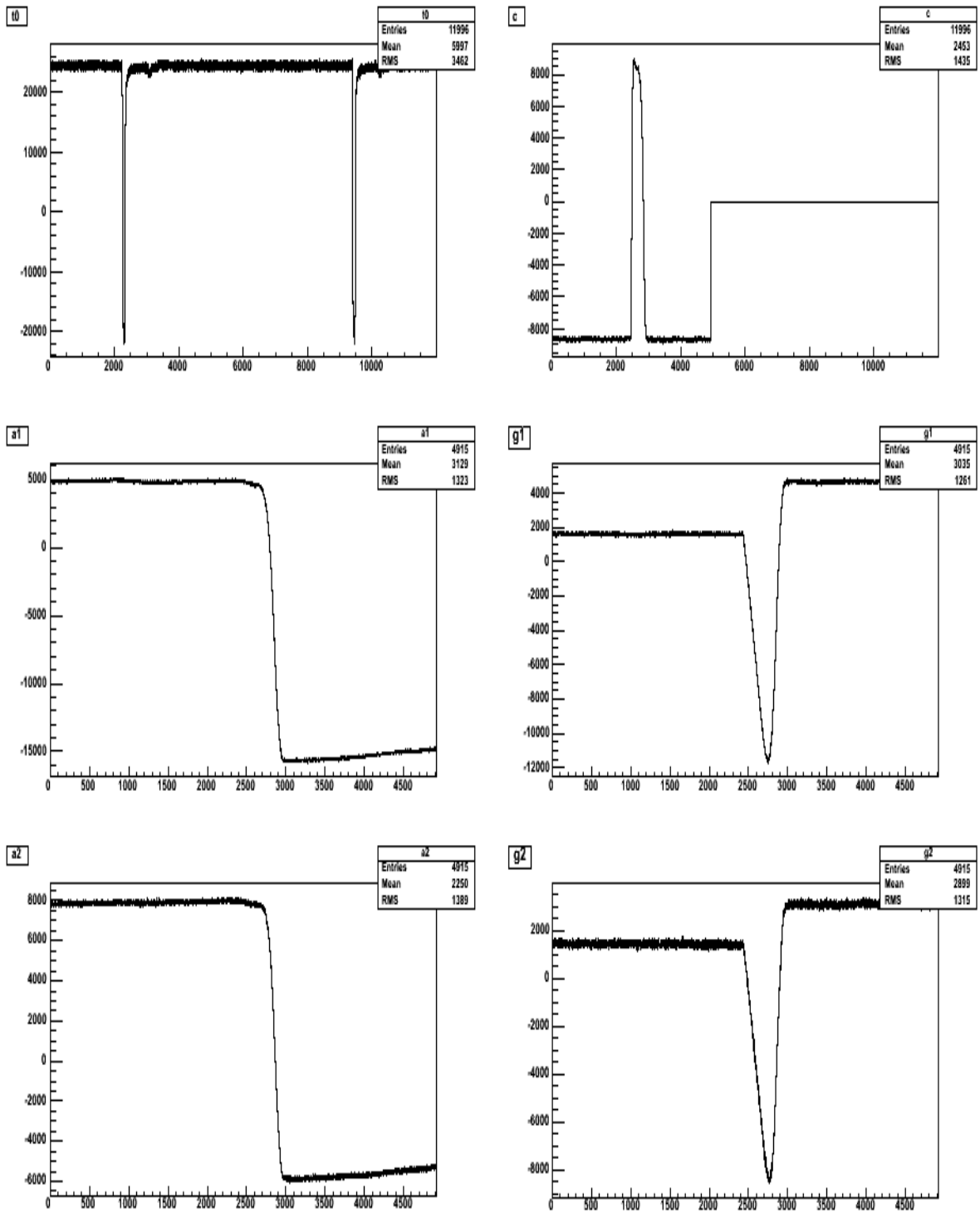

Figure 3.10: The digitized waveforms from a typical 238-FGIC DAQ event. The digitized signals are stored on a computer for later analysis, thus preserving as much information as possible about a fission event. Displayed from top to bottom and left to right: the T0, cathode, sample side anode, sample side grid, backing side anode, and backing side grid.

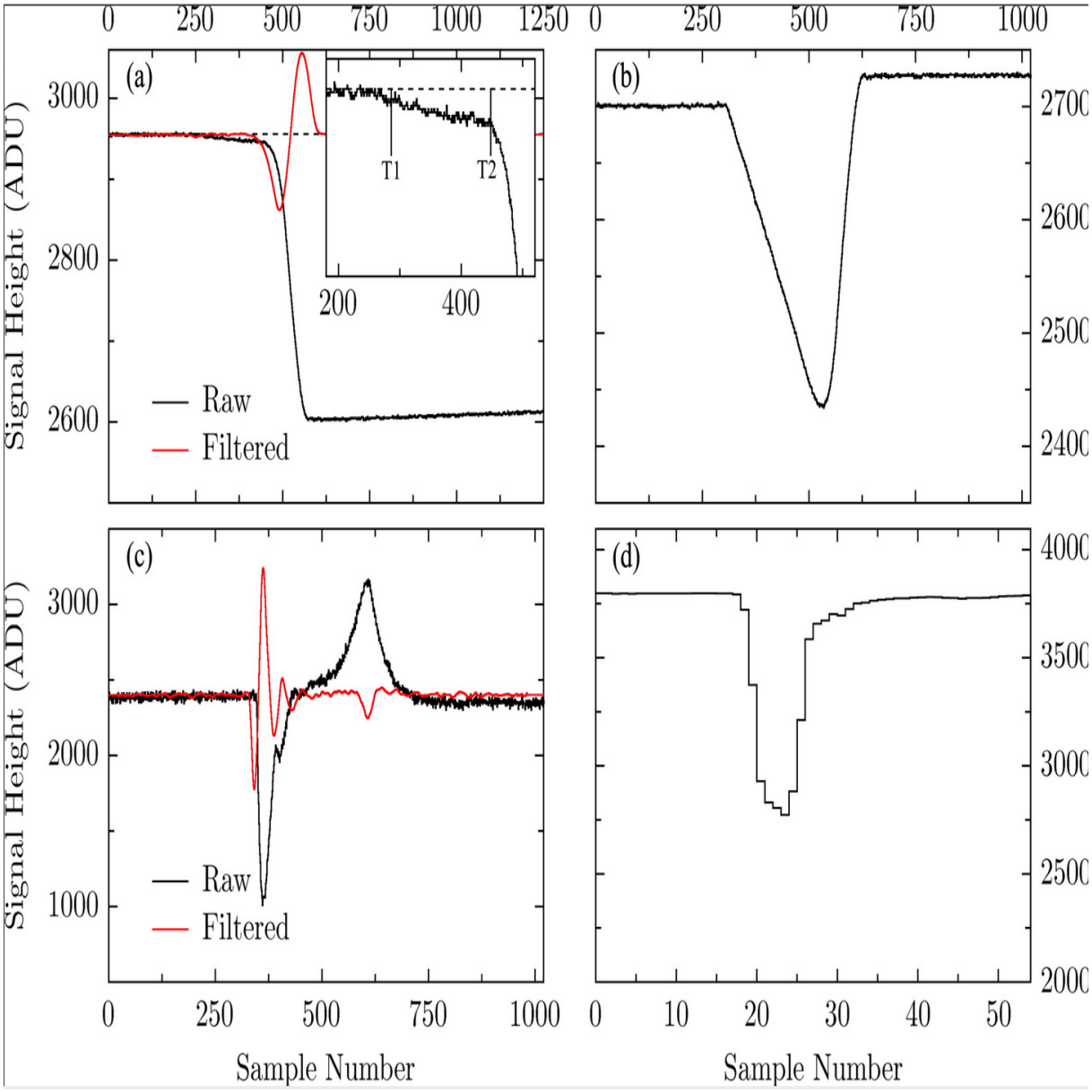

Figure 3.11: The digitized waveforms from a typical 235-FGIC DAQ event. Pictured are an (a) anode where T_1 and T_2 are the pickoff times for calculating grid inefficiency, (b) grid, (c) cathode with derivative filter in red, and (d) T0 from the accelerator. Figure taken from [41].

Data from both experiments were stored in small files for later processing. For the 238-FGIC, the data with beam and the correct digitizer settings are in runs data7_253 - data7_2983 and data12_0 - data12_3980. Carbon calibration data is found in data7_1 - data7_252. For 235-FGIC, the data with beam and good digitizer settings are found in runs 497-515, 522-538, 557-588, 591-1123, 1123-1137, 1295-1440. Carbon calibration data are in runs 1138-1348.

3.5 LANSCE Neutron Source

The detector was located in Los Alamos National Laboratory (LANL) at LANSCE-WNR (Los Alamos Neutron Science Center - Weapons Neutron Research). A schematic of the LANSCE facility is shown in Figure 3.12. LANSCE is an 800 MeV linear proton

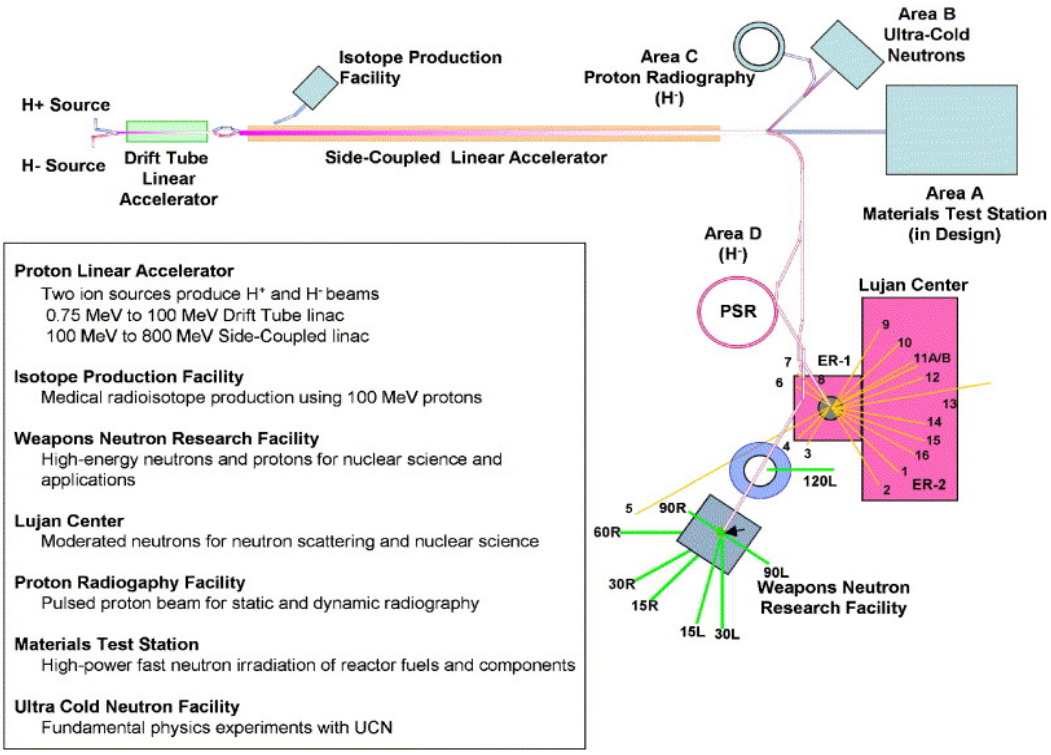

Figure 3.12: A schematic of the 800 MeV LANSCE accelerator with experimental facilities. 238-FGIC and 235-FGIC ran at WNR at the 90L flight path, located 90° with respect to the incident proton beam. Figure taken from [47].

accelerator coupled with spallation neutron sources that offer collimated beams of neutrons

from a cold to fast neutron spectrum [48]. The WNR facility is an unmoderated spallation neutron source where the 800 MeV pulsed proton beam is incident on a tungsten target. Spallation neutrons are collimated to an approximately 2 cm diameter beam through an approximately 6 m long steel pipe at the 90L flight path. The 90L flight path is located 90° with respect to the incident neutron beam on the tungsten target.

The proton beam timing structure at WNR is a 625 μs long macropulse consisting of micropulses 1.8 μs apart with 250 ps width, where the macropulse has a repetition rate of 60 Hz [47]. There are about 340 micropulses in each macropulse. During each micropulse, a bunch of protons are incident on the tungsten target, which sends neutrons with a spectrum of energies down the beam collimation apertures set at various angles. The available neutron energies range from 100's of keV to 100's of MeV. Neutron energies are determined using the neutron Time of Flight (nToF) method, detailed in Chapter 4.1. A spectrum of the neutron flux at flight path 90L is shown in Figure 3.13.

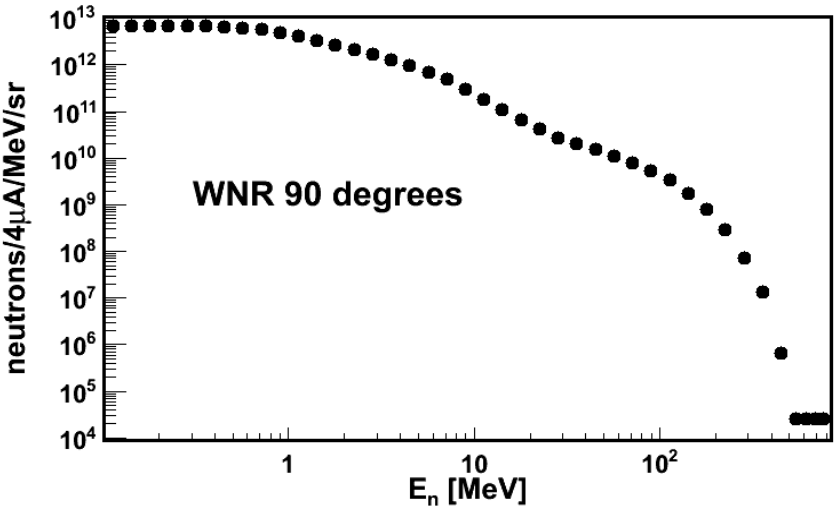

Figure 3.13: MCNP model of the neutron flux 90 degrees with respect to the incident proton beam at the WNR target. Units are given as a function of number of neutrons per 4 μA-proton current per steradian per energy. The flux can decrease or increase depending on solid angle covered by the experiment as a function of distance from the neutron production target.

This experiment shared the 90L flight path with the fissionTPC experiment. The neutron energy loss in the targets and windows of both detectors is negligible so placing them together in the beam line did not affect the quality of the measurement. A schematic of the flight path is shown in Figure 3.14. The TPC is placed about a meter from the flight path shutter, which shields the flight path and experimental personnel from neutrons when engaged.

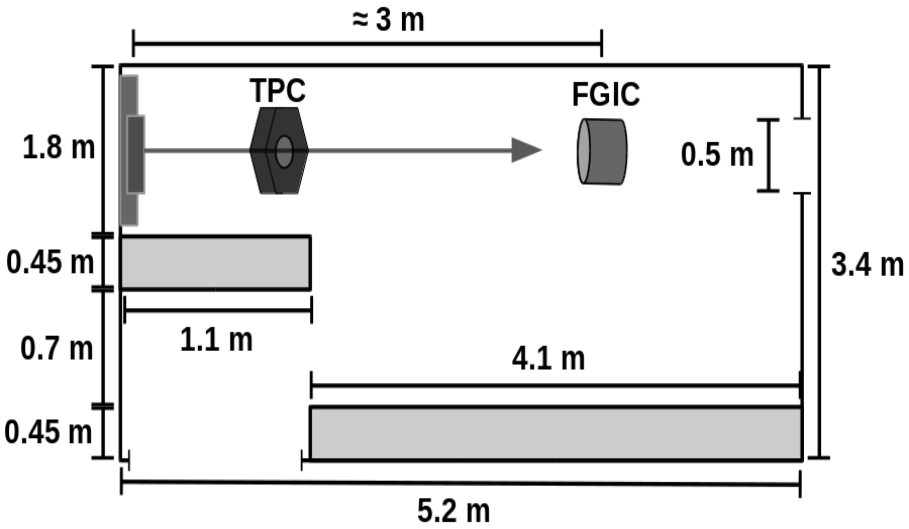

Figure 3.14: A schematic of the TPC and FGIC location on the 90L WNR flight path. Dimensions are approximate and not drawn to scale. Shielding blocks are pictured, along with the shutter from which the neutron beam is emitted after passing through approximately 6 m of collimation from the neutron production target. It passes through both the TPC and the FGIC into a 20 m long 0.5 m diameter pipe to a beam dump. The room ceiling is about 10 m in height. The calibrated flight path length (L) is calculated during the neutron time of flight calibration in Section 4.1.

CHAPTER 4

ANALYSIS

The ionization chamber's signals from the anodes, grids, and cathode and the accelerator timing signal are used to calculate physics observables like neutron energies, fragment energies, angles, and masses. The analysis procedures are discussed in the following chapter. There are many correction steps, which are outlined in Table 4.1. Data analysis is performed with the software package ROOT (`http://root.cern.ch/drupal/`). Part of the analysis is done using the Double Energy or 2E method, an iterative procedure where the energies and angles of the fission fragments are used with kinematic equations of motion to calculate the pre- and post-neutron emission fragment masses and energies. This method has been successful in determining fission fragment yields with similar detectors where data has been collected at quasi-monoenergetic neutron facilities [8], [9], [49]. The 2E procedure is outlined in further detail in Table 4.3.

Throughout the chapter, figures from intermediate steps of the ^{238}U analysis are shown. The analysis process is nearly identical for both isotopes, but when differences arise they will be discussed. These differences largely stem from steps requiring calibration to a previous measurement or steps incorporating simulations.

Table 4.1: A summary of analysis procedures.

Correction	**Description**	**Input**	**Output**
Waveform analysis Section 3.3	Use derivative filters to extract pulse heights and timing.	Digitized waveforms	P_{A1}, P_{A2}, P_{G1}, P_{G2}, T_1, T_0
Determine neutron energy Section 4.1	Use the neutron time-of-flight (nToF) method.	T_0 and T_1	E_n
Uncalibrated nToF Section 4.1.1	nToF is the difference in the fission signal and the accelerator signal.	T_0 and T_1	ΔT
nToF calibration Section 4.1.2	Use the carbon "notch" and gamma "flash" to determine the flight path length.	ΔT, T_γ, T_C, E_C	L
Convert nToF to energy Section 4.1.3	Use relativistic equations to determine neutron energy.	ΔT, L	E_n
Calculate the fission emission angles Section 4.2	Use the ratios of anode and grid pulse heights to calculate correction factors and emission angles.	P_{A1}, P_{A2}, P_{G1}, P_{G2}	$\cos\theta_1$, $\cos\theta_2$
Determine $\left(\overline{X}/D\right)_i$ Section 4.2.1	Plot P_A as a function of P_G/P_A and use projections and derivative filter to find the falling edge.	P_{A1}, P_{A2}, P_{G1}, P_{G2}	$\left(\overline{X}/D\right)_i$ for each P_{Ai}
Calculate the angles Section 4.2.2	Apply the $\left(\overline{X}/D\right)_i$ to recover emission angles	$\left(\overline{X}/D\right)_i$, P_{A1}, P_{A2}, P_{G1}, P_{G2}	$\cos\theta_1$, $\cos\theta_2$

Anode corrections Section 4.3	Use low E_n events with a provisional momentum correction to find energy loss correction and gain calibrations parameters.	P_{A1}, P_{A2}	b_1, b_2, G_a, G_b
Provisional momentum correction Section 4.3.1	Calculate provisional neutron momentum corrected masses, angles, and uncalibrated energies.	E_n, P_{A1}, P_{A2}, $\cos\theta_1$, $\cos\theta_2$	μ_1, μ_2, P_{A1}^{cm}, P_{A2}^{cm}, $\cos\theta_1^{cm}$, $\cos\theta_2^{cm}$
Energy loss correction 4.3.2	Determine the energy loss correction parameters from linear fits to average anode pulse height as a function of emission angle.	P_{A1}^{cm}, P_{A2}^{cm}, $\cos\theta_1^{cm}$, $\cos\theta_2^{cm}$	b_1, b_2, P_{A1}^{b}, P_{A2}^{b}
Gain calibration Section 4.3.3	Use light and heavy anode peak locations for both anode distributions to calibrate the backing to the sample side.	$P_{A1}^{b}(\cos\theta_1^{cm}, b_1)$, $P_{A2}^{b}(\cos\theta_2^{cm}, b_2)$	G_a, G_b, P_{A1}^{cal}, P_{A2}^{cal}
Energy calibration and momentum correction Section 4.4	Calibrate the anode spectra from digitizer units [ADU] to energy units [MeV].	P_{A1}, P_{A2}	E_1, E_2
Determine parameters Section 4.4.1	Calibrate the anode spectra to previously measured fission product energies.	P_{A1}^{cal}, P_{A2}^{cal}, E_H, E_L	C_a, C_b
Complete energy calibration Section 4.4.2	Calibrate anode pulse heights for events at all incident neutron energies along with a neutron momentum correction.	P_{A1}, P_{A2}	$E_1(P_{A1}^{cm}, b_1, C_a, C_b)$, $E_2(P_{A2}^{cm}, b_2, C_a, C_b, G_a, G_2)$
The 2E method[1] **Section 4.5**	Use the fission product energies and angles to calculate masses while making mass dependent corrections.	E_1, E_2, $\cos\theta_1^{cm}$, $\cos\theta_2^{cm}$	m_1^{pre}, m_2^{pre}, m_1^{post}, m_2^{post}, E_1^{pre}, E_2^{pre}, E_1^{post}, E_2^{post}

[1]See Table 4.3 for an expanded description.

Charge correction Section 4.6	A second correction to the emission angles for $\overline{X}$ following a similar procedure to the first angular correction in Section 4.2.1.	m_1^{pre}, m_2^{pre}, $\cos\theta_1^{cm}$, $\cos\theta_2^{cm}$	$\cos\theta_1^{cor}$, $\cos\theta_2^{cor}$
Physics results Section 4.7	Results from the 2E method are used to calculate yields and total kinetic energy release.	m_1^{pre}, m_2^{pre}, m_1^{post}, m_2^{post}, E_1^{pre}, E_2^{pre}, E_1^{post}, E_2^{post}	$\overline{TKE}^{pre}(E_n)$, $\overline{TKE}^{post}(E_n)$, $Y^{pre}(E_n)$, $Y^{post}(E_n)$
Uncertainty analysis Section 4.8	A description of the uncertainty budget including energies and mass resolution.	calibration parameters	σ_E, σ_{TKE}, mass resolution

4.1 Neutron Time of Flight

The incident neutron energies, E_n, are determined using the neutron time-of-flight (nToF) method. It is classically observed that the distance an object travels (L) is equal to its speed (v) multiplied by the travel time (ΔT) which looks like,

$$L = v\Delta T. \tag{4.1}$$

The raw time of flight (ΔT) is calculated in Section 4.1.1. The flight path length (L) is determined using a carbon calibration, explained in Section 4.1.2. Using L and ΔT, the neutron's speed, and therefore energy (E_n) can be determined using the relativistic version of Equation 4.1 in Section 4.1.3. Previous experiments at WNR have already used the nToF method to determine neutron energy [50].

4.1.1 Uncalibrated nToF

As discussed in Chapter 3, when a proton pulse is incident on the tungsten spallation neutron source, a burst of gamma rays followed by neutrons with a spectrum of energies travel toward the detector. The proton pulse signal from the accelerator (T_0) and the signal from the cathode indicating that a fission event has taken place (T_1) are recorded. The T_0 and T_1 originate from the zero crossing of the second derivative filter applied to digitized waveforms and are converted from channels to seconds using the digitizer sample rate (4 GHz), 0.25 ns/sample. The difference in the signal times is ΔT, the raw time of flight, simply expressed as,

$$\Delta T = T_1 - T_0. \tag{4.2}$$

The raw ΔT spectrum is shown in Figure 4.1. Since ΔT involves the cathode signal, which is a fission trigger, some notable features in the spectrum are the first-, second-, and third-chance fission thresholds, which appear as peaks in the spectrum when the fission cross section suddenly rises, shown in Figure 4.2. A very small bump appears in the beginning of the spectrum, which is the gamma peak from photo fission and is used to calibrate the

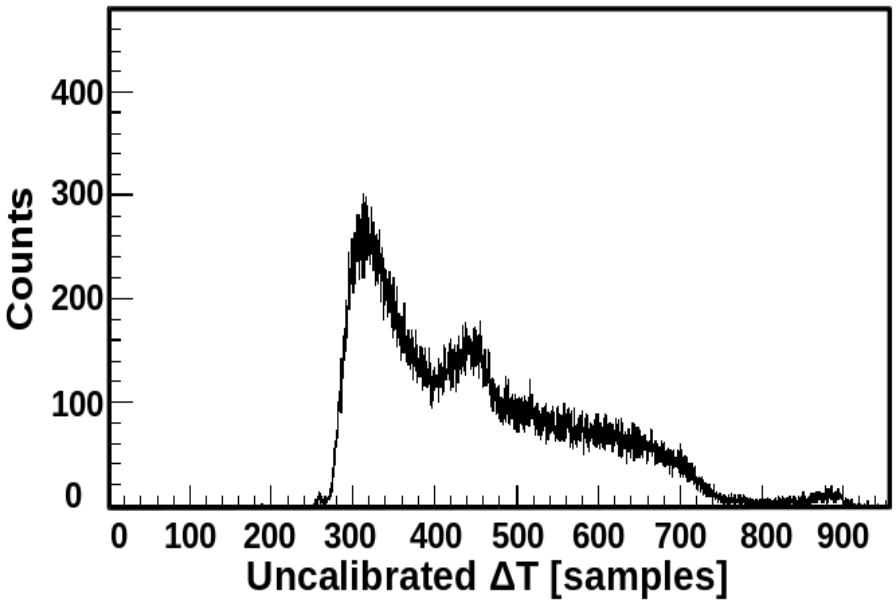

Figure 4.1: The uncalibrated time of flight for ^{238}U, ΔT, in digitizer samples, which are proportional to nanoseconds. A short time of flight corresponds to high energy neutrons while slower neutrons have a longer time of flight. The rises in the nToF correspond to multi-chance fission thresholds.

spectrum.

4.1.2 nToF Calibration

The nToF is essentially a linear energy calibration where the gain is determined using the digitizer sample rate to calculate time as shown in the previous section and the linear offset is determined by the position of the photofission peak, t_γ. To determine t_γ, the flight path length L, must be determined by collecting data when a carbon filter is placed in beam. The carbon filter is an approximately $2 \times 2 \times 4$ inch block of graphite. It was placed in beam directly on the collimation aperture with duct tape. The carbon filter works by scattering neutrons at specific energies, shown in the total carbon cross section Figure 4.4. Statistics with the carbon filter in beam were allowed to accumulate for about 2 days for each uranium isotope. Events collected during these times are not used in the final 2E analysis because the block induces additional background from neutron scattering.

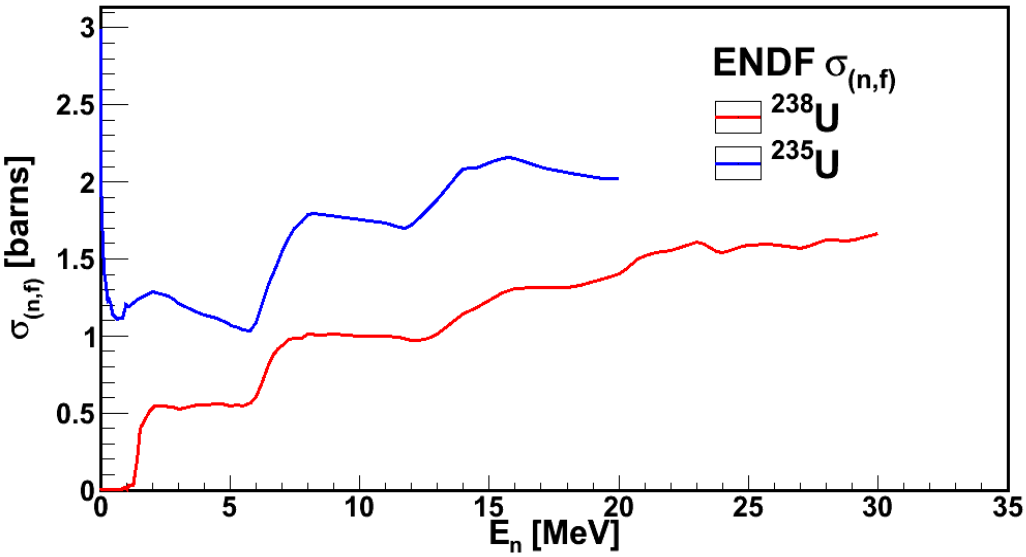

Figure 4.2: The neutron-induced fission cross section, $\sigma_{(n,f)}$ as a function of E_n is shown for ^{235}U (blue) and ^{235}U (red) [1]. The first-, second-, and third-chance fission thresholds are clearly seen as steps in the cross sections around $E_n = 1.5$, 7, and 14 MeV.

The raw ΔT spectrum with highlighted calibration features is shown in Figure 4.3. To calibrate the spectrum, we must 1) convert from digitizer samples to nanoseconds and 2) align the gamma peak to the correct time (i.e. the time it takes a gamma produced at the spallation target to travel down the flight path at the speed of the light to the uranium target). This calibration requires knowledge of the flight path length, which we measure using features in ΔT caused by incident neutrons interacting with the carbon filter.

The carbon calibration works on the principle of calculating total flight path length based on the time differences between two spectral features in a raw ΔT spectrum. The gamma peak appears as a small peak at the beginning of the spectrum from the reaction ^{238}U(γ,f) from gamma rays emitted by the proton pulse on the tungsten spallation target. The peak is fit with a Gaussian whose centroid and σ are also used to calculate timing resolution. The carbon "notch" is caused by incident neutrons with an energy corresponding to the resonance in the carbon scattering cross section at $E_n = 2078.0 \pm 0.3$ keV [1]. When the spectrum in Figure 4.3 is examined, a "notch" is present in the spectrum where those neutrons were

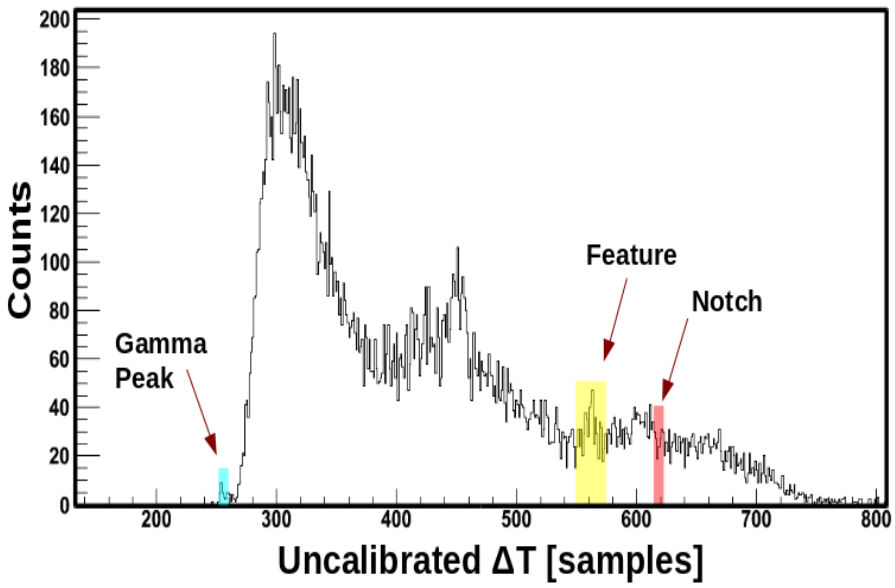

Figure 4.3: The uncalibrated time of flight, ΔT, in digitizer samples, when the carbon filter is placed in beam during FGIC-238. The carbon "notch" (t_c) and gamma peak (t_γ) appear at well known energies, which are used to determine the flight path length and therefore, neutron energy calibration. The "feature" is another dip in the carbon cross section that is used to help identify the position of the "notch".

scattered out of the beam path by the carbon filter. Another larger, but broader "feature" in the carbon cross section can also help in the identification of the carbon notch, but is too wide to use for energy calibration, shown in Figure 4.4.

The goal of the carbon calibration is to calculate the flight path length (L) based on the known energy of the carbon notch, E_n. With the correct L, the raw ΔT spectrum can be calibrated so time starts at 0 ns and the centroid of the gamma peak is aligned to the correct value. The kinetic energy of a non-relativistic particle is given by,

$$E_n = \frac{1}{2} m_n v^2 \tag{4.3}$$

where $m_n = 939.6$ MeV/c^2 and v is the speed [51]. (As an aside, we can verify that the classical approximation works by rearranging 4.3 and calculating v. When $E_n \approx 2$ MeV, $v \approx 0.06c$, under the limit for applying relativistic effects in this case.) By combining

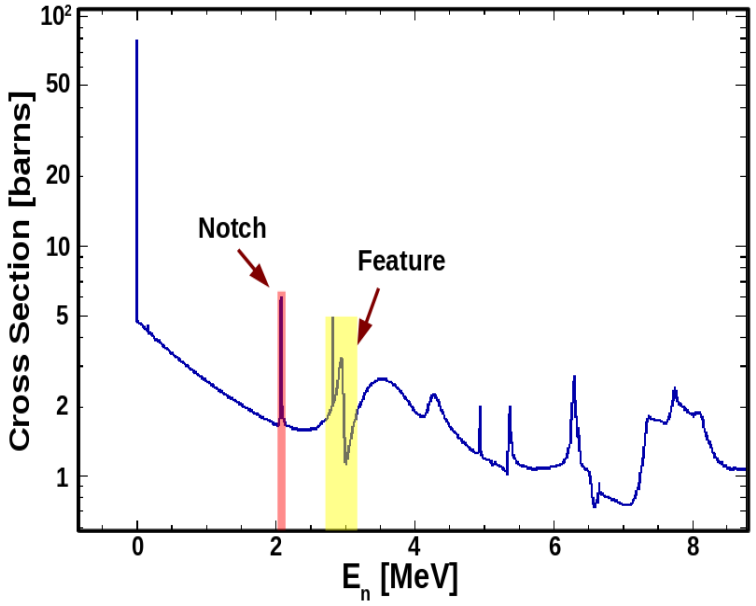

Figure 4.4: Total carbon cross section from ENDF for (^{12}C+n) [1] with the resonances that correspond to the "notch" and the "feature" indicated.

equations 4.3 and 4.1, we arrive at

$$E_n = \frac{1}{2} m_n \frac{L^2}{\Delta t_C^2}. \tag{4.4}$$

Here, Δt_C is the calibrated time it takes for a neutron of $E_n = 2.078$ MeV to get from the spallation source to the detector, which is presently unknown. We did however, measure the position of the notch relative to the gamma peak, $\Delta t_{\gamma \to C}$. We also know that the time is takes for the gammas Δt_γ to travel the distance L from the spallation target to detector at the speed of light c is,

$$\Delta t_\gamma = L/c. \tag{4.5}$$

Thus, we can express Δt_C as,

$$\Delta t_C = \Delta t_\gamma + \Delta t_{\gamma \to C}. \tag{4.6}$$

Making the substitution, Equation 4.4 becomes,

$$E_n = \frac{1}{2} m_n \frac{L^2}{\left(\Delta t_\gamma + \Delta t_{\gamma \to C}\right)^2}. \tag{4.7}$$

With another substitution for t_γ using Equation 4.5, we arrive at

$$E_n = \frac{1}{2} m_n \frac{L^2}{\left(\frac{L}{c} + \Delta t_{\gamma \to C}\right)^2}. \tag{4.8}$$

Solving Equation 4.8 for L yields

$$L = \frac{\Delta t_{\gamma \to C}}{\sqrt{\frac{2E_n c^2}{m_n}}}. \tag{4.9}$$

The uncertainty in L is given by propagation of uncertainties according to the method in [52],

$$\delta L = \sqrt{\left(\frac{\partial L}{\partial \Delta t_{\gamma \to C}} \delta \Delta t_{\gamma \to C}\right)^2}, \tag{4.10}$$

and taking the partial derivative of Equation 4.9 results in,

$$\delta L = \sqrt{\left(\frac{c}{\sqrt{\frac{2E_n c^2}{m_n}}} \delta \Delta t_{\gamma \to C}\right)^2}. \tag{4.11}$$

The difference between the carbon notch ($t_c = 617.5 \pm 0.5$ samples) and gamma peak ($t_\gamma = 258.6 \pm 0.3$ samples) is calculated by converting to nansoseconds using the waveform decimation factor (5 channels/sample) and digitizer sample rate (4 GHz = 0.25 ns/sample) and using Equation 4.6. Thus, $\Delta t_{\gamma \to C} = 448.6 \pm 0.7$ ns for the ^{238}U experiment. The uncertainty in $\Delta t_{\gamma \to C}$ results from adding the two uncertainties in quadrature,

$$\delta \Delta t_{\gamma \to C} = \sqrt{\delta t_c^2 + \delta t_\gamma^2}. \tag{4.12}$$

Thus, the flight path length can be determined along with its uncertainty, $L = 9.596 \pm 0.015$ m.

To calibrate the raw ΔT spectrum, use L and Equation 4.5 to calculate where the position of the centroid should appear. After fitting the gamma peak with a Gaussian, align the centroid fit value of the gamma peak to the calculated value. Apply this linear offset correction to the whole data set to recover the calibrated neutron time of flight, shown in Figure 4.5. The timing resolution of the final calibrated nToF spectrum is given by the full width half max of the gamma peak, 3.0 ± 0.3 ns, as shown in Figure 4.5, extracted from the

fit parameters.

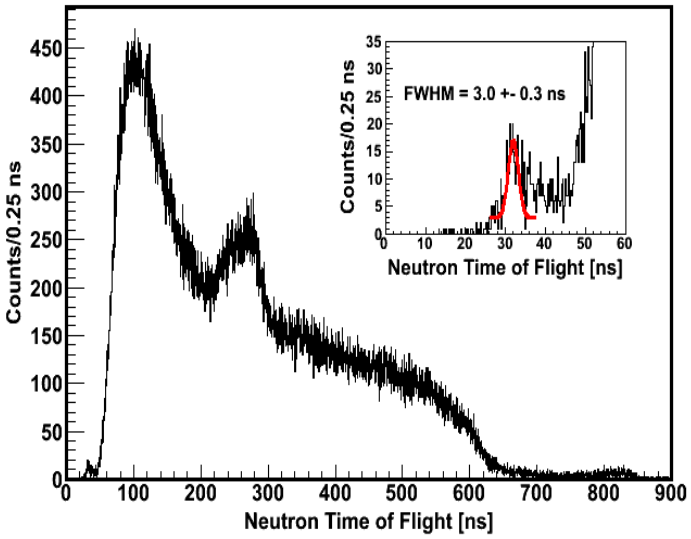

Figure 4.5: Neutron time-of-flight spectrum for ^{238}U. The inset displays the Gaussian fitted peak from photofission with full width half-max information. The features in the spectrum are due to multichance fission thresholds.

4.1.3 Converting nToF to Energy

The conversion from nToF to energy follows the relativistic kinetic energy equation,

$$E_n = \frac{1}{2} m_n c^2 \left(\frac{1}{\sqrt{1-\beta^2}} - 1 \right), \tag{4.13}$$

where $m_n = 939.6$ MeV/c^2 is the rest mass of the neutron and $\beta = v/c = L/(ct)$. As before, $L = 9.596 \pm 0.015$ m, t is the time in nanoseconds, and c is the speed of light. The E_n spectrum for ^{238}U is shown in Figure 4.6.

Each incident neutron energy also has an uncertainty associated with it, based on the resolution of the gamma peak. In a perfect neutron time-of-flight (nToF) spectrum, the gamma peak would look like a delta function since all the gammas arrive at a single time, however it is spread out because of experimental systematic effects (e.g. timing resolution of the accelerator signal, production target thickness, detector timing resolution, cable length, digitizer resolution). This uncertainty propagates to all nToF energies, with each energy

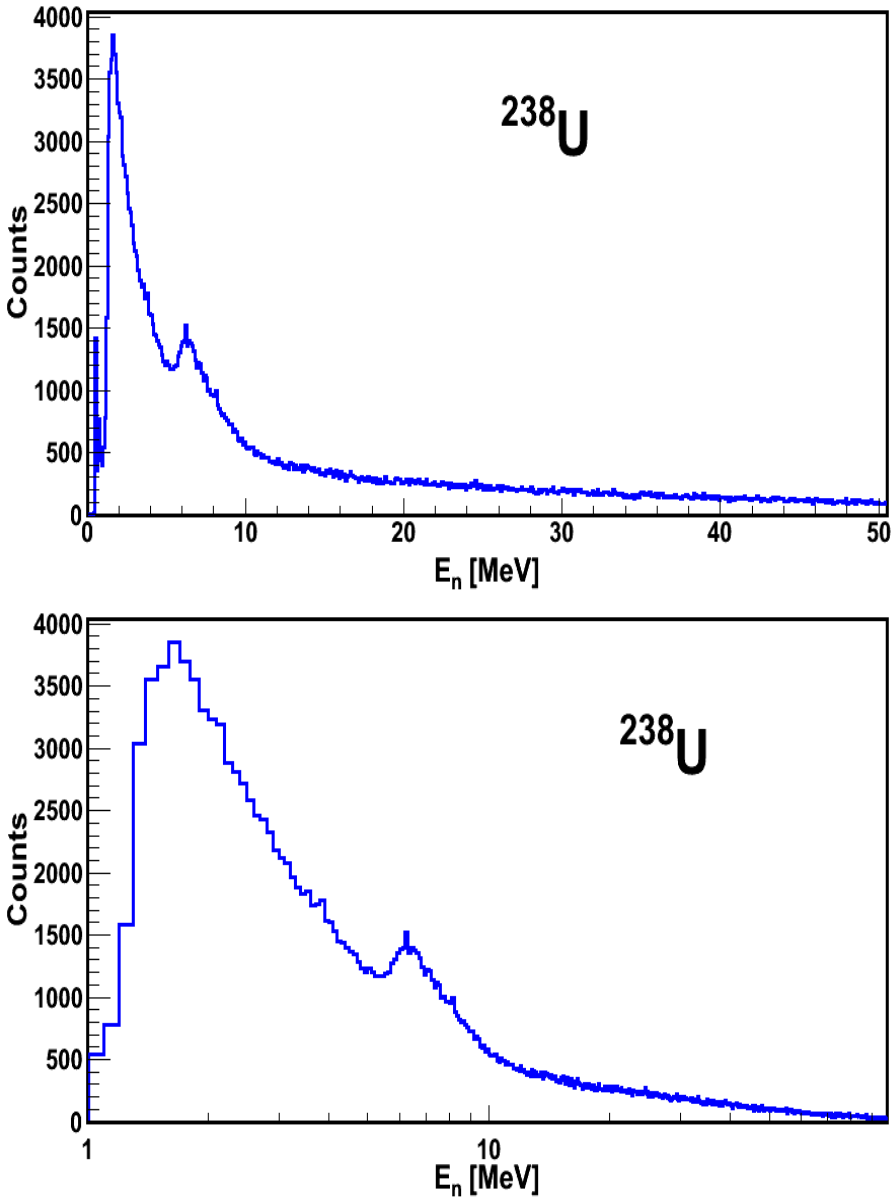

Figure 4.6: The ^{238}U(n,f) E_n spectrum for events with anode pulse heights $P_A > 30$ in arbitrary digitizer units (to cut out light particles). The structure is due to multi-chance fission thresholds. (Bottom) The neutron energy, shown on a logarithmic scale with 10 bins/decade.

having a different systematic uncertainty. To understand how the uncertainty behaves, consider the following example. Since the ^{238}U nToF gamma peak has FWHM = 3 ns, the E_n can be calculated 3 ns apart. Therefore, the energy of the neutron with an nToF = 200 ± 3 ns is a range centered on $E_n(200) = 12.3$ MeV with asymmetric error bars from $E_n(203) = 11.9$ MeV to $E_n(197) = 12.6$ MeV. In all of the analysis, logarithmic binning is used since it roughly corresponds to how uncertainty in distributed in the nToF data. The timing resolution determines how many bins to use per decade of neutron energy. For example, 30 bins/decade is more than enough to be within the energy resolution of 3 ns.

4.2 The Angular Distribution

The ratio of the grid pulse height (P_G) to the anode pulse height (P_A) is proportional to the quantity $\overline{X}/D\cos\theta$ [32] as was shown in section 3.3. Here, $\overline{X}$ is the path length from the fission origin to the center of mass of the electron drift cloud and D is the distance from the cathode to the grid. To recover the angle of the fission event for a given range of anode values, the $\overline{X}/D$ constant of proportionality as a function of anode pulse height must be experimentally determined, discussed in Section 4.2.1.

4.2.1 Determine $\overline{X}/D$

To begin, note that, $\overline{X}$ depends on the energy (P_A) of the fission product, its mass, and its charge, but the $\overline{X}$ value can be determined experimentally in the following procedure. An important relationship in this analysis is

$$P_G/P_A \propto \frac{\overline{X}}{D}\cos(\theta), \tag{4.14}$$

which was calculated in 3.3. P_A is plotted as a function of "angle", (P_G/P_A) shown in Figure 4.7. Because $\frac{\overline{X}}{D}$ is fission product energy dependent, one $\frac{\overline{X}}{D}_i$ can be determined for a slice of anode pulse heights, where i is the index of a slice. P_{A1} and P_{A2} on the y-axis in Figure 4.7 are divided into i slices. The domain of $\cos\theta$ is $[0, 1]$, however the x-axis of Figure 4.7 does not cover this range . We assume that $\frac{\overline{X}}{D}$ is like some constant of

proportionality that stretches or shrinks the angular distributions depending on the detector gas and voltages.

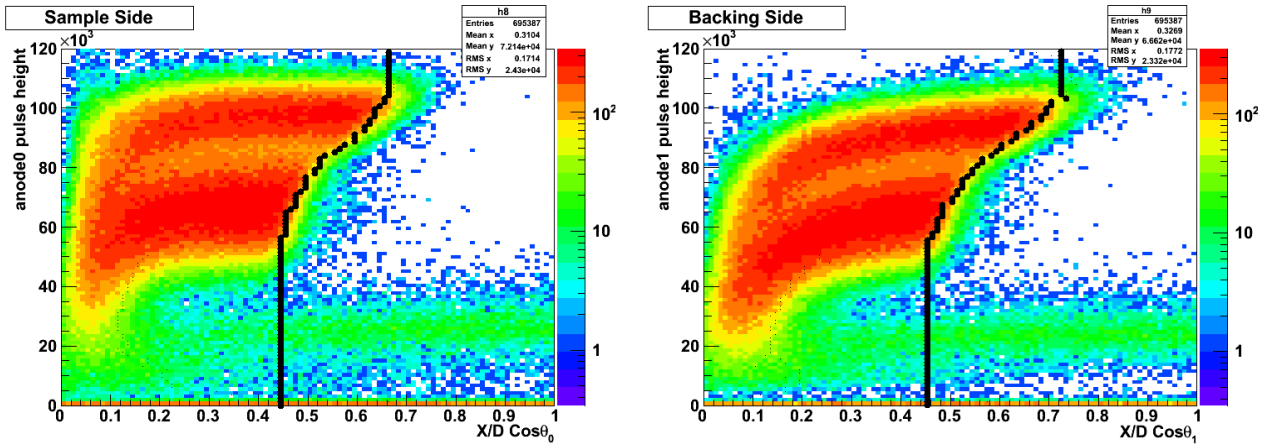

Figure 4.7: The heavy and light fission fragments sweep out the two "wings" at low and high pulse heights respectively. The $\overline{X}/D_i$ values are shown as black points, calculated directly from the derivative filter minima from the projections. We can see some distinguishing features about the fission events in Figure 4.7, where the light and heavy fragment bands are clearly visible. The band at low P_A are alphas and other light particles.

To calculate $\frac{\overline{X}}{D}_i(\cos\theta = 1; \cos\theta = 0)$, take an x-projection for each P_{A1} and P_{A2} i-slice, which represents an angular distribution at a particular average fragment energy. An example of a slice when $i = 80$ is shown in Figure 4.8. As mentioned, we expect the domain to cover $\cos\theta = [0, 1]$. However, because of the stretching/shrinking factor, $\frac{\overline{X}}{D} \neq 1$, the slice falls at a different value, in Figure 4.8 at around $\frac{\overline{X}}{D} = 0.6$. To determine the values for $\frac{\overline{X}}{D}_i$, we apply a derivative filter to find where the distribution falls to zero. A limitation of this method is when statistics are insufficient on the upper and lower edge of the $(P_A)_i$'s to create a decent distribution. In these cases, low and high limit values for $\overline{X}/D$ were applied for low and high pulse heights where the distributions did not have as well defined edges below 45% and above 87% of the total anode pulse height range. The $\frac{\overline{X}}{D}_i$ values are determined independently for each half of the detector and show the range of the fragments in the sections between the cathode and grids.

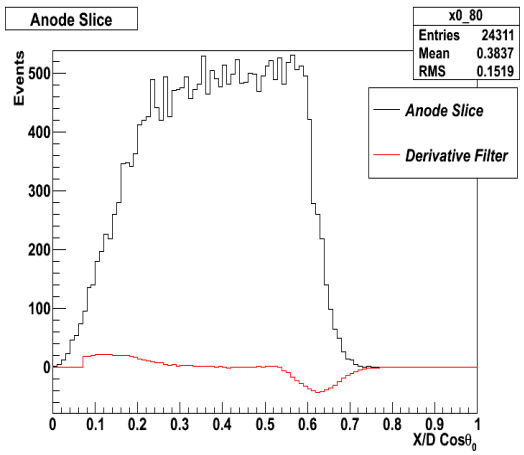

Figure 4.8: A derivative filter is applied to an x-projection of an anode slice to determine how much the angular distribution has been deformed. We chose the location of the derivative filter minimum to pick off $\overline{X}/D$.

4.2.2 Calculate the Angles

Once the $\frac{\overline{X}}{D}_i$ values are determined for each anode slice, they are applied to reveal corrected anode distributions as a function of the fragment emission angle, shown in Figure 4.9. This is simply done by rearranging Equation 4.14 and using the extracted $\left(\overline{X}/D\right)_i$ for the corresponding P_{Ai}, as in

$$\cos\theta_1 = \frac{P_{G1}}{\frac{\overline{X}}{D}_i P_{A1}} \qquad\qquad \cos\theta_2 = \frac{P_{G2}}{\frac{\overline{X}}{D}_i P_{A2}}. \tag{4.15}$$

The detector's angular resolution is determined by subtracting the $\cos\theta_1$ (the sample side) from $\cos\theta_2$ (the backing side). This produces a Gaussian distribution centered on zero with a FWHM = 0.159, comparable to other detectors of this design [5], and is displayed in Figure 4.11. Some events at very steep angles ($\cos\theta \leq 0.2$) are missing due to straggling in the backing and sample, which can be seen in Figure 4.11. These events are deselected from the final physics analysis by setting a threshold on the anode and the angular values described in Section 4.5.1.

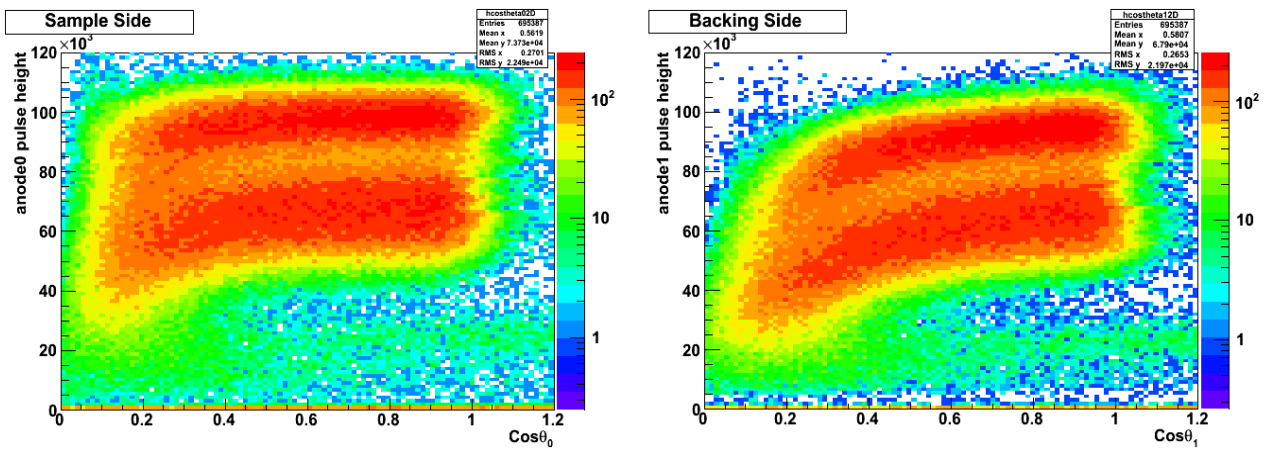

Figure 4.9: The $\left(\overline{X}/D\right)_i$ correction values were applied to the light and heavy fragment "wings" causing them to become more rectangular. Notice that the backing side dips to lower pulse heights when $\cos\theta \leq 0.4$ because fragments emitted at steep angles loose more of their energy in the target backing material. This is corrected in section 4.3.

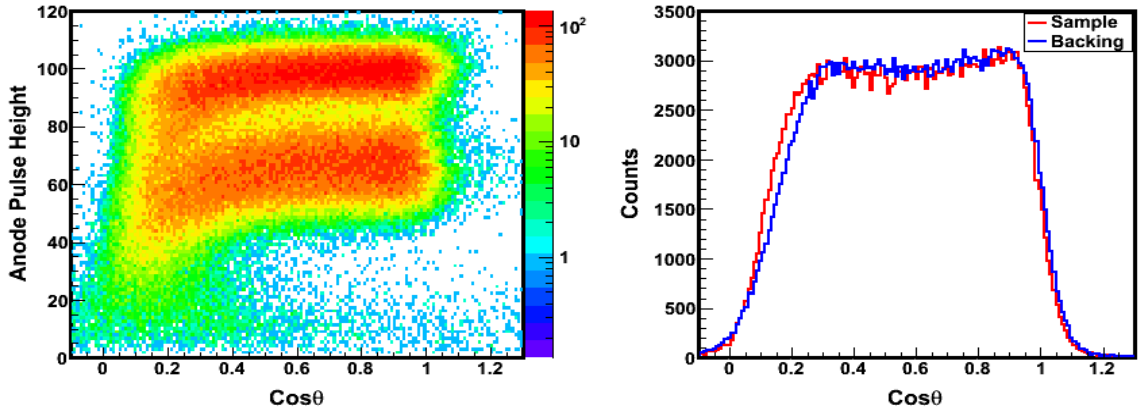

Figure 4.10: Since fission happens back to back in the center-of-mass frame, we expect that the angle distributions should overlay for both halves of the detector, which is the case.

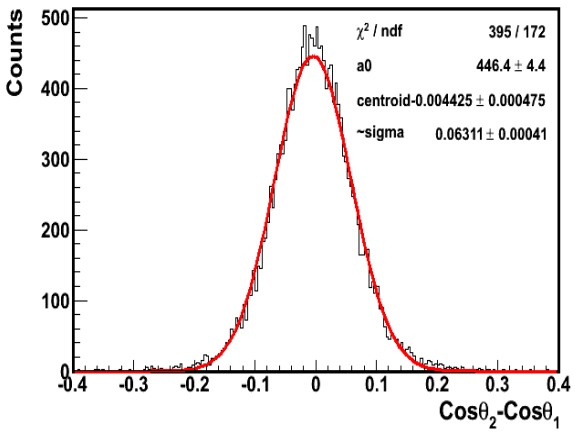

Figure 4.11: A quantitative comparison of angular resolution of the detector is determined by subtracting the cosine of the polar angle in the lab frame.

4.3 Anode Corrections

To determine the energy calibration for the anode pulse height signals, P_{A1} and P_{A2} (arbitrary digitizer units in ADU) to E_1 and E_2 (energy units in MeV), we first must determine some correction parameters for energy loss in the target/backing materials (Section 4.3.2) and for gain mismatch between the preamps (Section 4.3.3) which cause the two anode raw spectra to misalign as shown in Figure 4.12. These corrections must be done after an additional preliminary incident neutron momentum correction, discussed in Section 4.3.1.

4.3.1 Provisional Momentum Correction

Unlike the other correction and calibration parameters, the momentum correction is non-linear with fragment energy because of an additional dependency on fragment angle, compound nuclear mass, and fragment mass. However, a provisional neutron momentum correction can be made to the anode pulse heights and angles by restricting the analyzed energy range $E_n = 1.5 - 2.0$ MeV which allows for the assumption of first-chance fission with compound nuclear mass of $M_{CN} = 239$ in the calculation of provisional masses. Using the provisionally corrected data at high E_n, where neutron momentum matters more, would introduce unnecessary uncertainty into the calibration parameters. Thus the energy loss,

gain calibration, and energy calibration parameters are determined first in this restricted energy range and then applied to all the data. The complete energy calibration process is described in Section 4.4.2.

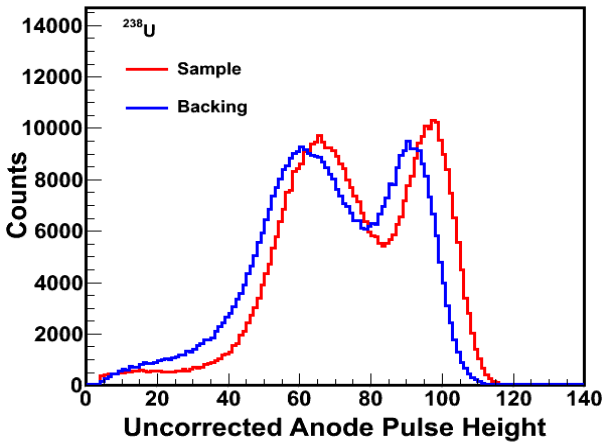

Figure 4.12: A histogram of the raw anode pulse heights in arbitrary digitizer units which are proportional to fission fragment energies. The double hump structure is caused by the lower energy heavy fragment and the higher energy light fragment. Note the the backing side (blue) is slightly lower in energy due to energy loss in the target and backing.

The incident neutron momentum transfer correction, especially at high energies, requires a transition from the lab frame to the center of mass (CM) frame. In the CM frame, the fission fragments' masses, m_1 and m_2, pre-neutron evaporation are related to the mass of the compound nucleus $M_{cn} = 239$ and the energies of the two fragments, $E_{1,2}$, with the equations,

$$m_1 = \frac{E_2 M_{cn}}{E_1 + E_2} \qquad\qquad m_2 = \frac{E_1 M_{cn}}{E_1 + E_2}. \tag{4.16}$$

Provisional masses, μ_1 and μ_2, are calculated by modifying Equations 4.16, when anode pulse heights, P_{A1} and P_{A2}, are substituted for energies along with $M_{cn} = 239$,

$$\mu_1 = \frac{239 P_{A2}}{P_{A1} + P_{A2}} \qquad\qquad \mu_2 = \frac{239 P_{A1}}{P_{A1} + P_{A2}}. \tag{4.17}$$

The provisional fragment masses are used in the preliminary correction for neutron momentum transfer to determine calibration parameters. The product energies are corrected for neutron momentum by moving from the lab frame to the center of mass frame using the equation,

$$E_{1,2}^{cm} = E_{1,2}^{lab} \pm 2\frac{\sqrt{m_{1,2}m_n E_{1,2}^{lab} E_n^{lab}}}{m_{cn}} \cos\theta_{1,2}^{lab} + \frac{m_n m_{1,2}}{m_{cn}^2} E_n^{lab}. \tag{4.18}$$

The top sign (+) is for the upstream side and the bottom sign (−) is for the downsteam side, according to the detector orientation, which is determined next. The neutron mass, $m_n = 1.009$ AMU. These equations are taken from [53].

The angular distributions were compared to determine the detector orientation. For high incident neutron energies ($E_n > 10$ MeV), the angular distribution of the downstream detector volume should be more forward peaked in the lab frame. As expected, this was observed in the data for the backing side, shown in Figure 4.13.

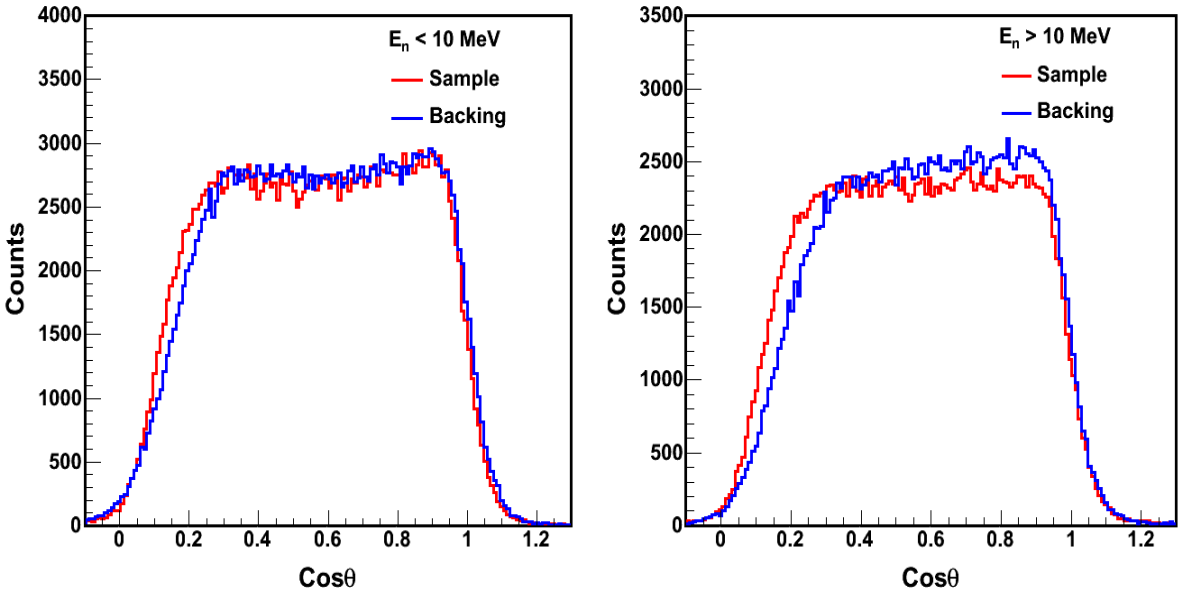

Figure 4.13: Angular distributions in the lab frame from the sample and backing side are compared to determine the sample orientation in beam. The backing side is downstream showing the angular distribution more forward peaked from additional high energy neutron momentum in the laboratory frame.

Equation 4.18 is modified by substituting in provisional masses μ_1 and μ_2 calculated in equations 4.17, substituting measured anode pulse heights P_{A1}^{lab} and P_{A2}^{lab} for energies, and by determining detector orientation to recover the neutron momentum corrected anode pulse heights $P_{A1,A2}^{cm}$ given by:

$$P_{A1}^{cm} = P_{A1} + 2\frac{\sqrt{\mu_1 m_n P_{A1} E_n}}{239}\cos\theta_1 + \frac{m_n \mu_{A1}}{239^2} E_n \tag{4.19}$$

and

$$P_{A2}^{cm} = P_{A2} - 2\frac{\sqrt{\mu_2 m_n P_{A2} E_n}}{239}\cos\theta_2 + \frac{m_n \mu_{A2}}{239^2} E_n. \tag{4.20}$$

Once the $P_{1,2}^{cm}$ are calculated, the final transition to the center of mass frame is done to recover center of mass angles $\cos\theta_{1,2}^{cm}$ using,

$$\cos\theta_{1,2}^{cm} = \sqrt{1 - \frac{E_{1,2}^{lab}}{E_{1,2}^{cm}}\left(1 - \cos^2\theta_{1,2}^{lab}\right)} \tag{4.21}$$

which is modified with provisional quantities in the same way as 4.18 to become

$$\cos\theta_1^{cm} = \sqrt{1 - \frac{P_{A1}}{P_{A1}^{cm}}\left(1 - \cos^2\theta_1\right)} \tag{4.22}$$

and

$$\cos\theta_2^{cm} = \sqrt{1 - \frac{P_{A2}}{P_{A2}^{cm}}\left(1 - \cos^2\theta_2\right)}. \tag{4.23}$$

A comparison of the raw anode pulse heights and neutron momentum corrected anode pulse heights is shown in Figure 4.14. Once the anode pulse heights and angles have been put into the center of mass frame, we proceed with further corrections for the energy loss in the backing and the gain calibrations.

4.3.2 Energy Loss Correction

The fission products detected on the backing side have lower energy on average than the sample side fragments because of straggling and additional energy loss in the backing material, but here, we correct for this effect. Fragments emitted at high angles tend to lose more energy because they pass through more target and/or backing material than fragments

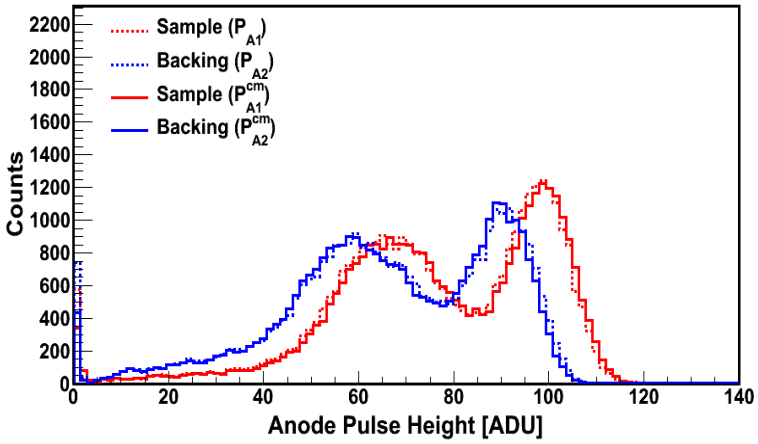

Figure 4.14: The raw (dotted) P_{A1} and P_{A2} are shown with the provisional neutron momentum corrected quantities P^{cm}_{A1} and P^{cm}_{A2} when $E_n = 1.5 - 2.0$ MeV.

emitted at smaller angles with respect to the beam axis. The amount of energy loss of the fragment through the material is proportional to the thickness of the material, shown in Figure 4.15.

From the geometric considerations of Figure 4.15, the thickness of material the fragment goes through is given by the relationship,

$$t = \frac{d}{\cos\theta} \tag{4.24}$$

Suppose the energy lost by a fragment in the material is given by P_t and is proportional to t, with a constant of proportionality $b(d)$,

$$P_t = \frac{b(d)}{\cos\theta}. \tag{4.25}$$

Further, the thickness of the material is a function of $1/\cos\theta$ so the final expression for anode pulse height of fragment in the ideal case is given by the equation,

$$P_{ideal} = P_A + P_t, \tag{4.26}$$

where P_{ideal} is the average anode pulse height in a situation where the fragment passes through no material and P_A is the average measured anode pulse height. This equation can

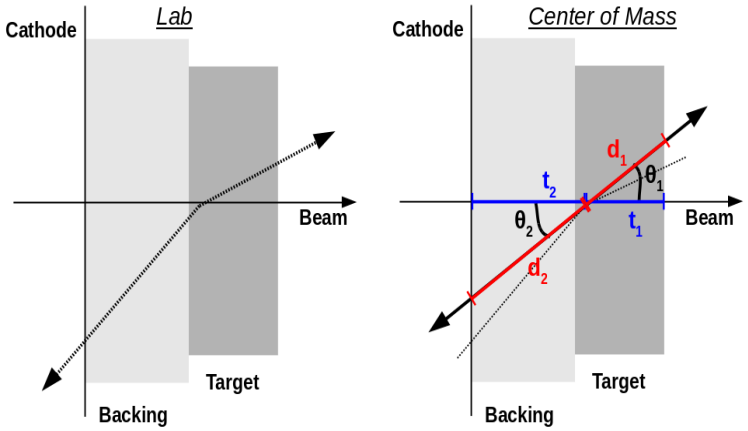

Figure 4.15: A schematic of the transition from the "Lab" frame to the "Center of Mass" frame where the fission fragments are emitted back to back. In the center of mass frame, the target orientation is shown along with the geometrical quantities, $d_{1,2}$, distances the fragments travel through the backing and target material before escaping into the gas, and $t_{1,2}$, the component of the distance along the beam direction.

be rearranged to get,

$$P_A = P_{ideal} - \frac{b}{\cos\theta}. \tag{4.27}$$

Suppose instead of P_{ideal}, the corrected anode pulse heights in both halves of the detectors can be calculated substituting P_{A1}^{b1} or P_{A2}^{b2} into Equation 4.27 to get,

$$P_{A1}^{b1} = P_{A1}^{cm} - \frac{b_1}{\cos\theta_1} \qquad\qquad P_{A1}^{b2} = P_{A2}^{cm} - \frac{b_2}{\cos\theta_2} \tag{4.28}$$

so the final expressions for the corrected P_{A1}^{b1} and P_{A2}^{b2} is simply the sum of the measured anode pulse height and the extra energy removed by the $b/\cos\theta$ term. The parameters b_1 and b_2 are determined by plotting neutron-momentum corrected average anode pulse heights as a function of $1/cos\theta$ for both detector halves for $E_n = 1.5 - 2.0$ MeV. Then a linear fit is applied to recover the parameters. The y-intercept, P_{ideal}, is fixed to the target-side fit value so only b_2 is allowed to vary on the backing side fit. Final parameters for both isotopes are shown in Table Table 4.2. The fits are shown in Figure 4.16.

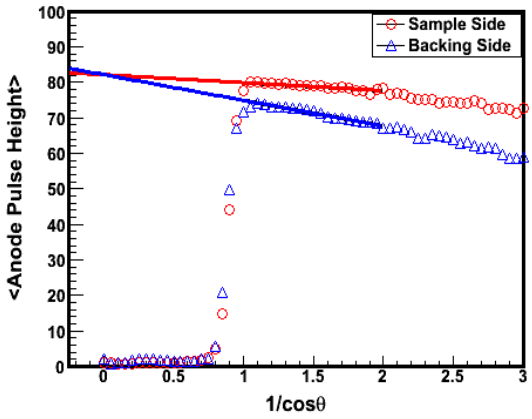

Figure 4.16: The average energy of the sample $< P_{A1}^{cm} >$ (red) and backing $< P_{A2}^{cm} >$ (blue) side fragments are plotted as a function of $1/(\cos\theta)$ to determine the amount of energy loss in the target material. The data was fit between values of $1/(\cos\theta) = 1.0 - 2.0$ to determine the parameters b_1 and b_2, the slopes of the linear fit .

Figure 4.17 shows the momentum and energy loss corrected anode signals for $E_n = 1.5 - 2.0$ MeV. Since the distributions do not overlap, one more correction for gain is required,

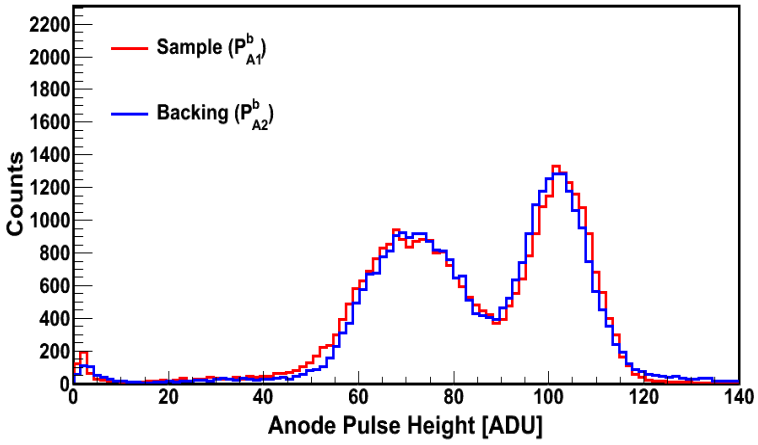

Figure 4.17: The calibrated pulse height spectrum after all energy loss corrections are applied at $E_n = 1.5 - 2.0$ MeV.

discussed in the next section.

4.3.3 Gain Calibration

A small correction for differences in the preamp gain is made by calibrating the backing side spectrum to the sample side anode spectrum. Before the gain calibrations, additional selection criteria were applied to the data based on anode pulse height ($P_{A1,A2} \geq 30$ ADU) and angle of emission ($\cos\theta_{1,2} \geq 0.5$). These cuts are for quality control and are later applied to all data before the full 2E method, described in detail in Section 4.5.1.

Like an energy calibration, the gain calibration is assumed to be linear and follows the equation,

$$P_{A2}^{cal} = G_a\left(P_{A2}^{b}\right) + G_b, \tag{4.29}$$

where G_a and G_b are calibration parameters to be determined. P_{A2}^{b} are the energy loss corrected pulse heights calculated in the last section for the backing side, which is to be the only side affected by the gain calibration. To find G_a and G_b, both the sample and backing side of the anode spectrum shown in Figure 4.18 are fit with Gaussians.

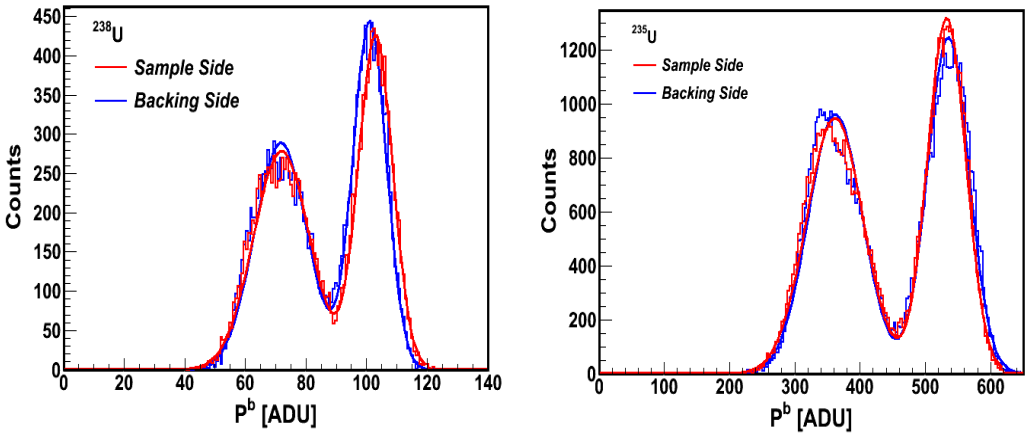

Figure 4.18: The P_{A1}^{b} and P_{A2}^{b} spectra for both targets with quality cuts and fit with Gaussians. The centroids of these Gaussians will be used to calibrate the backing side to the sample side.

This procedure extracts the centroids from the heavy peaks (H_1 and H_2) and the light peaks (L_1 and L_2). Then the calibration equation parameters are derived from a line that runs through the points p1 = (H_2,H_1) and p2 = (L_2,L_1) shown in Figure 4.19.

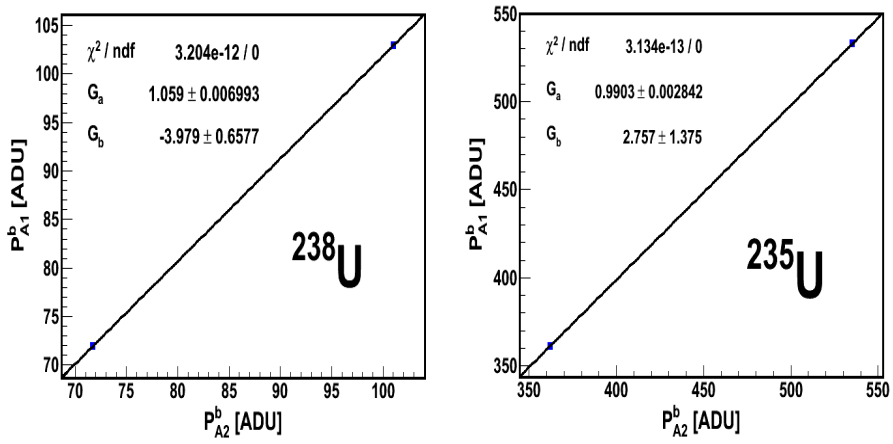

Figure 4.19: Fit to calibrate the backing side digitizer units to the sample side digitizer units using the linear equation $P^b_{A1} = G_a P^b_{A2} + G_b$.

The final corrected anode pulse height spectrum is shown in Figure 4.20.

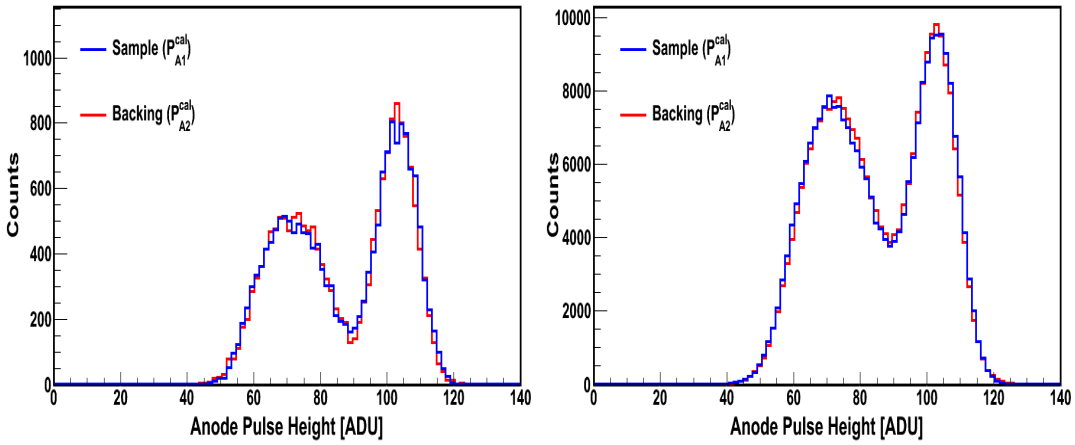

Figure 4.20: The calibrated pulse height spectrum after all corrections are applied at $E_n = 1.5 - 2.0$ MeV (left) and for ALL the E_n (right) to show the corrections can be extended to higher energies.

4.4 Energy Calibration

Until this point in the analysis, the energies of the fragments have been considered in terms of anode pulse heights in arbitrary digitizer units (ADU). An energy calibration is required to change the anode pulse height in ADU into energies in MeV. The method of determining the calibration parameters for each isotope is described in Section 4.4.1. In

Section 4.4.2, the parameters are applied to the neutron momentum corrected anode pulse heights (P_{A1}^{cor}, P_{A2}^{cor}) along with the other anode correction factors determined in Section 4.3. The calibration equation is determined for events with $E_n = 1.5 - 2.0$ MeV since that introduces the least amount of uncertainty due to the provisional momentum correction. The parameters are then applied to events at all incident neutron energies.

4.4.1 Determine Calibration Constants

Since the average energies of light (E_L) and heavy (E_H) fission fragments have been previously measured at specific incident neutron energies for both uranium isotopes, a small subset of the data at the specified E_n can be used to determine the calibration parameters. The final ADU-to-MeV calibration is calculated by establishing a linear relationship between the light and heavy peaks of the anode spectra and the previously measured values for E_H and E_L.

The average energies of the light and heavy fragments are required with a correction factor. For ^{238}U, the heavy and light fission product energy data of Vives et. al. are used for calibration at $E_n = 1.5 - 2.0$ MeV [33]. An averaging of the data points in this energy range gives, $E_H = 70.9 \pm 0.05$ MeV and $E_L = 95.5 \pm 0.07$ MeV. For ^{235}U, a calculation of $TKE(A)$ at $E_n = 5.5$ MeV by P. Talou was used for calibration [54]. In this case, the average light fragment mass was assumed to be $m_L = 99$ AMU with a corresponding energy of$E_L = 100.2 \pm 0.5$ MeV. For the heavy fragment, $m_H = 139$ AMU with a corresponding energy of $E_H = 69.9 \pm 0.3$ MeV. The typical ionization chamber value of 0.5% energy resolution is used to determine the uncertainty.

It is important to note that later in the analysis, we are going to be correcting fragment energy E, because of the pulse height defect PHD, discussed in detail in section 4.5.4, using the equation $E^{cor} = E + PHD(m)$. Pulse height defect is a detector effect due to non-ionizing collisions in the gas and ion recombination. As a result, the raw measured P_A value is a representation of the fragment energy before the PHD correction. It is a non-linear mass dependent effect, which is why a linear calibration of P_A to E^{cor} will not accurately

correct for PHD. To accurately calibrate P_A to energy, we should compare it to a previously measured energy that is also missing some energy due to PHD. Since the values are typically not reported, the reported data will be manipulated to remove the PHD correction. The energy loss due to pulse height defect for the average light fragment mass of 100 AMU is $PHD_L = 3.7 \pm 0.05$ MeV and for the average heavy fragment mass of 140 AMU is is $PHD_H = 4.29 \pm 0.03$ MeV, according to the PHD(A) curve in 4.5.4. The correction is applied and uncertainties quantified using equations,

$$E_L^{cor} = (E_L \pm \delta E_L) - (PHD_L \pm \delta PHD_L) \quad E_H^{cor} = (E_H \pm \delta E_H) - (PHD_H \pm \delta PHD_H) \tag{4.30}$$

For ^{238}U at $E_n = 1.5 - 2.0$ MeV, $E_L^{cor} = 95.50 \pm 0.07$ MeV and $E_H^{cor} = 66.61 \pm 0.06$ MeV. Uncertainties were added in quadrature.

As with the gain calibration, the goal is to extract the centroids from the heavy peaks (H_1 and H_2) and the light peaks (L_1 and L_2), from Figure 4.21. Since the P_A's are calibrated,

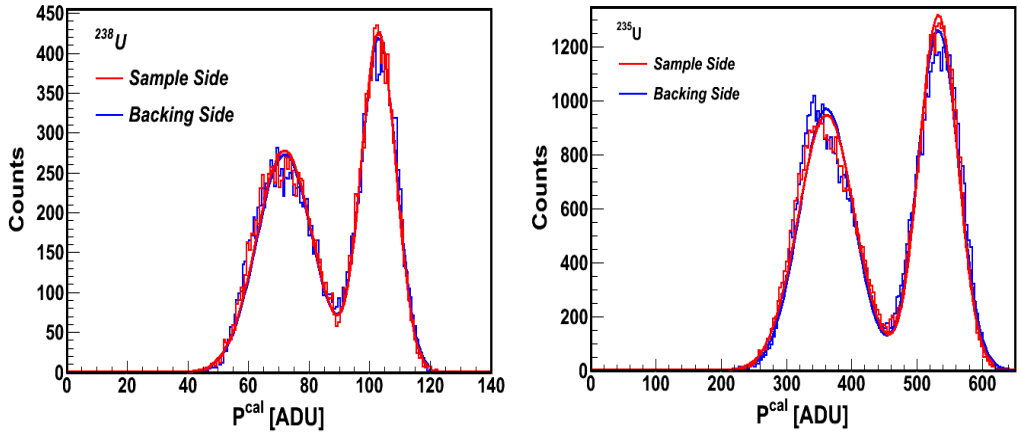

Figure 4.21: The sum of two Gaussians are used for fits to P^{cal} for the sample and backing sides. The locations of the heavy and the light peak are averaged for both and used as calibration parameters.

these are almost identical, but we take the averages nonetheless to get $P_H = 74.75 \pm 0.17$ ADU and $P_L = 105. \pm 0.11$ ADU for ^{238}U. Then compare with the previous data E_H^{cor} and E_L^{cor}. The calibration equation parameters come from a line that runs through the points p1

= (P_H, E_H^{cor}) and p2=(P_L, E_L^{cor}) shown in Figure 4.22. Uncertainties are taken into account in the fitting process.

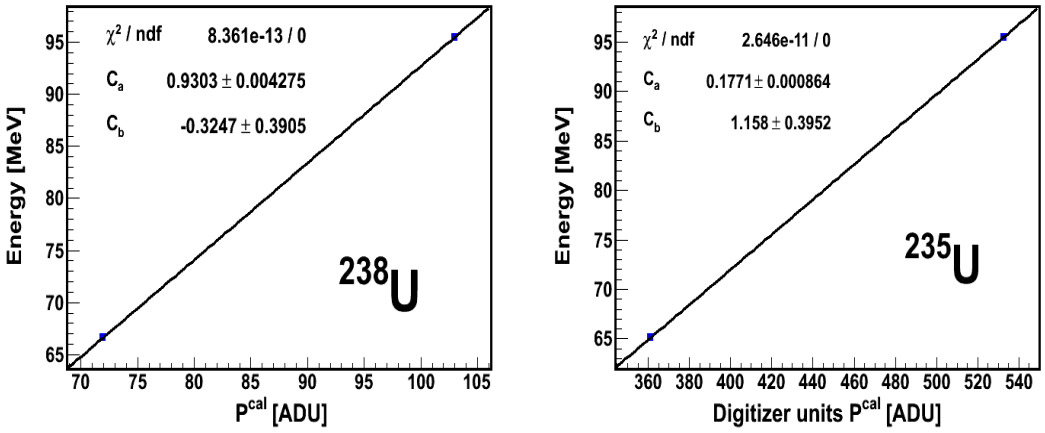

Figure 4.22: Fit to calibrate the digitizer units to the energy units using the linear equation $E = C_a P_A^{cal} + C_b$.

The final energy is dependent on an additional pulse height defect correction, but this correction is mass dependent so must be performed later in the analysis.

4.4.2 Complete Energy Calibration and Momentum Correction

In this step, the anode pulse heights, P_{A1} and P_{A2}, are converted into calibrated energies, E_1 and E_2, using correction and calibration parameters determined in Sections 4.3 and 4.4 for low energy events. Events of all incident neutron energies, E_n, can be corrected by assuming that fission products react the same way to detector effects once their angles and energies are corrected for neutron momentum. Thus, the same detector calibration and correction parameters apply at high E_n as at low E_n.

First, a correction for incident neutron momentum is made using provisional masses from Equations 4.17, Center of Mass angles from Equations 4.21, and Equations 4.18 for corrected P_{A1}^{cm} and P_{A2}^{cm} at all E_n. The calibration parameters are displayed for the two uranium isotopes in Table Table 4.2. The calibrated energies E_1^{cal} and E_2^{cal} are then calculated using Equations 4.31 and 4.32 by substituting in the appropriate parameters, P_{A1}^{cm}, P_{A2}^{cm}, $\cos\theta_1^{cm}$,

and $\cos\theta_2^{cm}$.

The final correction equation, which incorporates momentum, energy loss, gain matching, and calibration has the form,

$$E_1^{cal} = C_a(P_1^{cm} - \frac{b_1}{\cos\theta_1}) + C_b, \tag{4.31}$$

while the form is slightly different for the backing side,

$$E_2^{cal} = C_a(G_a(P_2^{cm} - \frac{b_2}{\cos\theta_2}) + G_b) + C_b, \tag{4.32}$$

where $C_a = 0.930 \pm 0.004$ and $C_b = -0.3 \pm 0.4$ are from the channel to energy calibration equation, $G_a = 1.059$ and $G_b = -3.97$ is the gain matching correction, and $b_1 = -2.3 \pm 0.7$ and $b_2 = -7.24 \pm 0.14$ are from the energy loss correction. After applying the 2E method, which calculates masses by applying a prompt neutron correction, the yields also overlap, indicating the corrections were accurate. Following the energy loss and calibration corrections we again examine the anode pulse heights as a function of angle. Since the backing side was especially corrected for energy loss, it should appear identical to the sample side as two rectangular bars, which is confirmed in Figure 4.23.

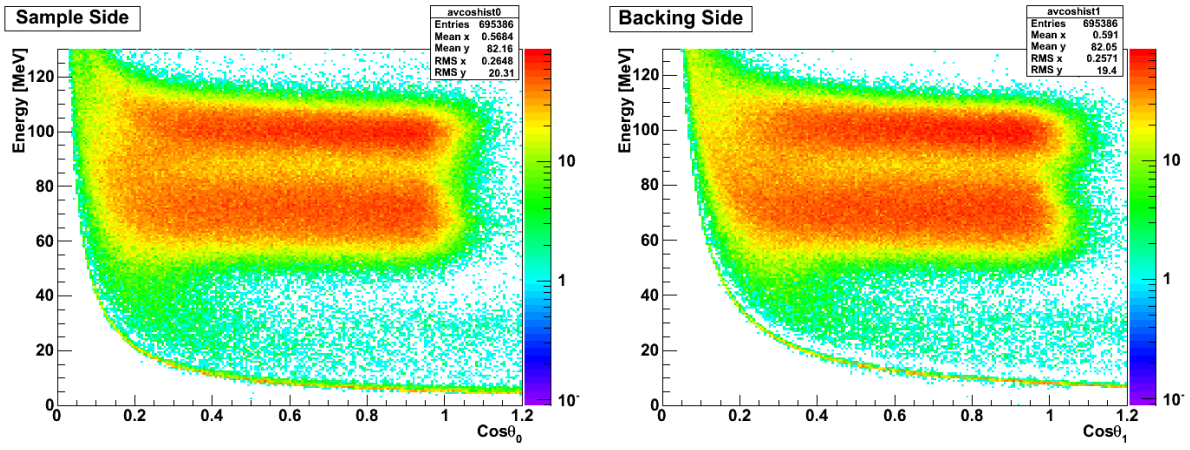

Figure 4.23: The angular and energy loss dependencies have been eliminated from the data, indicated by the similarity in both the sample and backing side of the detector when fragment energy is examined as a function of fragment angle (lab).

Table 4.2: A list of the calibration and correction parameters.

Isotope	b_1	b_2	G_a	G_b	C_a	C_b
^{235}U	-16.99	-60.71	0.969	-6.4	0.187 ± 0.008	-1.6 ± 0.3
^{238}U	-2.26	-7.24	1.059	-3.97	0.9303 ± 0.004	-0.3 ± 0.4

With the energies and angles of the fission products now determined, we proceed to calculate the fragment mass m_1^{pre} and m_2^{pre} using the 2E method.

4.5 The 2E Method

The 2E method calculates the pre-prompt neutron emission mass yield distributions using the fission products' energies and angles in kinematic equations. This iterative procedure also makes mass dependent corrections such as prompt neutron evaporation and pulse height defect. The process is outlined in Table 4.3.

Table 4.3: A summary of 2E analysis procedures.

Step	**Description**	**Input**	**Output**
Data selection Section 4.5.1.	Set angular and anode thresholds to cut out light charged particles and events with straggling.	Complete data set	Subset of quality data
Multi-chance fission treatment Section 4.5.2	Select the mass of the compound nucleus using multi-chance fission probabilities for a given E_n and set the symmetric fission initial condition.	E_n	M_{cn}, m_1^{pre}, m_2^{pre}
Prompt-neutron correction Section 4.5.3	Subtract the appropriate number of neutrons from the fragment mass to calculate the product masses.	m_1^{pre}, m_2^{pre}, $\nu(E_n, m^{pre})$	m_1^{post}, m_2^{post}
Pulse height defect correction 4.5.4	Add the missing pulse height defect energy back to the measured energy	E_1, E_2, $PHD(m^{post})$	E_1^{post}, E_2^{post}
Recalculate fragment mass 4.5.5	Use the calculated quantities to find a new m^{pre}	E_1^{post}, E_2^{post}, m_1^{pre}, m_2^{pre}, m_1^{post}, m_2^{post}	m_1^{pre}, m_2^{pre}
Test for convergence 4.5.6	Compare the pre-neutron mass at the beginning and the end of the loop.	m_{before}^{pre}, m_{after}^{pre}	break or continue

4.5.1 Data Selection

Aggressive selection criteria based on the anode pulse height and emission angle were applied to the data before further processing. Recall that anode pulse height (P_A) is proportional to particle energy. By restricting the anode to P_{A1} and $P_{A2} \geq 40$ arbitrary digitizer units (ADU), low energy events are not processed in the 2E method. This cut was selected based on the appearance of the calibrated anode spectrum, shown on the right in Figure 4.24. Events with $P_A \geq 40$ ADU are fission products while events with $P_A \leq 40$ ADU are most

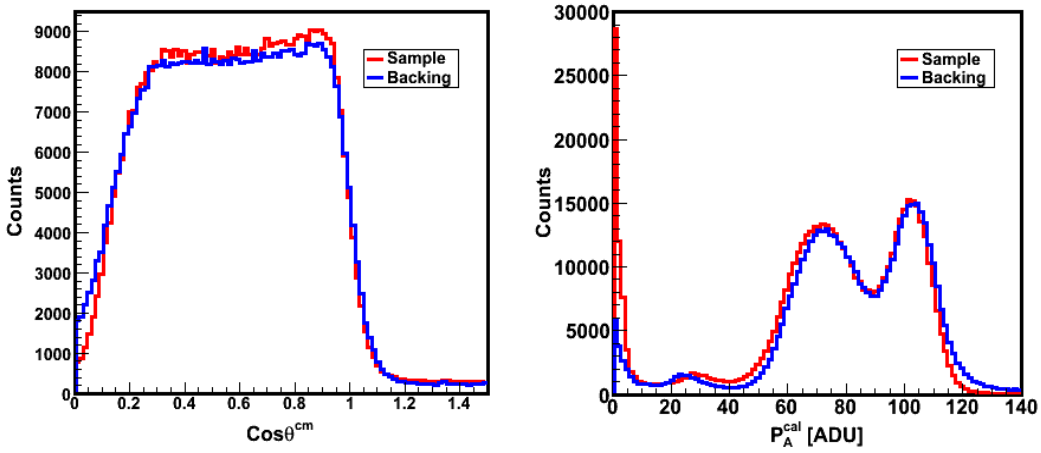

Figure 4.24: The $\cos\theta$ distributions and the P_A^{cal} spectra at all incident neutron energies.

likely light charged particles and alphas. No upper limit is imposed.

The angular cut is for $\cos\theta_1$ and $\cos\theta_2 \geq 0.5$. This cut was selected based on the appearance of the angle spectrum shown in Figure 4.24. Note that the rising edge of the angular spectrum in Figure 4.24 only begins to flatten out around $\cos\theta = 0.3$. Recall from Section 4.2 that fragments emitted at very steep angles (low values of $\cos\theta$) tend to travel through more material and therefore have a higher probability of being caught in the backing or losing a significant portion of the energy. The cut is extended to $\cos\theta = 0.5$ to ensure that only fragments with minimal energy loss are used in the final calculation. No upper limit is imposed.

By selecting conditions for both sides of the chamber, we ensure that the only events processed are coincident fragments that suffered minimal interference from detector effects. The selected, good data looks like Figure 4.25.

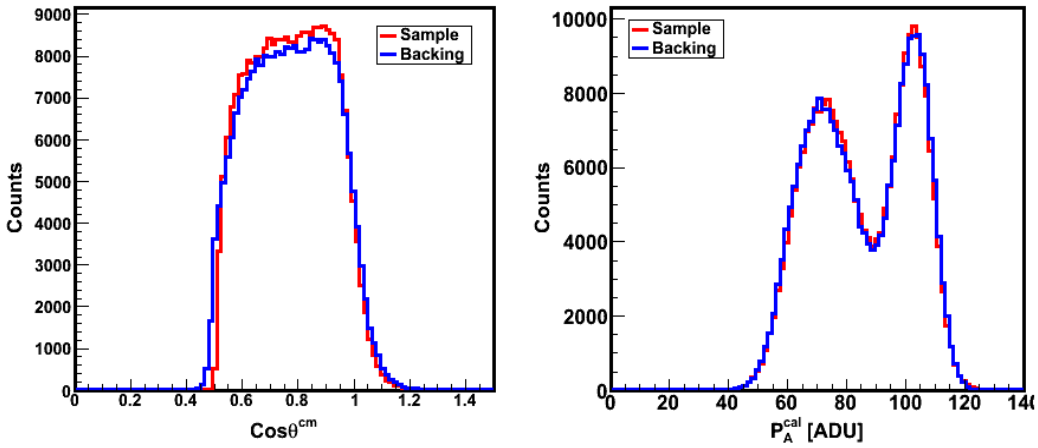

Figure 4.25: The $\cos\theta$ distributions and the P_A^{cal} spectra at all incident neutron energies after selecting the data. Some angles are less than $\cos\theta = 0.5$ because selections were made on the raw angle and the provisional momentum corrected angle is shown here.

4.5.2 Multiple Chance Fission Treatment

The 2E process begins by initially assuming that the fission fragments are symmetric, that is half the atomic mass of the compound nucleus M_{cn},

$$m_1^{pre} = m_2^{pre} = M_{cn}/2. \tag{4.33}$$

We can then enter into the iteration process until the convergence condition of $|m_i^{pre}$(after) - m_i^{pre}(before)$| \leq 0.125$ is satisfied where $i = 1$ or 2 since there are two fragments.

The compound nuclear mass changes because multi-chance fission and other light particle emissions become probable with higher neutron energies. To account for this behavior, the fission probabilities were simulated in GEF at E_n=1 MeV intervals or larger, scaling up with the experiment's neutron energy resolution. The GEF code is the General Description of Fission Observables [55], which does empirical simulations based on existing fission data. Where some data exists, the simulations are typically good quality. Thresholds for multi-

chance fission were determined using the ENDF cross section [1] when the steep rises at the second-, third-, and multi-chance thresholds were more than 50% of the cross section's previous plateau value. Evaluated cross sections are shown in Figure 4.26.

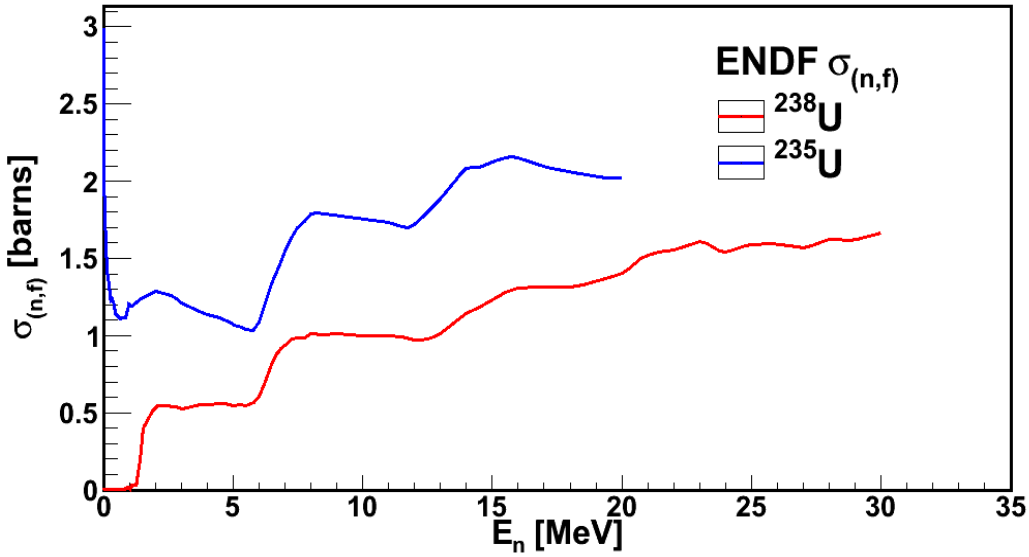

Figure 4.26: The neutron-induced fission cross section, $\sigma_{(n,f)}$ as a function of E_n is shown for ^{235}U (blue) and ^{235}U (red) [1]. The first-, second-, and third-chance fission thresholds are clearly seen as steps in the cross sections around E_n = 1.5, 7, and 14 MeV.

When the evaluation stopped at $E_n > 20$ MeV for ^{235}U and $E_n > 30$ MeV for ^{238}U, the energy ranges were adjusted so that the standard deviations of the M_{cn} average probabilities were minimized. The various probabilities of fission chances and light particle emissions resulting in the same compound nucleus were averaged within these ranges. A Monte Carlo Code selected the starting compound nucleus by sampling the average probabilities of starting with a particular compound nucleus within the specified energy range, shown in Table 4.4 for ^{238}U and in Table 4.5. High energy measurements do not exist so complete simulations cannot be performed for ^{235}U at $E_n > 60$ MeV. In this case, we use the results for ^{238}U adapted to the -3n case.

Table 4.4: Average probabilities for a compound nucleus for given incident E_n range for ^{238}U(n,f) calculated using input from [55] [1].

E_n [MeV]	239(%)	238(%)	237(%)	236(%)	235(%)	234(%)	233(%)	232(%)
0 - 6	100	-	-	-	-	-	-	-
6 - 13	50	50	-	-	-	-	-	-
13 - 18	35	49	16	-	-	-	-	-
18 - 32.5	16	33	27	24	-	-	-	-
32.5 - 42.5	8	18	22	28	19	5	-	-
42.5 - 55	6	12	17	21	24	17	3	-
55 100	2	7	10	13	18	19	18	13

Table 4.5: Average probabilities for a compound nucleus for given incident E_n range for ^{235}U(n,f) calculated using input from [55] [1].

E_n [MeV]	236(%)	235(%)	234(%)	233(%)	232(%)	231(%)	230(%)	229(%)
0 - 6	100	-	-	-	-	-	-	-
6 - 13	65	35	-	-	-	-	-	-
13 - 19.5	33	43	24	-	-	-	-	-
19.5 - 32.5	16	37	37	10	-	-	-	-
32.5 - 42.5	7	22	32	29	10	-	-	-
42.5 - 55	5	15	24	28	22	6	-	-
55 - 100	2	7	10	13	18	19	18	13

4.5.3 Prompt Neutron Corrections

Recall from Section 2.1 that when the compound nucleus first divides into the two fragments, the excess excitation energy dissipates through evaporation of prompt neutrons and gammas. Therefore, calculating the mass of the fission product requires a neutron evaporation correction through using values from the so-called neutron sawtooth ($\nu(A)$), displayed in Figure 4.27. This includes an evaluation of $\nu(A)$ experimental data for ^{233}U and ^{233}U at E_n = thermal [56] and a calculation of the ^{233}U sawtooth [57]. Very little experimental data exists for $\nu(A)$ for any isotope at any E_n. The average number of prompt neutrons, $\nu(m_i^{post}, E_n)$, emitted during fission varies with the mass of the fission fragment and the energy of the incident neutron, but typically displaying a sawtooth shape, shown in Figure 4.27 for ^{238}U at E_n =thermal. They are subtracted from the pre-neutron evaporation fragment

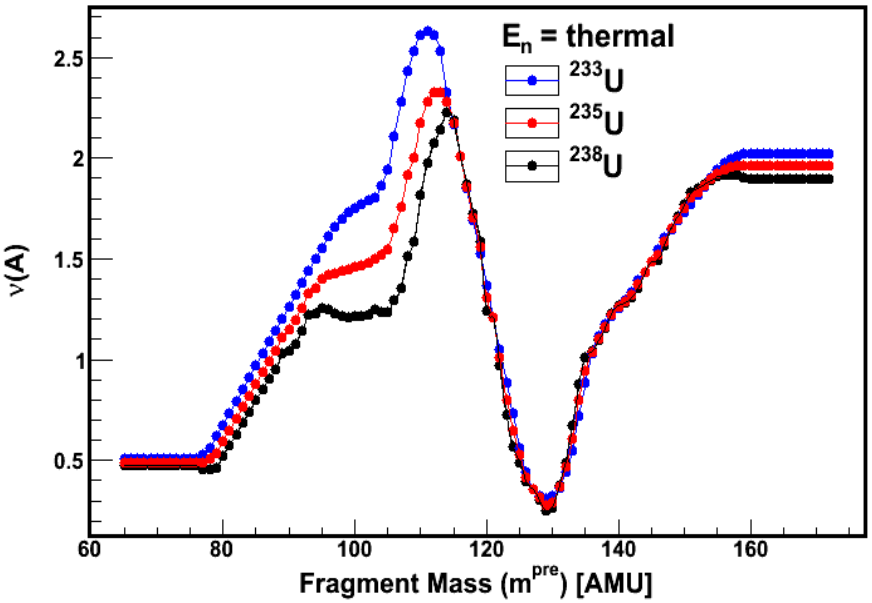

Figure 4.27: The neutron sawtooth for ^{238}U, calculated from experimental data for ^{235}U and ^{233}U and E_n = thermal using the observations of [56] and calculation method of [57].

mass using equations,

$$m_1^{post} = m_1^{pre} - \nu(m_1^{pre}, E_n) \qquad m_2^{post} = m_2^{pre} - \nu(m_2^{pre}, E_n). \tag{4.34}$$

The neutron sawtooth has this shape due to nuclear shell structure. The sharp dip at $m^{pre} = 132$ AMU is largely due to ^{132}Sn, a common double magic fission fragment which is unlikely to evaporate any prompt neutrons. To perform the correction, a $\nu(m_i^{post}, E_n)$ curve is selected based on incident neutron energy. Based on the m^{pre} from the initial condition (Equation 4.33) or the previous iteration (Equation 4.37), an interpolation method selects the appropriate corresponding $\nu(m_i^{post}, E_n)$.

The average number of prompt neutrons evaporated per fission fragment as a function of fragment mass, or the "sawtooth" has proven difficult to measure experimentally and is one of the main sources of systematic uncertainty in calculating fragment mass. In fact, no measurement of the ^{238}U sawtooth exists and ^{235}U has been measured only at thermal incident neutron energies [56]. Because the WNR measurement takes place at energies above

thermal, two methods were compared to deduce the shape of the neutron sawtooth correction, 1) the scaling method and 2) the GEF method, described below.

Previous 2E method studies on ^{238}U(n,f) have scaled a thermal sawtooth derived in calculations from measured data at thermal energy for other uranium isotopes [56] [57]. The scaling method is outlined in the model work of Lestone [37] and involves multiplying each point along the thermal neutron sawtooth with a scaling factor chosen to keep the *total* average number of neutrons emitted in fission, $\bar{\nu}(E_n)$ consistent with previously measured experimental values. A selection of sawteeth at selected E_n are shown in Figure 4.28. The

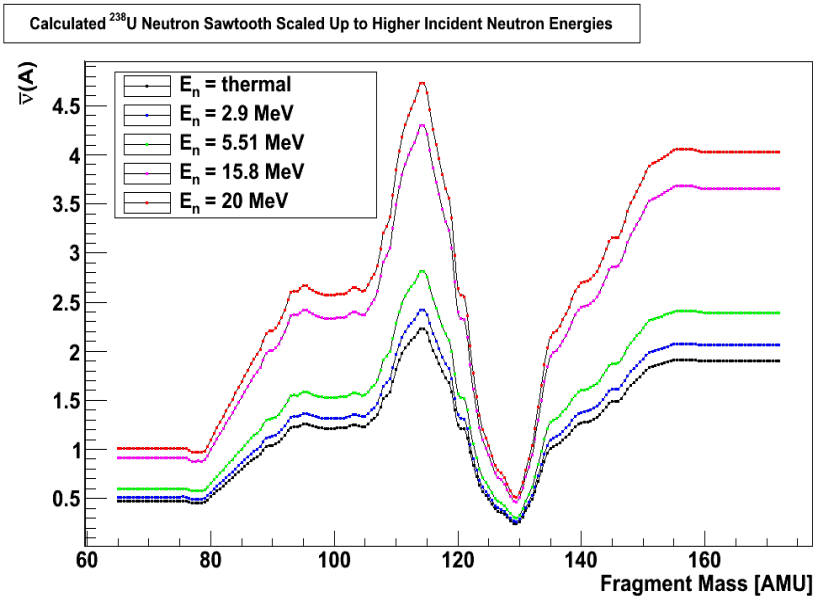

Figure 4.28: The neutron sawtooth for ^{238}U, calculated thermal incident neutrons using the methods in [56] [57] and scaled using the method of [37].

$\bar{\nu}(E_n)$ corresponds to the integral under the $\nu(m_i^{post}, E_n)$ curve. However, the scaling method fails to capture the behavior that more neutrons are evaporated from the heavy fragment at energies higher than thermal, observed in [58] [59] and more recently modeled in [60], [61], [62].

In this work, the sawtooth is simulated using GEF, The General Description of Fission Observables, as described in the previous section [55]. The GEF sawtooth simulations evaporate substantially more neutrons from the heavy fragment at fast neutron energies than the

scaling method. Several GEF sawteeth are shown in Figure 4.29. Since it would take too

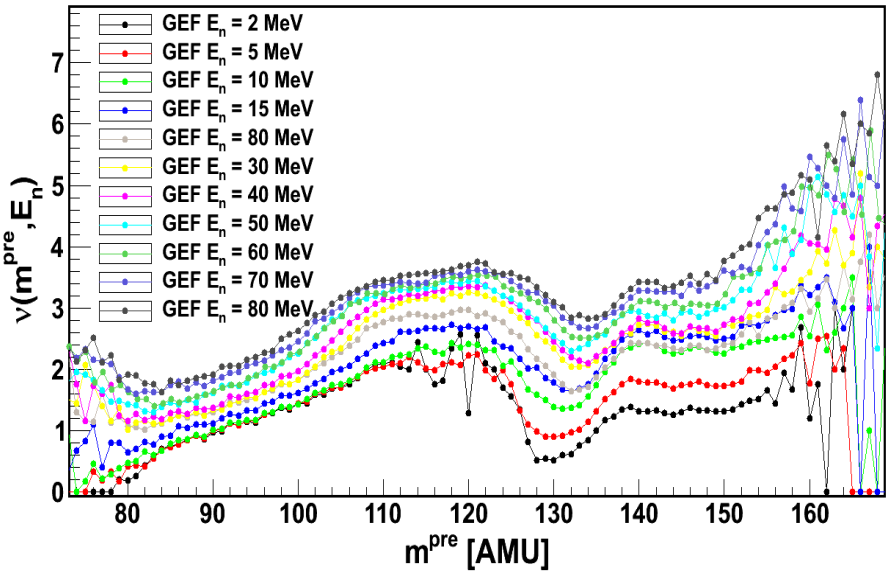

Figure 4.29: GEF simulations of the neutron sawtooth for ^{238}U at various E_n. The connecting lines between points are to guide the eye. Oscillations are an artifact of the simulation.

much computing power to simulate the sawtooth for each minute change in E_n, the sawtooth was simulated for ranges of energies larger than the timing resolution of the detector. For ^{238}U, the sawtooth was simulated at E_n = 1, 2, 3, 4, 5, 6, 7, 8, 9, 10, 11, 12, 13, 14, 15, 16, 18, 20, 22, 24, 26, 28, 30, 35, 40, 50, 60, 70, 80, and 90 MeV and for ^{235}U at E_n = thermal, 1, 2, 3, 4, 5, 6, 7, 8, 9, 10, 11, 12, 13, 14, 15, 16, 18, 20, 22, 24, 26, 28, 30, 35, 40, 45, 50, 61, 70 MeV. The sawtooth for a particular E_n is applied to events with an energy range ending halfway between itself and the next or previous energy. For example, the E_n = 30 MeV sawtooth would be applied to events in a range from $E_n = 29 - 32.5$ MeV since other sawteeth are available at both E_n = 28 MeV and E_n = 35 MeV. Like the scaling method, interpolation between the points is used to extract the appropriate value of ν.

The scaling method and the GEF simulations were compared during this work on ^{238}U. A comparison of neutron sawteeth using the two methods are shown in Figure 4.30. The diminishing effects of shell structure (the dip at m^{pre} = 132 AMU) in the GEF simulations suggest that this method is more correct since the compound nucleus does not equilibrate at

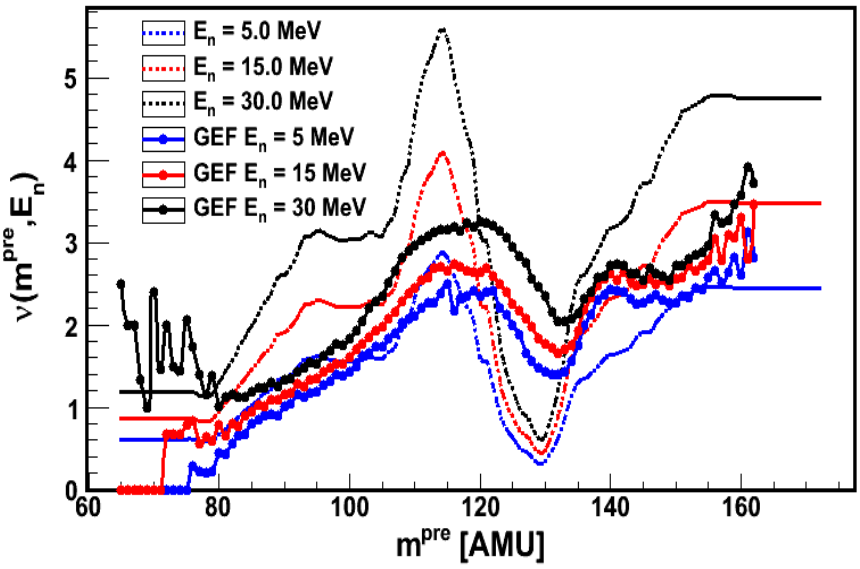

Figure 4.30: A comparison between the GEF and calculated sawtooth methods in ^{238}U. No experiments are available for comparison.

high E_n as discussed in Chapter 2. The simulated GEF sawteeth result in higher pre-neutron emission yield in the valley. This observation is in agreement with a prior study of prompt neutron corrections in the 2E method [63]. Their effects on the mass distributions are shown in Figure 4.31. It should be noted that until the $\nu(m^{pre}, E_n)$ is measured experimentally for a range of E_n, it is difficult to draw conclusions about the evolving behavior of the sawtooth.

4.5.4 Pulse Height Defect

Pulse Height Defect (PHD), mentioned earlier in Section 4.4, is a mass dependent correction to the energy that needs to be accounted for in the 2E method. It corrects for recombination of the ions in the gas and non-ionizing collisions, which causes the fragment to deposit a few % less than its total energy in ionizing action transmitted to the anode. The correction is necessary to get the actual post-neutron emission energies,

$$E_1^{post} = E_1^{cal} + PHD(m_1) \qquad\qquad E_2^{post} = E_2^{cal} + PHD(m_2). \tag{4.35}$$

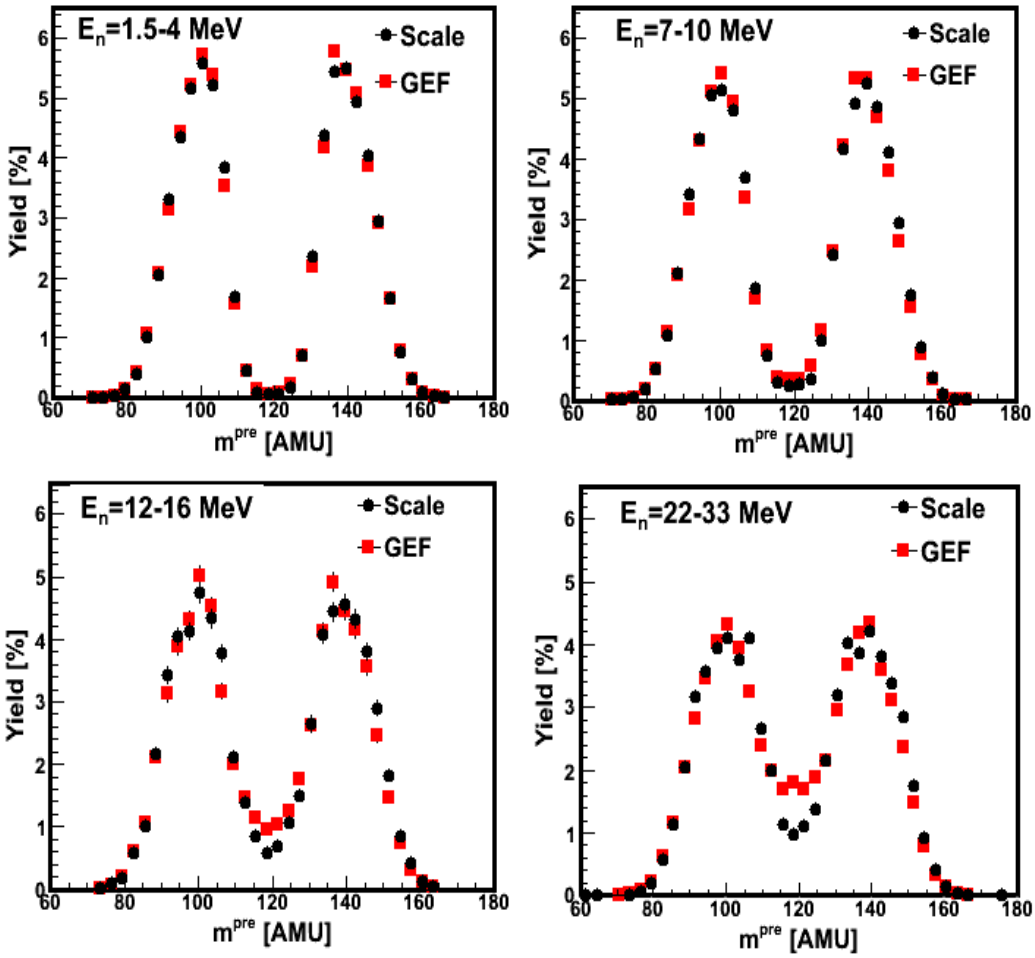

Figure 4.31: A comparison between the GEF and scaled sawtooth methods in ^{238}U when applied to the data in the 2E method. As expected, the scaled method leads to lower yield in the valley since it evaporates more neutrons in this mass region.

The PHD curve in Figure 4.32 was measured in an identical ionization chamber in another experiment [8]. To extract the PHD, an interpolation technique applied to the curve in Figure 4.32 retrieves the appropriate value based on the input mass.

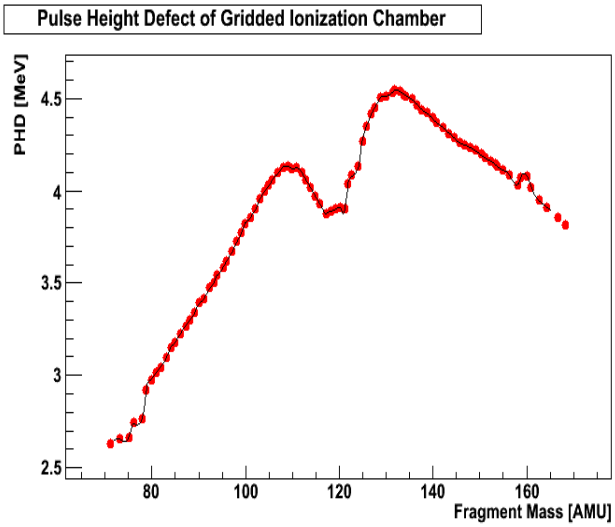

Figure 4.32: Pulse heigh defect curve taken from [8].

Other methods have been developed to empirically calculate pulse height defect, however PHD varies with many parameters such as gas pressure, gas composition, electric field in the chamber [64] [65]. It also varies with fragment masses and energies, so it has proven to be a difficult problem. A full study of PHD could be made with a variable mass heavy ion beam into an ionization chamber under various conditions to truly study this technical challenge.

4.5.5 Recalculate Fragment Masses

Once the pre- and post-neutron evaporation masses from Equations 4.33 and 4.34 are determined, conservation of mass and energy are used to derive an expression to calculate the new pre-neutron evaporation fragment mass that accounts for the corrected energies from Equation 4.35. The full derivation can be found in [8]. Calculate B, a ratio between the two fragment masses,

$$B = (m_2^{pre} * m_1^{post})/(m_2^{post} * m_1^{pre}). \tag{4.36}$$

Calculate m_i^{pre} using B,

$$m_1^{pre} = \frac{M_{cn} E_2^{post}}{E_1^{post}/(B) + E_2^{post}} \tag{4.37}$$

$$m_2^{pre} = \frac{M_{cn} E_1^{post}}{E_2^{post}(B) + E_1^{post}}, \tag{4.38}$$

which express pre-prompt neutron masses in terms of observables and assumptions. The pre-prompt lab energies are calculated using

$$E_{1,2}^{lab} = \frac{m_{1,2}^{pre}}{m_{1,2}^{post}} E_{1,2}^{post}, \tag{4.39}$$

which can then be converted to the CM frame using equation 4.18. The first iteration of the 2E code used the initial condition from 4.33 for m_i^{pre}, however each subsequent iteration will use the new m_i^{pre} calculated in 4.37 as the initial mass. This step effectually checks the calculated mass against the measured energy until the assumed mass at the beginning of the iteration and final calculated mass are nearly the same, which is tested by the convergence condition in the next step.

4.5.6 Check for convergence

Check the convergence condition, $|m_i^{pre}(\text{after}) - m_i^{pre}(\text{before})| \leq 0.125$. This value is chosen to maximize accuracy while minimizing computation time. Each iteration, the calculation of m_i^{pre} will be more closely correlated with the measurement of E_i^{post}. When convergence is reached, corrected values of m_1^{pre}, m_2^{pre}, m_1^{post}, m_2^{post}, E_1^{pre}, E_2^{pre}, E_1^{post}, and E_2^{post} are available for further physics analysis.

4.6 Charge Correction

The results of the 2E mass calculations are shown in Figure 4.33 for ^{238}U. Here, the rectangular energy bars seen earlier in Figure 4.23 are converted to masses. The angled ends at values of $\cos\theta = 1.0$ are due to fragment charge variations which can be corrected using the same method described earlier in Section 4.2 to calculate $\overline{X}/D$. This time, the energies

are plotted as a function of angle and projected onto the angle axis. The resulting final mass vs. angular distribution is shown in Figure 4.33. As expected, it now exhibits the same rectangle bar behavior as the energy vs. angle distribution in Figure 4.23.

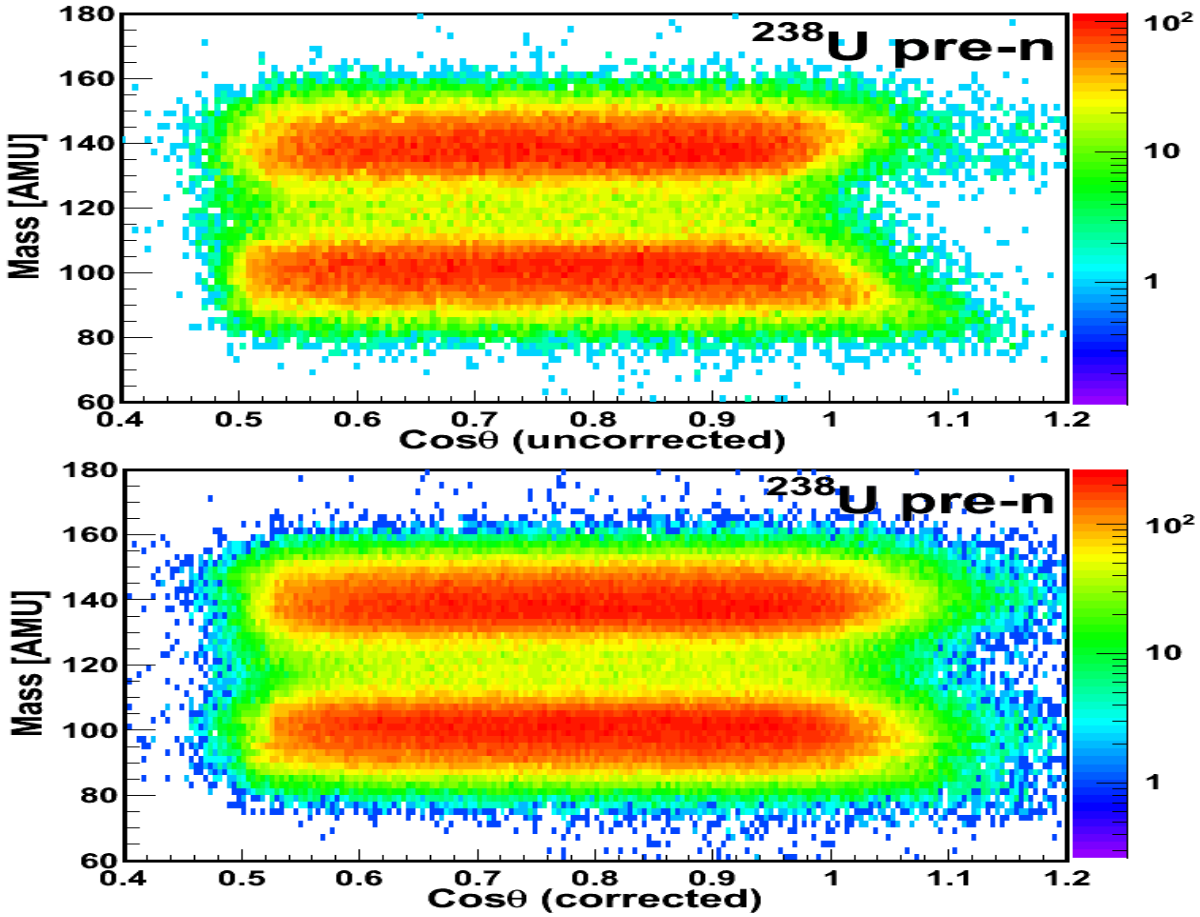

Figure 4.33: The final distribution of fragment masses with emission angles before (top) and after (bottom) charge correction. The angles are in the CM frame and the masses are for fragments pre-neutron emission.

4.7 Physics Calculations

To calculate the $\overline{TKE}$, the sum of the heavy and light fragment energies was computed to get a TKE spectrum, e.g. $TKE = E_1 + E_2$. A histogram of TKE for a given neutron energy range was then generated and fit with a Gaussian distribution,

$$G(x) = A \exp\left(\left(-0.5 * \frac{(x - TKE)}{\sigma}\right)^2\right). \tag{4.40}$$

A typical example of a ^{238}U TKE distribution is shown in Figure 4.34 for $E_n = 4$ MeV. Each incident neutron energy range and pre- and post-neutron emission quantities are treated separately. The centroid of a Gaussian fit to the TKE spectrum is the $\overline{TKE}$. The $\overline{TKE}$ varies with E_n and the trends are discussed in Chapter 5. The width of the TKE distribution, σ_{TKE}, also provides some hints about the physical properties of the compound nucleus.

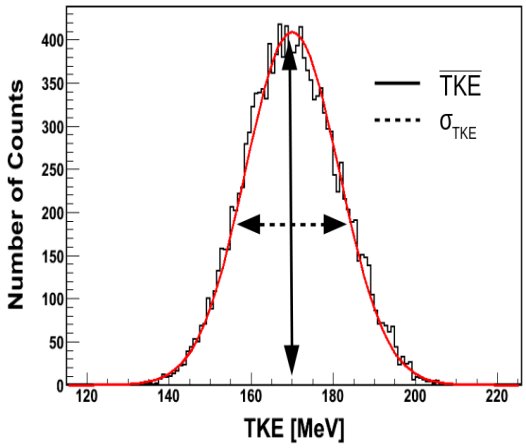

Figure 4.34: An example of a ^{238}U TKE distribution at $E_n = 4$ MeV fit with a Gaussian whose centroid is the average total kinetic energy ($\overline{TKE}$) and width is σ_{TKE}.

The mass yields are calculated pre- and post- neutron emission. Fission yields are normalized to 200%. Raw count spectra from either detector volume are added.

Both the $\overline{TKE}$ and the mass distributions are calculated in neutron energy ranges that maximize statistics and stay within the incident neutron energy resolution.

4.8 Uncertainty Quantification

The main sources of uncertainty in the 2E method is the way the prompt-neutron correction is handled. The variations in the valley region of the mass distributions were as much as 2% different at high E_n, depending on the method of neutron correction. The locations of the mass peaks did not shift but the amount of yield varied by as much as 0.3% yield percentage points.

We consider the final uncertainties on the energy to be the uncertainties on the linear energy calibration fit parameters, treated as anticorrelated uncertainties. Recall the uncertainties on the energy calibration fit parameters included uncertainties for the pulse height defect. Thus, the final uncertainty is,

$$\sigma_E^2 = \sigma_{C_a}^2 P_A^2 + \sigma_{C_b}^2 - 2P_A\sqrt{\sigma_{C_a}^2 \sigma_{C_b}^2}. \tag{4.41}$$

As a check, the calibration parameters were varied as much as 2 sigma, the 2E method was run, and the final $\overline{TKE}$ results shifted up and down by at most, 3 MeV, which is on par for an ionization detector energy measurement which will have between 0.5 to 1 % uncertainty on a typical fragment energy of 100 MeV.

CHAPTER 5

RESULTS

The following chapter contains results obtained from ^{238}U and ^{235}U measured kinetic energy data. First, the neutron energy dependent average total kinetic energy ($\overline{TKE}$) will be discussed in Section 5.1, followed by Section 5.2 on the evolution of the derived mass distributions with neutron energy. In Section 5.3, the correlations between the TKE and the fragment masses are considered. Throughout the sections, differences and similarities between the two isotopes will be compared and contrasted. Where applicable, the data are shown with models discussed in Chapter 2.

5.1 TKE as a Function of Neutron Energy

The change in the ^{238}U average total kinetic energy ($\overline{TKE}$) as a function of incident neutron energy (E_n) is shown in Figure 5.1 and Figure 5.2 for pre- and post-neutron emission respectively. The same quantities for ^{235}U are shown in Figure 5.4 and Figure 5.5. The $\overline{TKE}$ data is also available in tabular form in Table 5.1 for ^{238}U and Table 5.2 for ^{235}U. The vertical error bars represent the statistical errors while the horizontal error bars show the widths of the neutron energy bins which are always selected to be slightly larger than the neutron energy resolution.

The pre-neutron ^{238}U $\overline{TKE}$ is shown in Figure 5.1 along with the previous measurement [7] and phenomenological models [15], with [35] included in Figure 5.2. There are two physics reasons for the overall decrease in the $\overline{TKE}$. At higher incident neutron energies, the excitation energy of the compound nucleus typically increases. The extra excitation energy is however carried away by prompt neutrons and gammas compounded with higher probabilities of symmetric fission fragments which typically have lower Coulomb repulsion and thus, lower TKE. Exactly how the TKE is affected by fragment mass will be explored in Section 5.3.

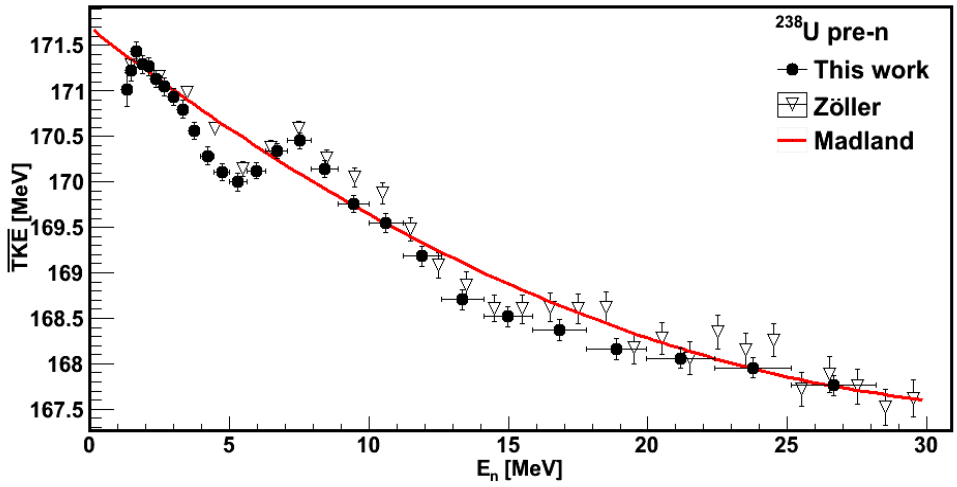

Figure 5.1: The $\overline{TKE}$ as a function of neutron energy for ^{238}U pre-neutron emission. [7] [15]

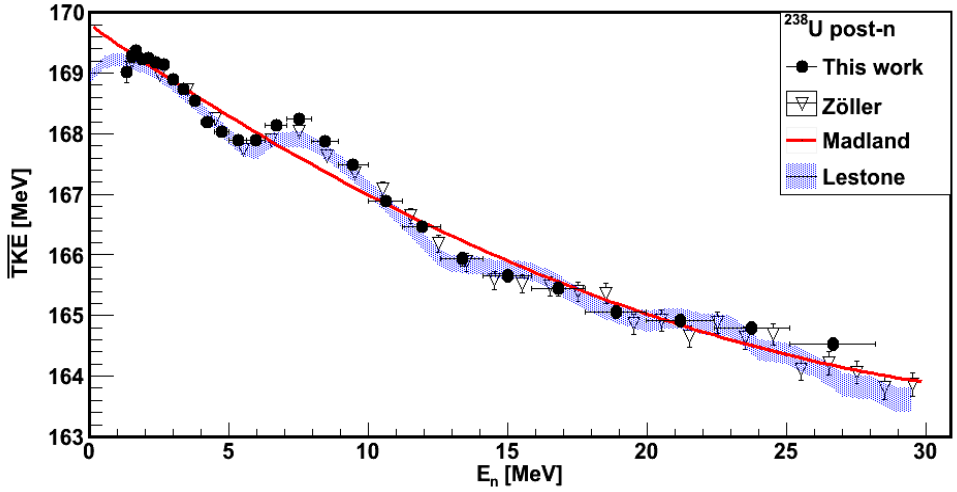

Figure 5.2: The $\overline{TKE}$ in this work as a function of neutron energy for ^{238}U post-neutron emission. A blue confidence band around the Lestone model is shown in blue [35] [15] [7].

The first peak at around $E_n = 1.7$ MeV establishes the fission threshold for ^{238}U. There is a prominent dip at 5.5 MeV, the second chance fission threshold, followed by a rise at 8 MeV where the second chance fission process dominates. This result suggests that as a new fission channel becomes probable, the extra excitation energy of the nucleus is dispersed by the pre-scission neutrons as the compound system deexcites into a lower energy state. The resulting compound nucleus has less energy available to transfer into the fragments so there is a drop in $\overline{TKE}$ with an initial fission channel opening.

The data are in good agreement with a previous unpublished measurement at WNR by Zöller et al. [7] at energies between $E_n = 1$ - 30 MeV. The overall shape of the data confirms a rough model fit made to the Zöller data by Madland [15]. The older data show more variation above 18 MeV, likely due to the arbitrary binning choice of 1 MeV increments, disregarding energy resolution of the neutron beam detector. This is also the case for the post-neutron emission energy dependent $\overline{TKE}$, shown in Figure 5.2. While the masses used in the calculations of the pre-neutron $\overline{TKE}$ are sensitive to the number of prompt neutrons, we do not account for the energy they carry away from the system.

Previous data analyzed with the 2E method is available for $E_n < 6$ MeV by Birgersson et al. [34] and Vives et al. [33] shown with the current measurement in Figure 5.3. Both experiments reported on pre-neutron emission data for ^{238}U, but used different neutron saw-tooth shapes than this work. These measurements were performed at quasi-monoenergetic neutron facilities. The systematic error on Frisch-gridded ionization chamber measurement of $\overline{TKE}$ is no more than 1%, which accounts for the difference in the absolute values of the measurements. Since the Birgersson study was of vibrational resonances, some low E_n points have been omitted. The shape of the Birgersson data confirms the decrease in TKE by about 300 keV between $E_n = 1.7$- 2.0. We do not observe the drop in TKE at $E_n = 3.8$ MeV which Vives et. al. suggest is due to pair breaking.

The pre-neutron ^{235}U $\overline{TKE}$ is shown in Figure 5.4 with a phenomenological model [15], output of the Los Alamos Dynamical Fission Model [66], and previous measurements [4] [5].

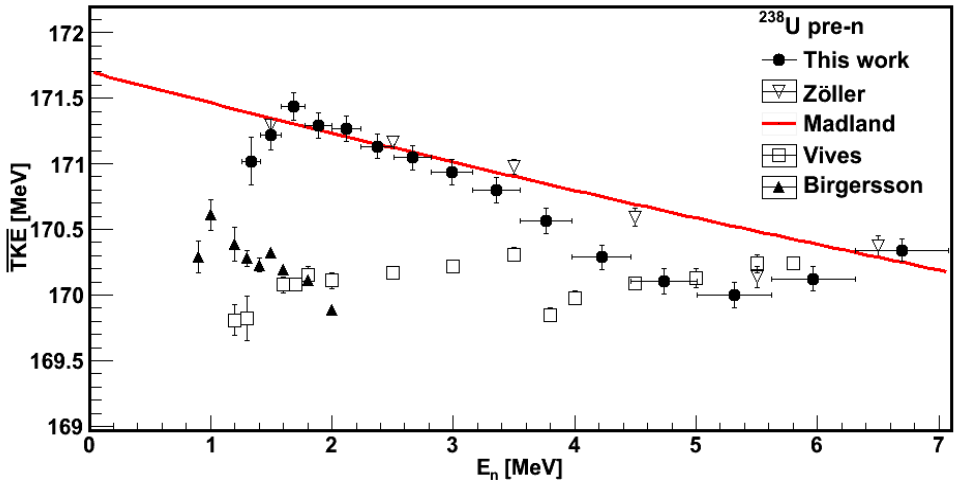

Figure 5.3: The $\overline{TKE}$ as a function of neutron energy for ^{238}U pre-neutron emission shown with previous 2E measurements at the low end of the neutron energy range [7] [33] [34] and the first-order model [15].

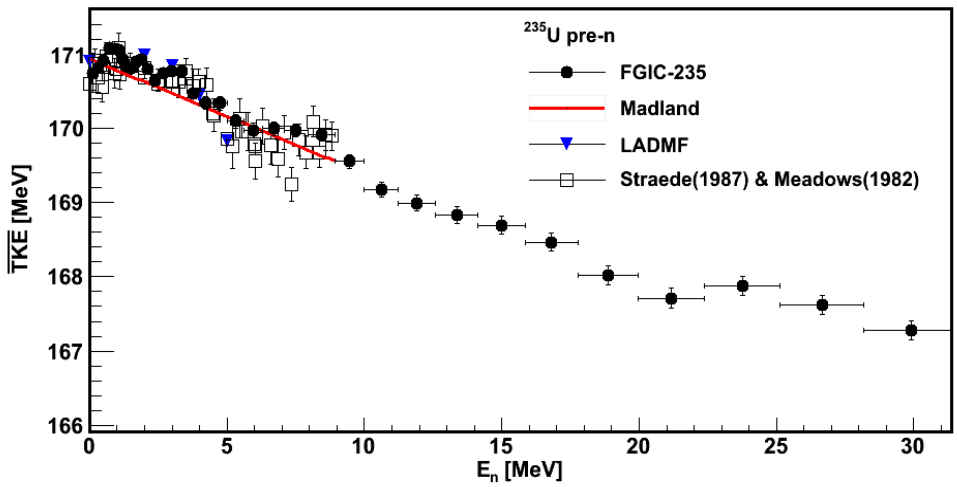

Figure 5.4: The $\overline{TKE}$ as a function of neutron energy for ^{235}U pre-neutron emission with two models [15] [66].

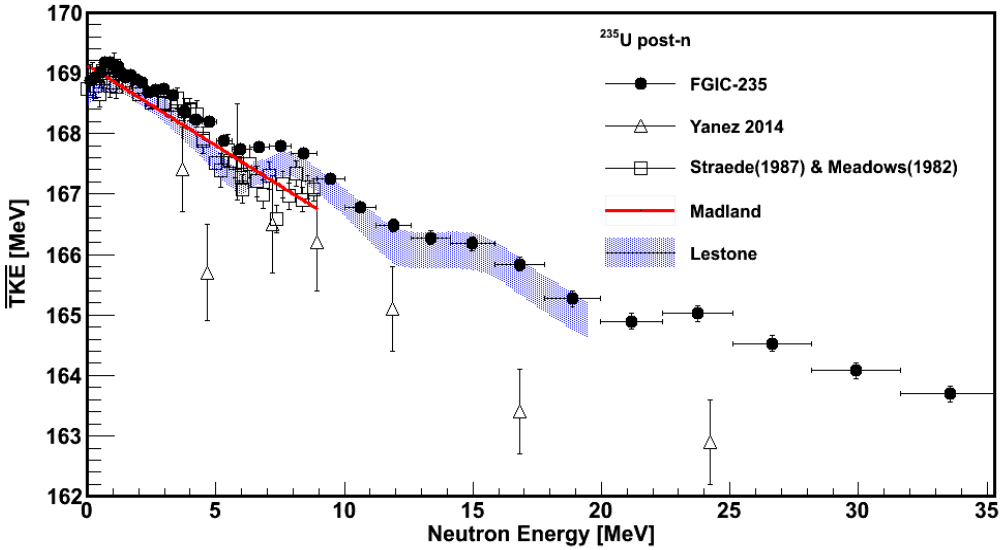

Figure 5.5: The $\overline{TKE}$ as a function of neutron energy for ^{235}U post-neutron emission [6] [15] [35] [5] [4].

The previous measurements [6] and an extended model [35] are included in Figure 5.5. The models are fits to other previous data sets between $E_n = 0-9$ MeV [4] [5]. The distributions of the previous data points were scattered [5] [4], but suggested the shape of the Lestone model, which this measurement confirms.

The turnover at $E_n = 0 - 3$ MeV is particularly interesting and was not confirmed in the previous data. A close-up of the low E_n region is shown in Figure 5.6 and Figure 5.7. Hints of the same behavior are seen in ^{238}U, but since that E_n is below the fission barrier, it is difficult to investigate experimentally. The LADFM model has predicted a turnover in ^{233}U [66]. The turnover behavior appears to be unique to uranium, as older data [67] and preliminary results using the same detector and WNR flight path for ^{239}Pu do not have this effect. As with ^{238}U, there is an overall decrease in the $\overline{TKE}$.

To verify that the shoulders in the $\overline{TKE}$ are correlated with multi-chance fission, we plot the $\overline{TKE}$ along with the evaluated cross sections from ENDF/B VII.1 [1], which are shown in Figure 5.8 and Figure 5.9. As discussed in Chapter 2, multiple chance fission occurs when the excited compound nucleus deexcites by emitting one or more neutrons prior to scission

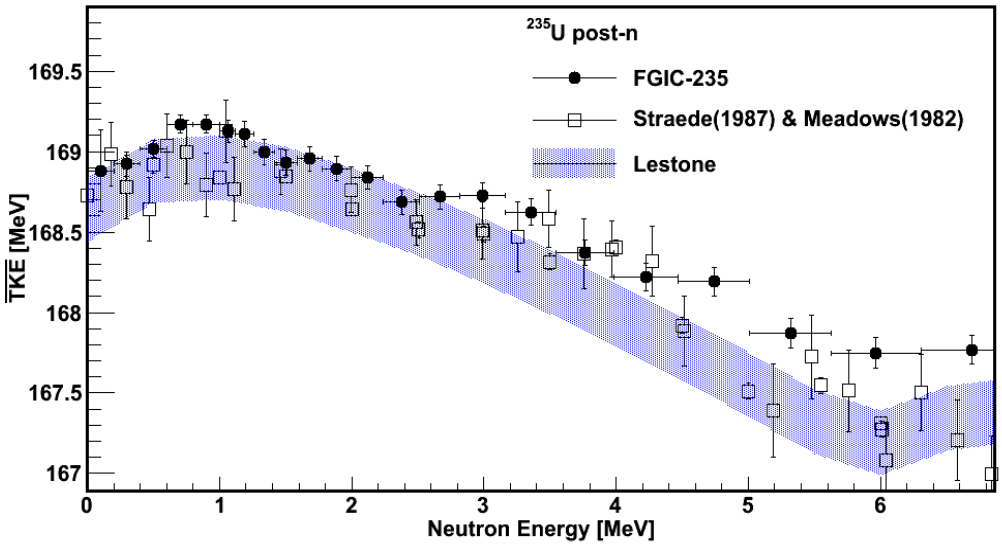

Figure 5.6: The $\overline{TKE}$ as a function of neutron energy for ^{235}U post-neutron emission zoomed in the show the "turnover" between $E_n = 0 - 3$ MeV. A blue confidence band around the Lestone model is shown in blue [35] with previous data [4] [5] .

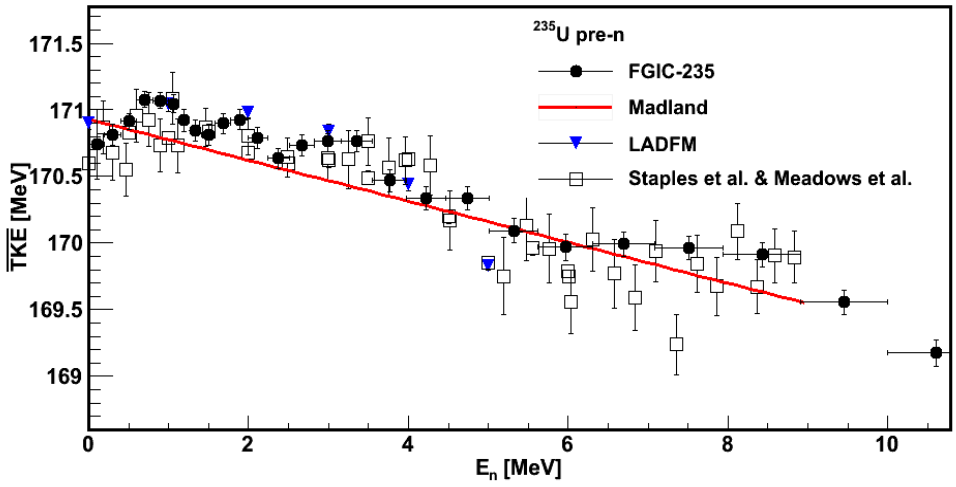

Figure 5.7: The $\overline{TKE}$ as a function of neutron energy for ^{235}U pre-neutron emission with fission models [66] [15] and previous measurements of [4] [5].

- the time when the two independent fragments form. The pre-scission neutrons carry away some of the system's energy, so we suppose that the compound nucleus is populating fewer energy states and the $\overline{TKE}$ initially rises. It drops again with increasing neutron energy after a multi-chance fission threshold because more states are getting populated and that energy gets carried away by prompt neutrons and gammas. In this data, structure in the TKE clearly shows these trends at the first chance fission threshold for both isotopes around $E_n = 6$ MeV.

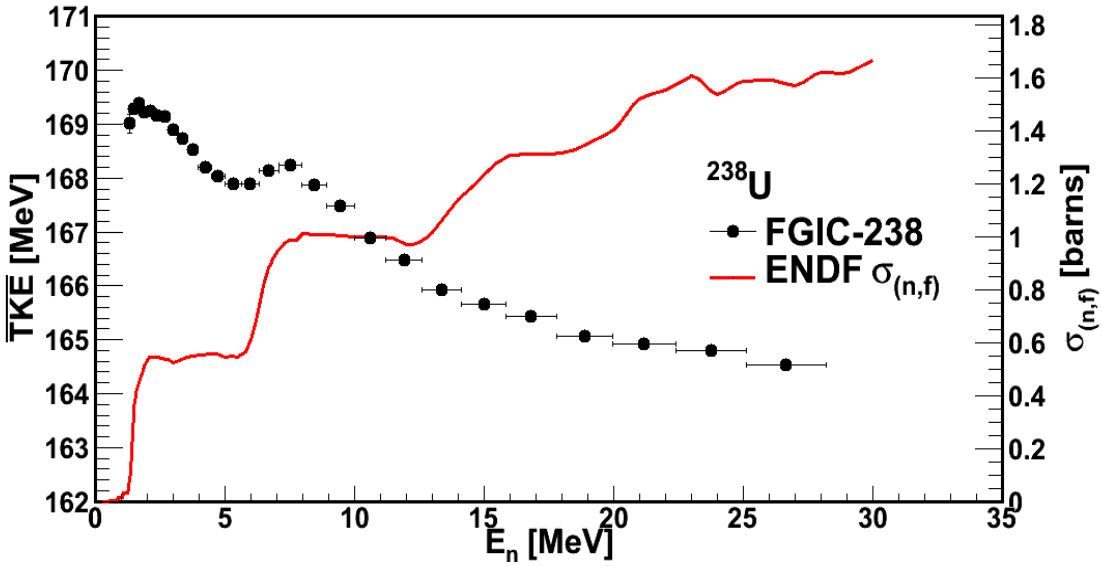

Figure 5.8: The $\overline{TKE}$ as a function of neutron energy for ^{238}U post-neutron emission plotted with the neutron-induced fission cross section, $\sigma_{(n,f)}$ (red). [1]

Perhaps the best evidence of the fissioning system's energy dependence is seen in the σ_{TKE} show in Figure 5.10. The σ_{TKE} for pre- and post-neutron emission for ^{235}U is shown in Figure 5.11 and Figure 5.12. These plots reveal the most variation at multichance fission thresholds. The observed TKE distribution is a superposition of TKE distributions for many pairs of fragments and fission pathways. With each muliple-chance fission pathway, more TKE distributions are present in the total distribution, resulting in an overall increase in σ_{TKE} with neutron energy. The structural changes in σ_{TKE} in both the pre- and post-neutron measurements at $E_n = 5.5$, 13, and 20 MeV suggest variations in the deformation

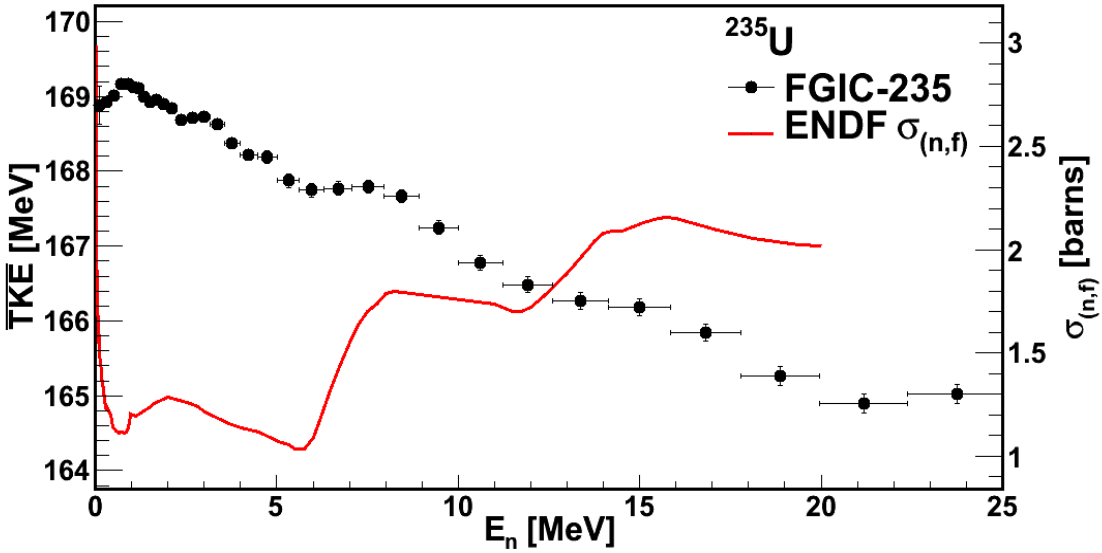

Figure 5.9: The $\overline{TKE}$ as a function of neutron energy for ^{238}U post-neutron emission plotted with the neutron-induced fission cross section, $\sigma_{(n,f)}$ (red). [1]

of the nucleus at the second, third, and fourth chance fission thresholds.

While a change in the $\overline{TKE}$ structure at third-chance fission threshold around $E_n = 12$ MeV and fourth-chance around $E_n = 20$ MeV is not present, there is clear structure at those values in the σ_{TKE} both pre- and post-neutron emission. It is not as clear in the older Zöller data, which has poorer energy resolution.

To better compare the σ_{TKE} behavior with the fission cross section, the two quantities are plotted together in Figure 5.12.

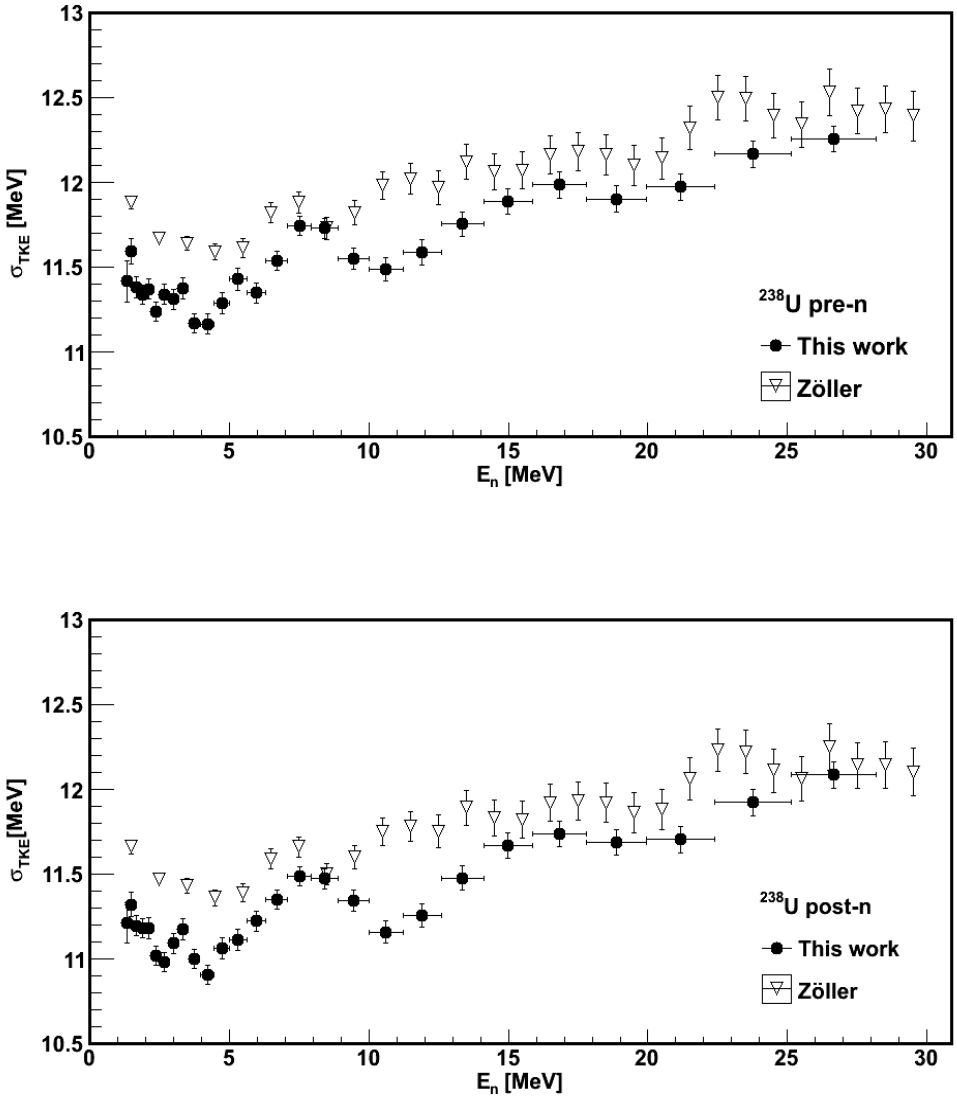

Figure 5.10: The variance σ_{TKE} in the TKE as a function of neutron energy for ^{238}U pre-neutron emission (top) and post-neutron emission (bottom) shown with existing data [7].

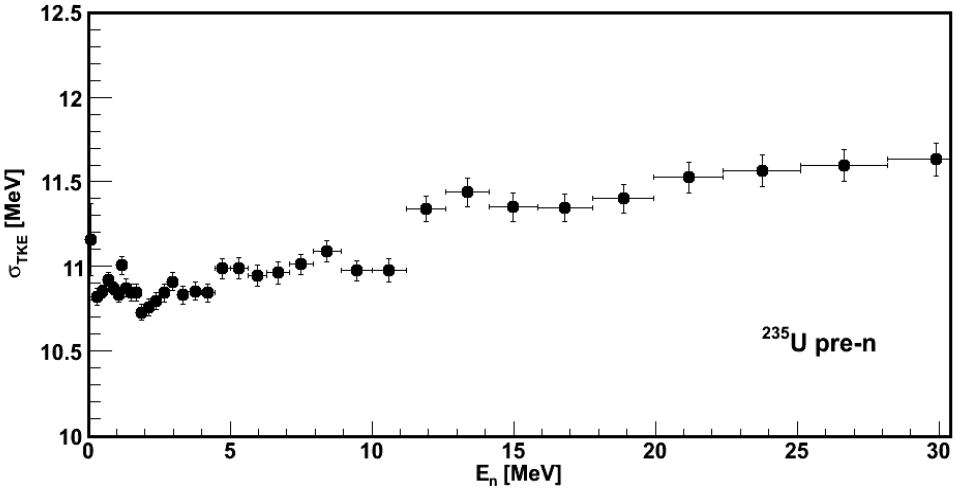

Figure 5.11: The variance in the TKE distribution as a function of neutron energy for ^{235}U pre-neutron emission.

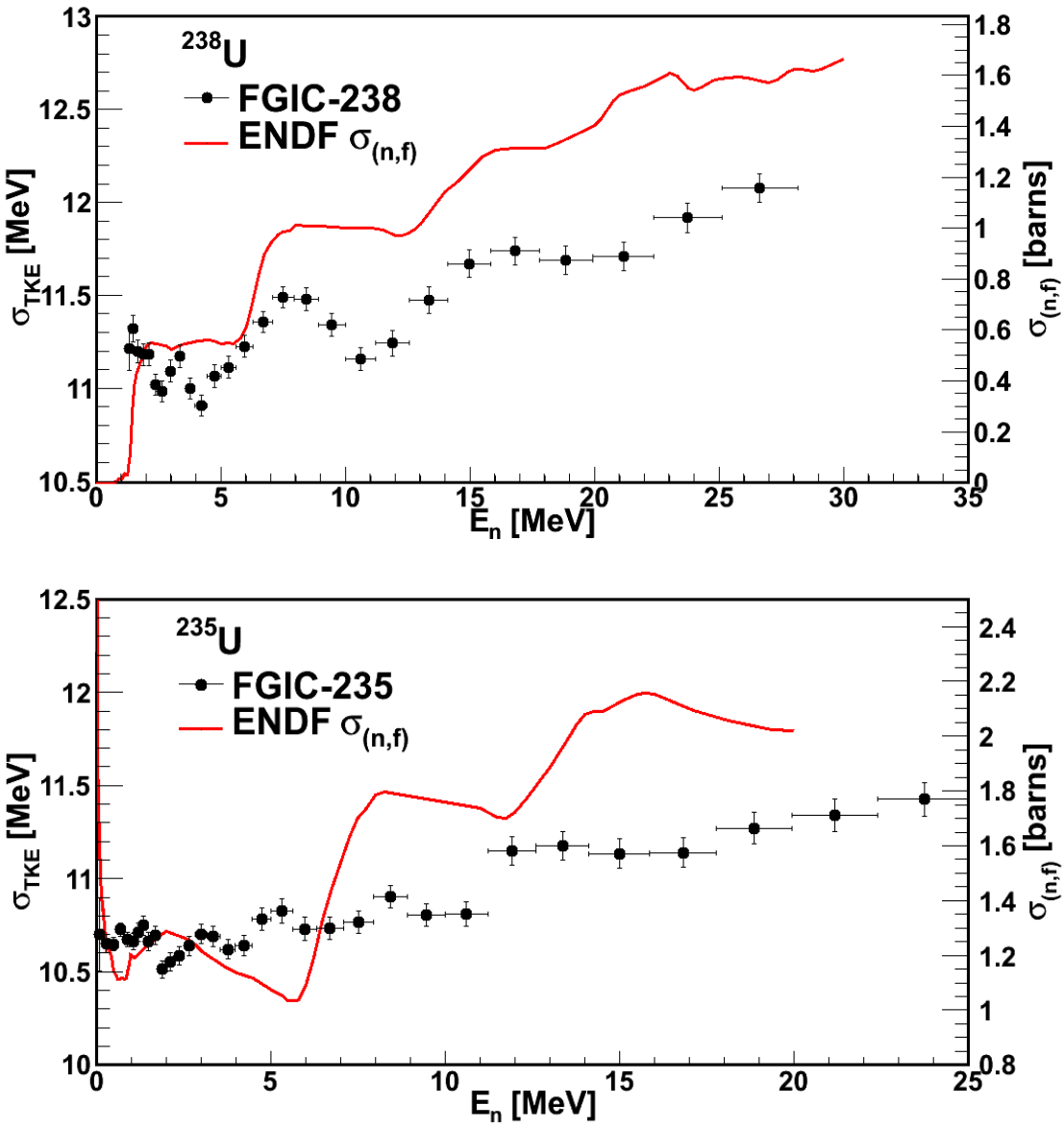

Figure 5.12: The σ_{TKE} as a function of neutron energy post-neutron emission plotted with the neutron-induced fission cross sections, $\sigma_{(n,f)}$ (red) for for ^{238}U (top) and for ^{235}U (bottom). [1]

Table 5.1: The pre- and post-neutron $\overline{TKE}$ and σ_{TKE} for ^{238}U. Uncertainties are statistical. Add ±0.5% for systematic uncertainties on the $\overline{TKE}$.

E_n [MeV]	pre-n $\overline{TKE}$ [MeV]	pre-n σ_{TKE} [MeV]	post-n $\overline{TKE}$ [MeV]	post-n σ_{TKE} [MeV]
1.3 - 1.5	171.02 ± 0.18	11.42 ± 0.12	169.02 ± 0.18	11.21 ± 0.12
1.5 - 1.7	171.22 ± 0.12	11.59 ± 0.08	169.29 ± 0.11	11.32 ± 0.07
1.7 - 1.9	171.44 ± 0.10	11.38 ± 0.06	169.38 ± 0.10	11.20 ± 0.06
1.9 - 2.1	171.29 ± 0.10	11.34 ± 0.06	169.23 ± 0.09	11.18 ± 0.06
2.1 - 2.4	171.27 ± 0.09	11.37 ± 0.06	169.25 ± 0.09	11.18 ± 0.06
2.4 - 2.7	171.13 ± 0.09	11.24 ± 0.06	169.17 ± 0.09	11.02 ± 0.06
2.7 - 3.0	171.05 ± 0.09	11.34 ± 0.06	169.15 ± 0.09	10.98 ± 0.06
3.0 - 3.4	170.94 ± 0.09	11.31 ± 0.06	168.89 ± 0.09	11.09 ± 0.06
3.4 - 3.8	170.80 ± 0.10	11.38 ± 0.06	168.74 ± 0.09	11.17 ± 0.06
3.8 - 4.2	170.57 ± 0.09	11.17 ± 0.06	168.54 ± 0.09	11.00 ± 0.06
4.2 - 4.7	170.29 ± 0.09	11.17 ± 0.06	168.20 ± 0.09	10.91 ± 0.06
4.7 - 5.3	170.11 ± 0.10	11.29 ± 0.06	168.04 ± 0.09	11.06 ± 0.06
5.3 - 6.0	170.00 ± 0.10	11.43 ± 0.06	167.90 ± 0.09	11.11 ± 0.06
6.0 - 6.7	170.12 ± 0.09	11.35 ± 0.06	167.89 ± 0.09	11.22 ± 0.06
6.7 - 7.5	170.34 ± 0.09	11.54 ± 0.06	168.13 ± 0.08	11.35 ± 0.06
7.5 - 8.4	170.45 ± 0.09	11.74 ± 0.06	168.24 ± 0.08	11.49 ± 0.06
8.4 - 9.5	170.15 ± 0.09	11.73 ± 0.06	167.87 ± 0.09	11.47 ± 0.06
9.5 - 10.6	169.76 ± 0.09	11.55 ± 0.06	167.48 ± 0.09	11.34 ± 0.06
10.6 - 11.9	169.55 ± 0.10	11.49 ± 0.07	166.89 ± 0.10	11.16 ± 0.06
11.9 - 13.4	169.19 ± 0.11	11.59 ± 0.07	166.47 ± 0.10	11.26 ± 0.07
13.4 - 15.0	168.70 ± 0.11	11.75 ± 0.07	165.93 ± 0.11	11.48 ± 0.07
15.0 - 16.8	168.52 ± 0.11	11.89 ± 0.07	165.66 ± 0.11	11.67 ± 0.07
16.8 - 18.9	168.37 ± 0.11	11.98 ± 0.08	165.44 ± 0.11	11.74 ± 0.07
18.9 - 21.2	168.16 ± 0.11	11.90 ± 0.08	165.06 ± 0.11	11.69 ± 0.08
21.2 - 23.8	168.06 ± 0.11	11.97 ± 0.08	164.91 ± 0.11	11.70 ± 0.08
23.8 - 26.7	167.96 ± 0.11	12.17 ± 0.08	164.80 ± 0.11	11.92 ± 0.08
26.7 - 30.0	167.76 ± 0.11	12.25 ± 0.08	164.53 ± 0.11	12.09 ± 0.08

Table 5.2: The pre- and post-neutron $\overline{TKE}$ and σ_{TKE} for ^{235}U. Uncertainties are statistical. Add ±0.5% for systematic uncertainties on the $\overline{TKE}$.

E_n [MeV]	pre-n $\overline{TKE}$ [MeV]	pre-n σ_{TKE} [MeV]	post-n $\overline{TKE}$ [MeV]	post-n σ_{TKE} [MeV]
0.0 - 0.2	168.9 ± 0.3	10.7 ± 0.2	170.7 ± 0.3	11.2 ± 0.2
0.2 - 0.4	168.92 ± 0.07	10.65 ± 0.05	170.81 ± 0.08	10.82 ± 0.05
0.4 - 0.6	169.02 ± 0.06	10.65 ± 0.04	170.91 ± 0.06	10.85 ± 0.04
0.6 - 0.8	169.17 ± 0.06	10.73 ± 0.04	171.08 ± 0.06	10.92 ± 0.04
0.8 - 1.0	169.17 ± 0.06	10.68 ± 0.04	171.07 ± 0.06	10.87 ± 0.04
1.0 - 1.1	169.13 ± 0.06	10.66 ± 0.04	171.05 ± 0.07	10.83 ± 0.04
1.1 - 1.3	169.11 ± 0.08	10.71 ± 0.05	170.92 ± 0.08	11.01 ± 0.05
1.3 - 1.4	169.00 ± 0.08	10.75 ± 0.05	170.84 ± 0.08	10.87 ± 0.05
1.4 - 1.6	168.93 ± 0.08	10.66 ± 0.05	170.82 ± 0.08	10.84 ± 0.05
1.6 - 1.8	168.96 ± 0.08	10.70 ± 0.05	170.90 ± 0.08	10.85 ± 0.05
1.8 - 2.0	168.90 ± 0.07	10.51 ± 0.05	170.93 ± 0.08	10.73 ± 0.05
2.0 - 2.2	168.84 ± 0.07	10.56 ± 0.05	170.79 ± 0.08	10.76 ± 0.05
2.2 - 2.5	168.69 ± 0.08	10.58 ± 0.05	170.64 ± 0.08	10.80 ± 0.05
2.5 - 2.8	168.72 ± 0.08	10.64 ± 0.05	170.74 ± 0.08	10.85 ± 0.05
2.8 - 3.2	168.73 ± 0.08	10.70 ± 0.05	170.76 ± 0.08	10.91 ± 0.05
3.2 - 3.5	168.63 ± 0.08	10.69 ± 0.05	170.76 ± 0.08	10.83 ± 0.05
3.5 - 4.0	168.37 ± 0.08	10.62 ± 0.05	170.47 ± 0.08	10.86 ± 0.05
4.0 - 4.5	168.22 ± 0.08	10.64 ± 0.05	170.34 ± 0.09	10.84 ± 0.06
4.5 - 5.0	168.19 ± 0.09	10.78 ± 0.06	170.34 ± 0.09	10.99 ± 0.06
5.0 - 5.6	167.87 ± 0.09	10.83 ± 0.06	170.09 ± 0.09	10.99 ± 0.06
5.6 - 6.3	167.75 ± 0.09	10.73 ± 0.06	169.97 ± 0.1	10.95 ± 0.06
6.3 - 7.1	167.77 ± 0.09	10.73 ± 0.06	169.99 ± 0.09	10.96 ± 0.06
7.1 - 7.9	167.80 ± 0.09	10.77 ± 0.06	169.96 ± 0.09	11.01 ± 0.06
7.9 - 8.9	167.67 ± 0.09	10.90 ± 0.06	169.91 ± 0.09	11.09 ± 0.06
8.9 - 10.0	167.25 ± 0.09	10.81 ± 0.06	169.56 ± 0.09	10.98 ± 0.06
10.0 - 11.2	166.80 ± 0.1	10.81 ± 0.07	169.18 ± 0.1	10.98 ± 0.07
11.2 - 12.6	166.48 ± 0.11	11.15 ± 0.08	168.99 ± 0.11	11.34 ± 0.08
12.6 - 14.1	166.27 ± 0.11	11.18 ± 0.08	168.83 ± 0.12	11.44 ± 0.08
14.1 - 15.8	166.18 ± 0.11	11.14 ± 0.08	168.69 ± 0.12	11.35 ± 0.08
15.8 - 17.8	165.84 ± 0.11	11.14 ± 0.08	168.47 ± 0.12	11.35 ± 0.08
17.8 - 20.0	165.27 ± 0.12	11.27 ± 0.08	168.02 ± 0.12	11.40 ± 0.08
20.0 - 22.4	164.89 ± 0.13	11.34 ± 0.09	167.71 ± 0.13	11.53 ± 0.09
22.4 - 25.1	165.03 ± 0.13	11.43 ± 0.09	167.87 ± 0.13	11.57 ± 0.09
25.1 - 28.2	164.53 ± 0.13	11.40 ± 0.09	167.62 ± 0.13	11.60 ± 0.09
28.2 - 31.6	164.08 ± 0.13	11.35 ± 0.09	167.28 ± 0.13	11.63 ± 0.10
31.6 - 35.5	163.70 ± 0.13	11.40 ± 0.1	166.90 ± 0.13	11.56 ± 0.10
35.5 - 39.8	163.55 ± 0.13	11.45 ± 0.1	166.93 ± 0.14	11.63 ± 0.10

5.2 Mass yields as a function of Neutron Energy

The pre- and post-neutron emission mass yields are presented as they evolve with neutron energy. In both regimes, we confirm that for the uranium isotopes, symmetric fission becomes much more likely at high incident neutron energies. First we consider post-neutron emission and compare it to ENDF evaluations of independent yields, which are important for applications. We next consider pre-neutron yields which provide valuable test cases and input data for fission modelers.

The post-neutron masses are comparable to the independent yield evaluation by England and Rider who define "Independent yields are taken from a calculated charge distribution model. The model independent yields are normalized so their sum equals the chain yields." [10] Chain yields are determined by radio-chemical methods. This comparison is shown in Figure 5.13 and Figure 5.14.

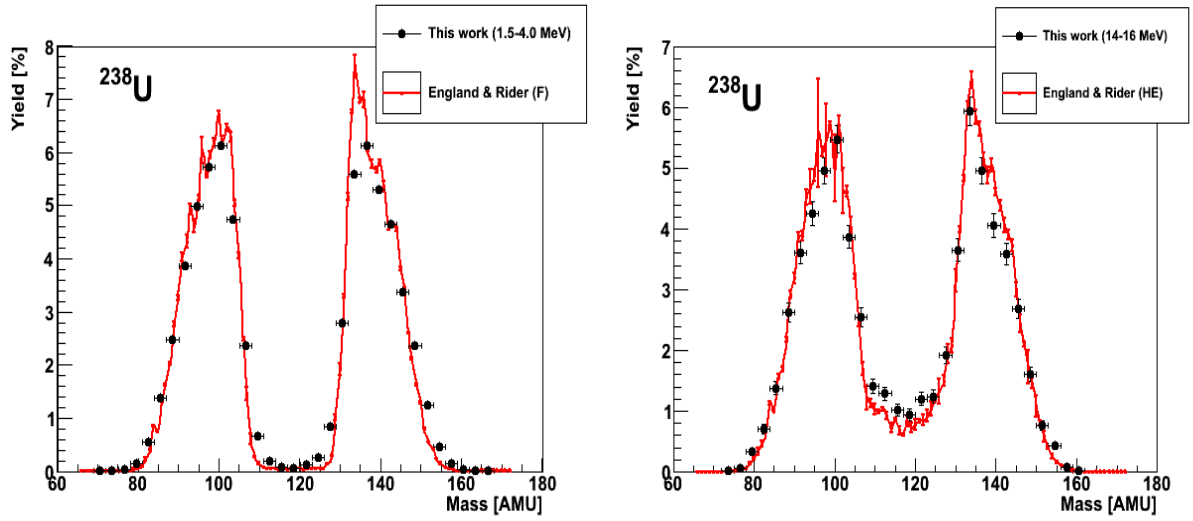

Figure 5.13: The England and Rider evaluation for independent yields are shown with the appropriate corresponding neutron energies [10]. "HE" denotes and energy bin from $E_n = 14 - 15$ MeV with the majority of events at 14.7 MeV. "F" denotes the fission neutron spectrum with additional pooling from $E_n = 0.5 - 2$ MeV. This work is shown for the E_n range beginning at 1.5 MeV because of the high fission threshold for ^{238}U.

The data show good agreement to the evaluation, however we do not observe the steep rise in the fission neutron energy range heavy peak at $A = 132$ AMU to 7.6% because it

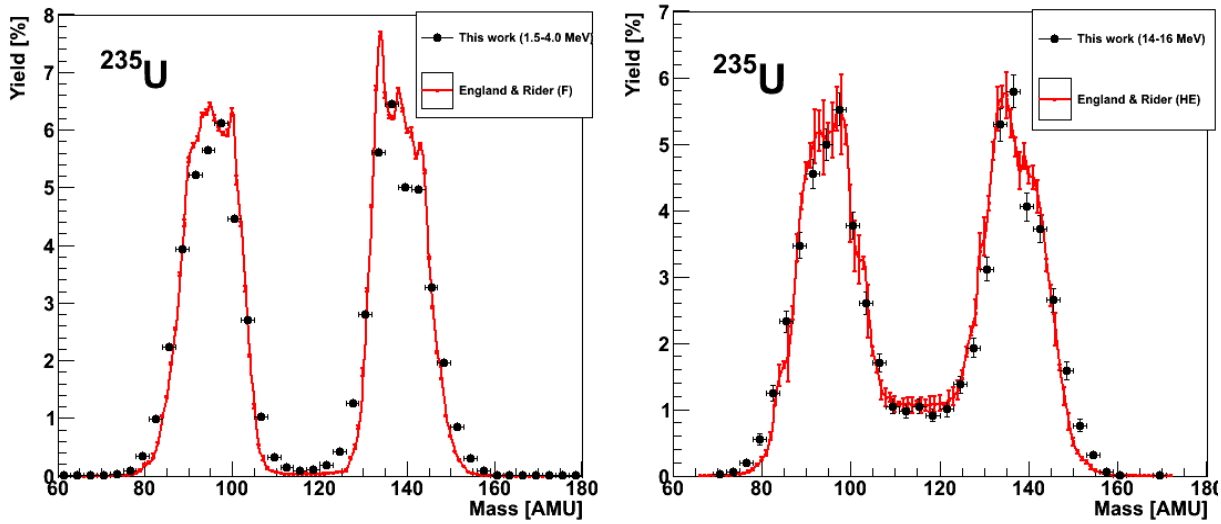

Figure 5.14: The England and Rider evaluation for independent yields are shown with the appropriate corresponding neutron energies [10]. "HE" denotes and energy bin from $E_n = 14 - 15$ MeV with the majority of events at 14.7 MeV. "F" denotes the fission neutron spectrum with additional pooling from $E_n = 0.5 - 2$ MeV. This work is shown for the E_n range beginning at 1.5 MeV because of the high fission threshold for ^{235}U.

is averaged out by the low mass resolution of this work. Agreement with the England and Rider evaluation validates this experimental method.

The mass yield landscape shows the expected trend of the filling of the valley region as incident neutron energy increases, shown in Figure 5.15. The yields are normalized to 200% for fragments at increasing neutron energies within range of the resolution of the detector.

Figure 5.16 shows a comparison to previously measured fragment yields pre-neutron emission, which show very good agreement. The data is plotted for 4 AMU energy resolution, consistent with limitations of the analysis method. At low energies, the present work predicts lower yield in the valley for $E_n = 1.5 - 2.5$ MeV possibly because the older work is plotted for a higher resolution than can be accounted for with the 2E method so some of the yield from the peaks could bleed into the valley. The older data is plotted with its full quoted 1 AMU resolution.

The pre-neutron emission yield plots in Figure 5.17, Figure 5.18, and Figure 5.19 show the full range of neutron energy covered by this experiment. A line is drawn between the

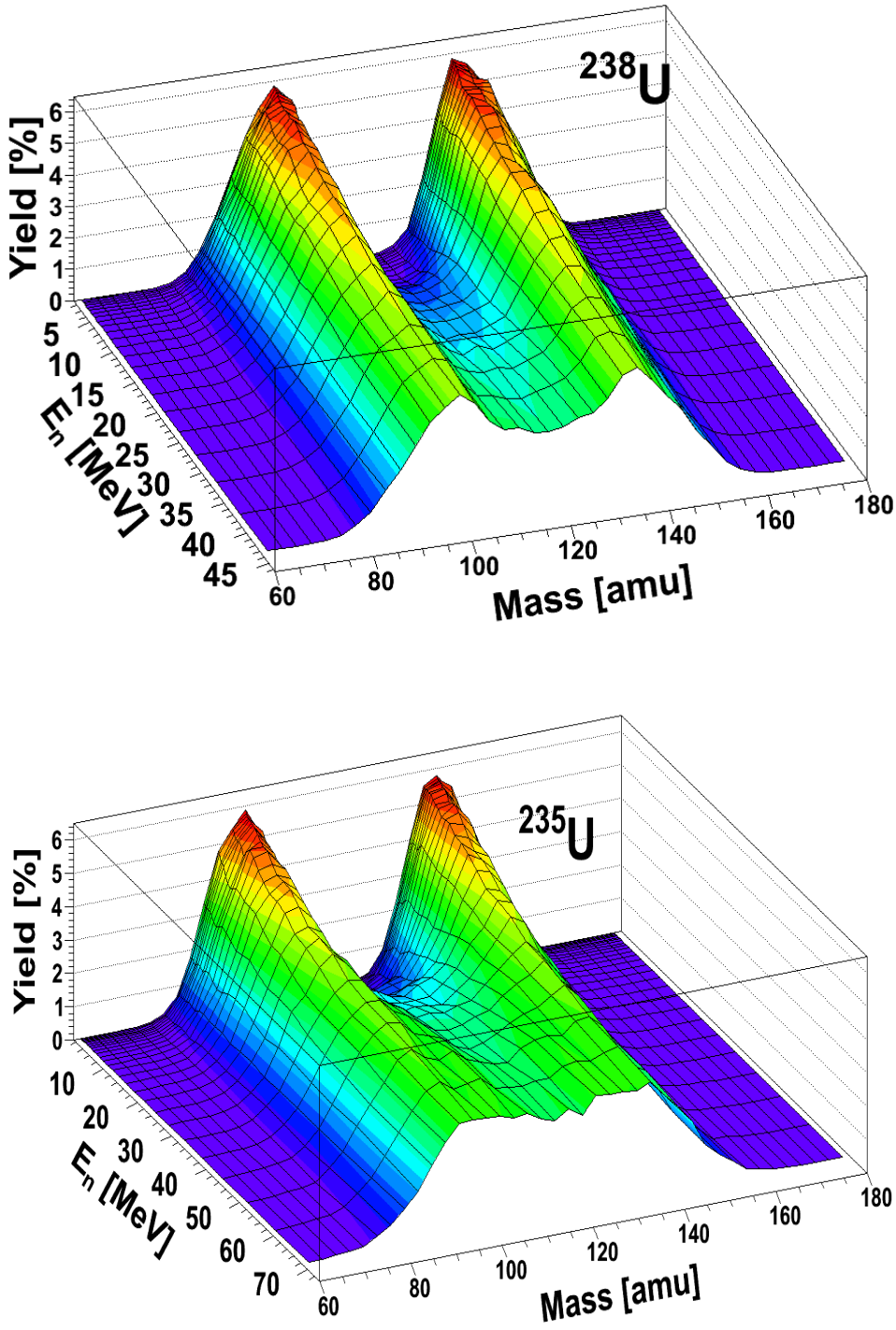

Figure 5.15: The fission fragment yield pre-neutron emission of ^{238}U (top) and ^{235}U (bottom) for calculated with 4-5 AMU resolution for incident neutron energies from 1.5 - 40 MeV. As expected, the valley fills in at higher incident neutron energies as fission becomes more symmetric. The color scale goes with the yield.

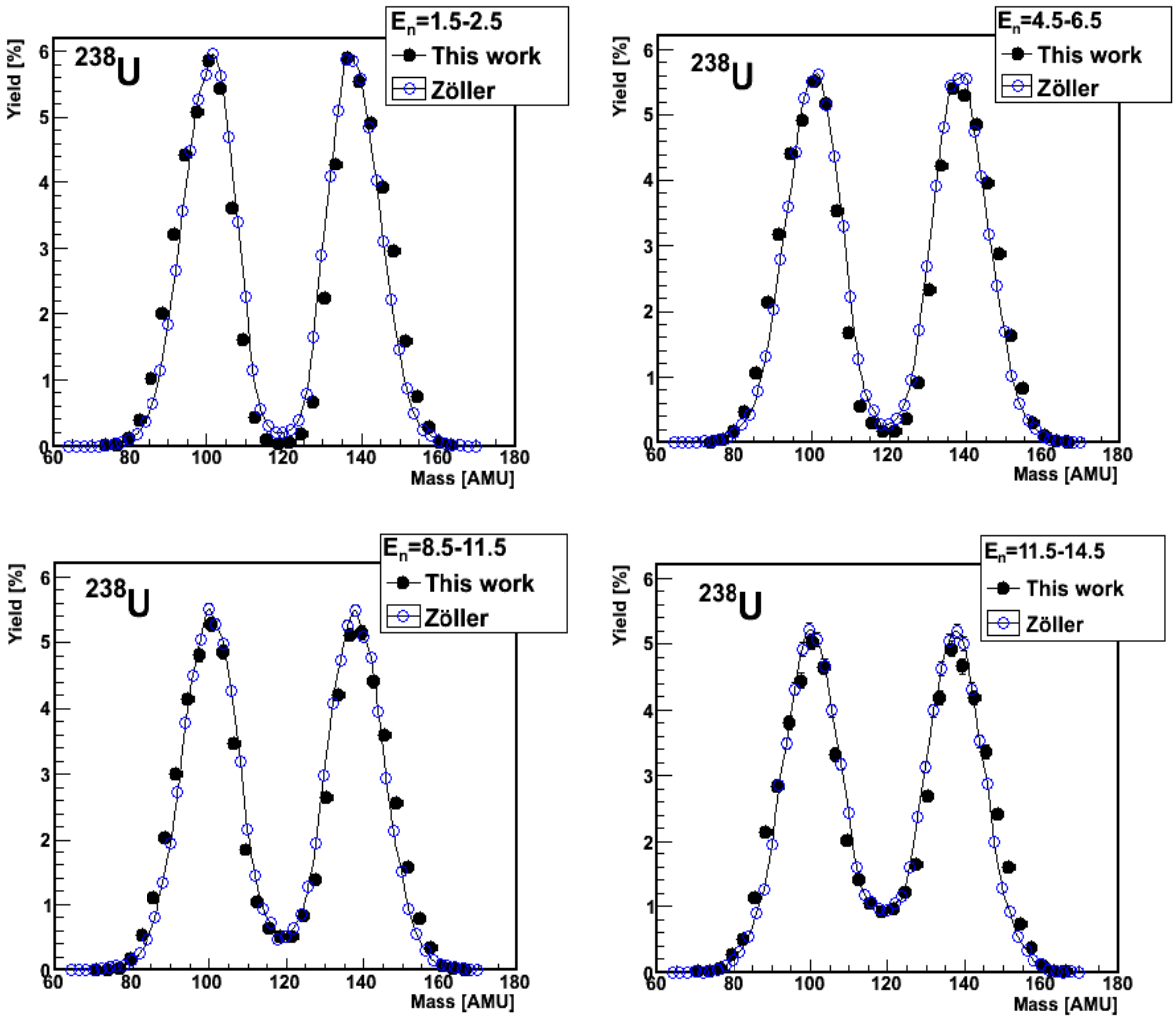

Figure 5.16: Comparison to Zöller data [7]. The line connecting the point guides the eye.

points to guide the eye. The legend shows the center of the neutron energy considered in each histogram range.

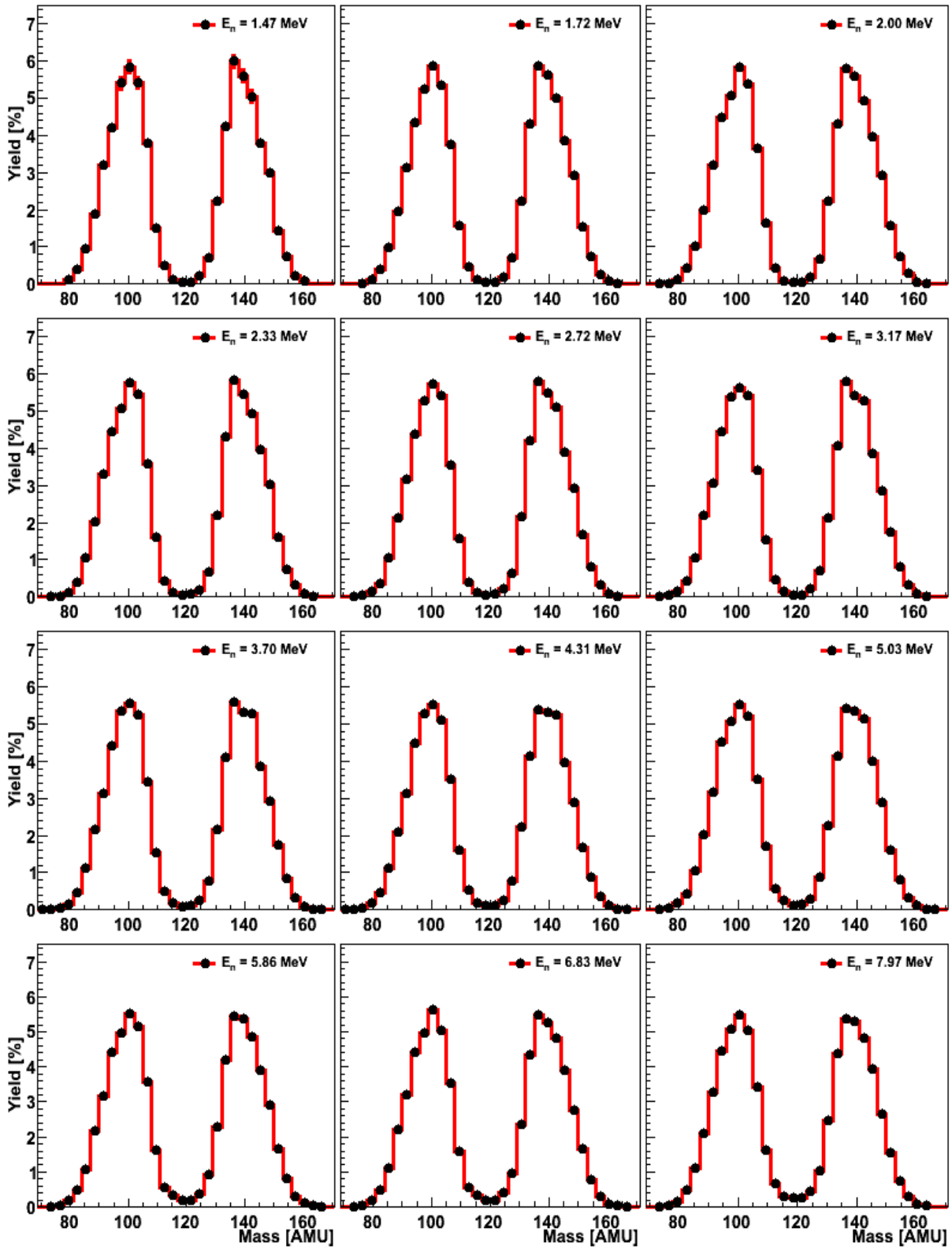

Figure 5.17: ^{238}U mass yield distributions pre-neutron emission from $E_n = 1.3 - 8.5$ MeV. Labeled E_n is the center of the incident neutron energy bin.

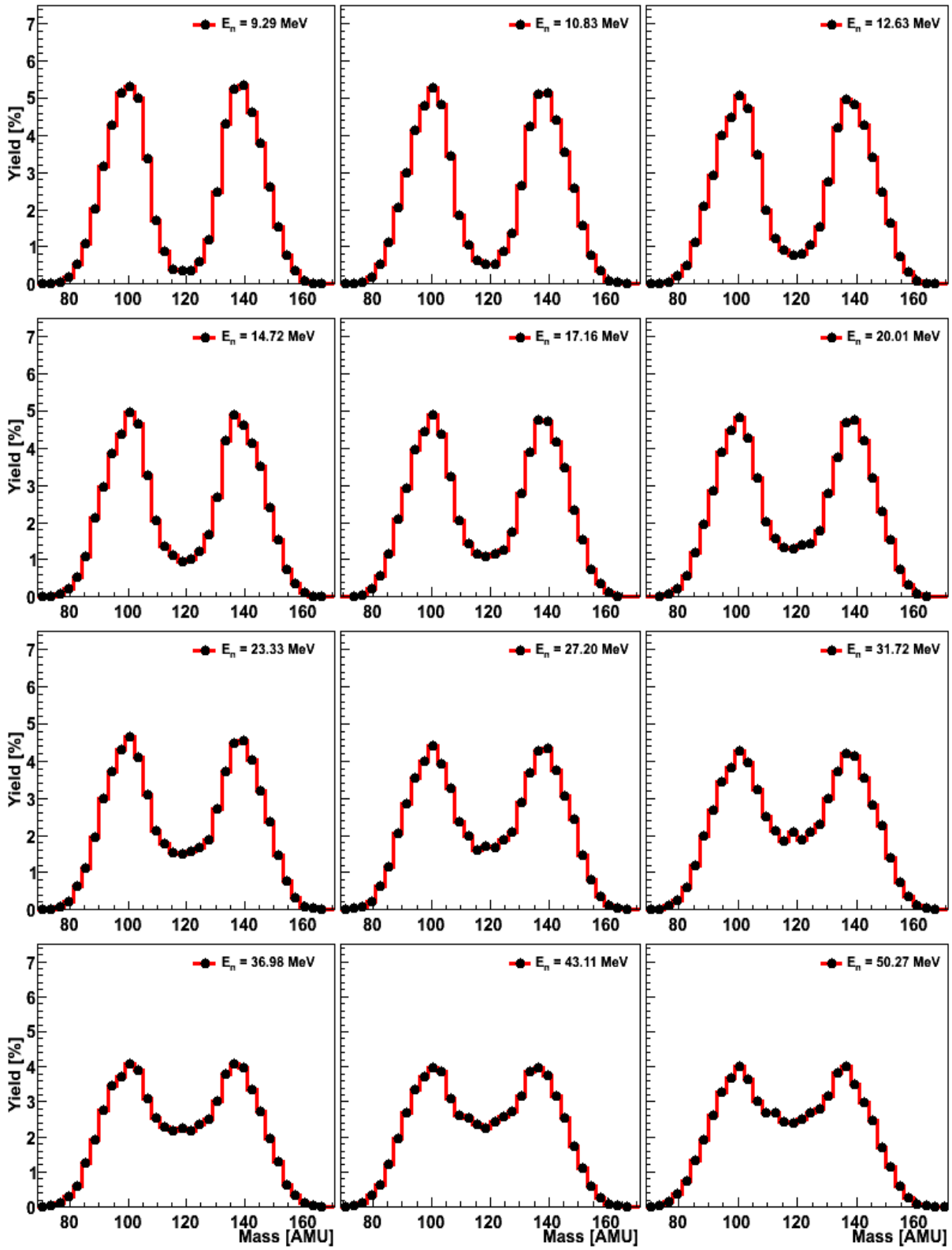

Figure 5.18: ^{238}U mass yield distributions pre-neutron emission from $E_n = 8.5 - 54$ MeV. Labeled E_n is the center of the incident neutron energy bin.

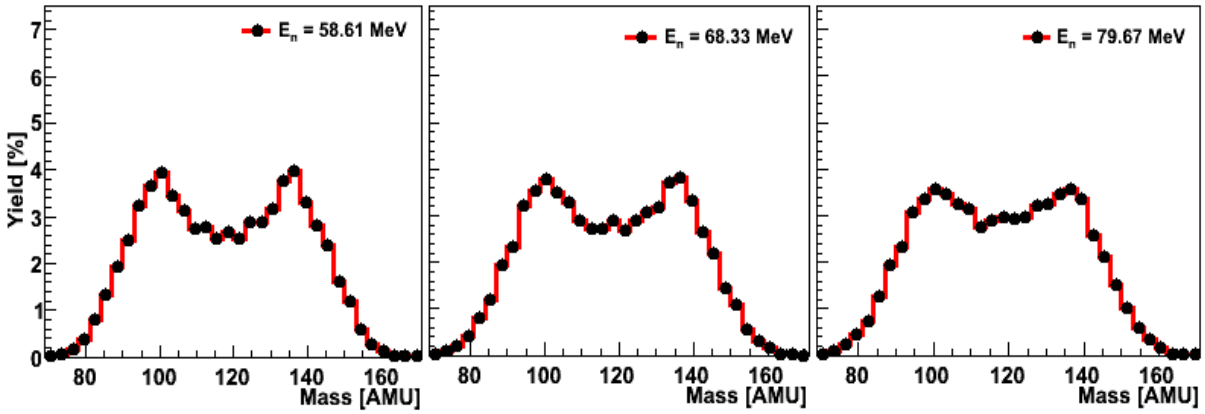

Figure 5.19: ^{238}U mass yield distributions pre-neutron emission from $E_n = 54 - 85$ MeV. Labeled E_n is the center of the incident neutron energy bin.

5.3 TKE as a function of mass yields

The net decrease in the $\overline{TKE}$ can be understood as how the kinetic energy is distributed to the individual fragments. Figure 5.20 and Figure 5.21 shows the TKE of the fragments as a function of the fragment mass. The plots look symmetric because there are two fragments per event whose mass must sum to that of the compound nucleus. Energy ranges were selected based on the location of the multi-chance fission thresholds. Qualitatively, the figures suggest that the more symmetric fragments have a lower TKE. The same is true for ^{235}U.

This observation is confirmed for both uranium isotopes in Figure 5.22 and Figure 5.23 for fragment masses between $A_H = 120 - 126$ AMU. This figure shows the $\overline{TKE}(A)$ for the heavy fragment. We can conclude that the $\overline{TKE}(A)$ peaks for asymmetric fragments found in abundance in the mass peaks, but drops for strongly symmetric or asymmetric fragments. A possible reason for lower symmetric fragment $\overline{TKE}(A)$ could be that the Coulomb repulsion is not as strong since the neck between symmetric fragments is longer at the moment of scission. There is a slight increase in $\overline{TKE}(A)$ with E_n for the symmetric fragments, however fragments greater than $A_H = 140$ AMU appear largely unaffected.

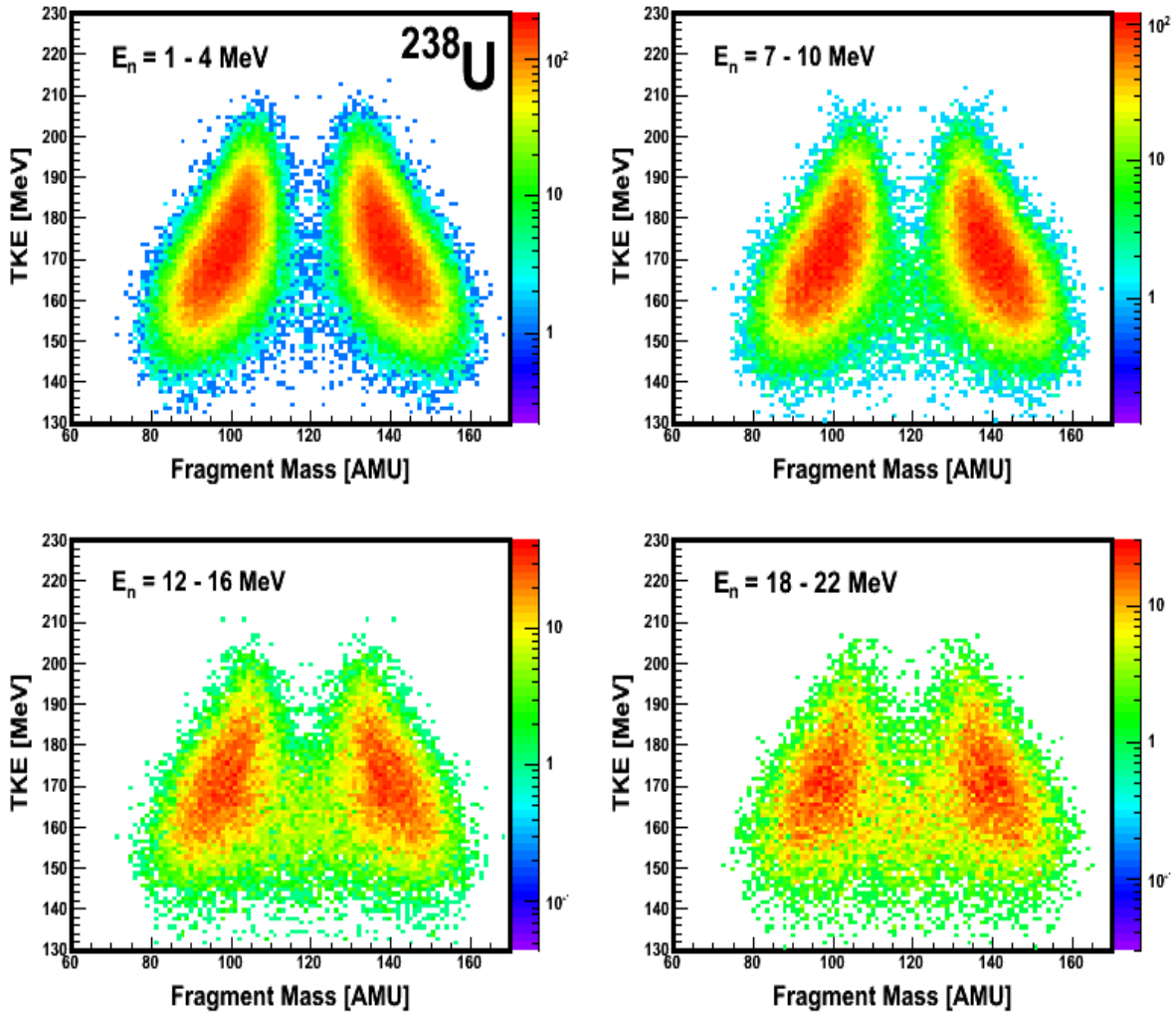

Figure 5.20: The distribution of TKE for ^{238}U fragment pairs within an energy range.

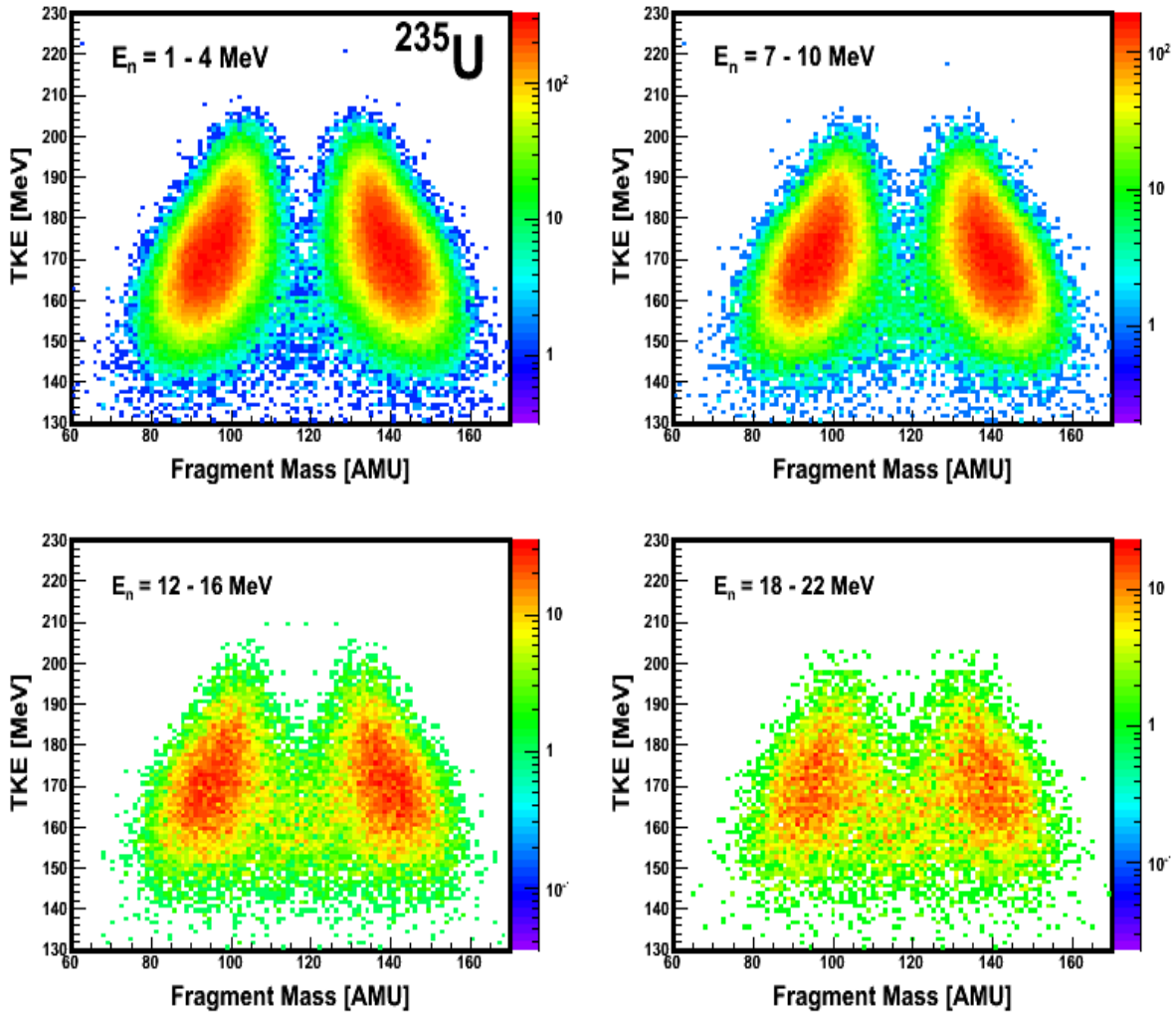

Figure 5.21: The distribution of TKE for ^{235}U fragment pairs within an energy range.

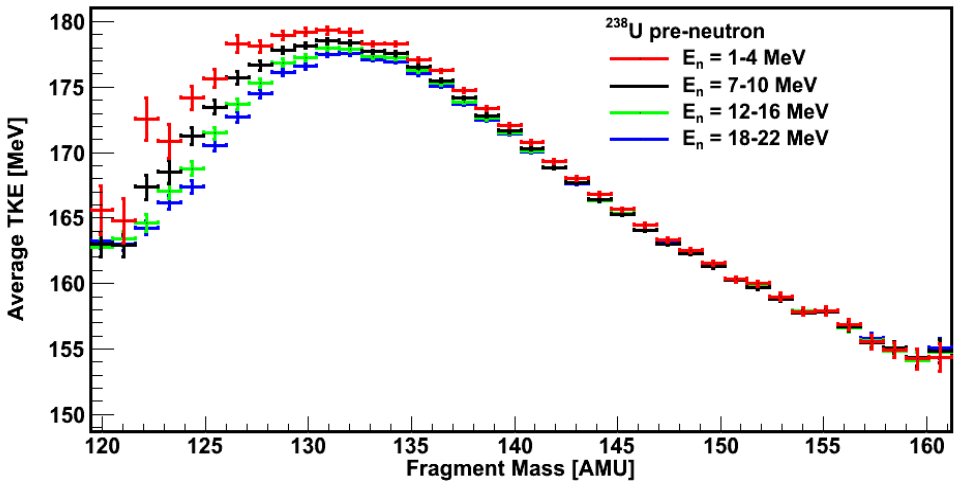

Figure 5.22: The distribution of $\overline{TKE}$ for the heavy fragment within a neutron energy range for ^{238}U shows clear evidence that symmetric and highly asymetric fragments have lower TKE.

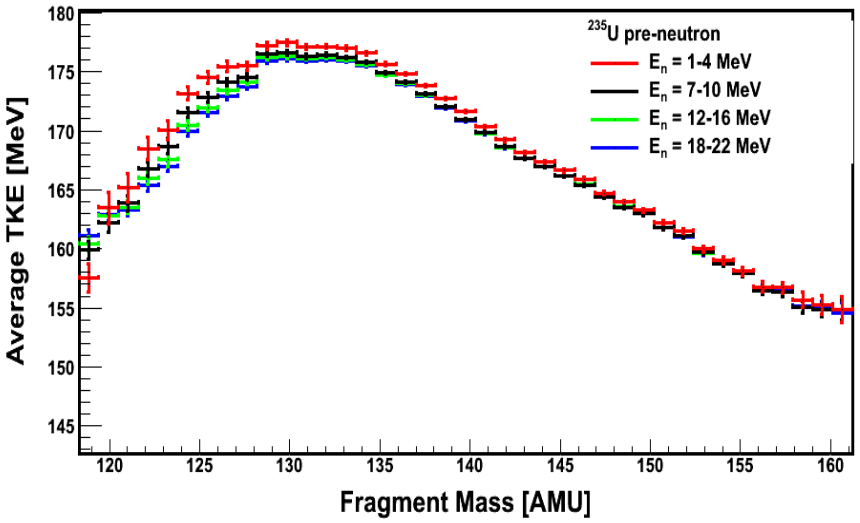

Figure 5.23: The distribution of $\overline{TKE}$ for the heavy fragment within a neutron energy range for ^{235}U shows clear evidence that symmetric and highly asymetric fragments have lower TKE.

CHAPTER 6

CONCLUSIONS

The purpose of this work was to measure correlated fission data to better understand how energy is distributed in a fissioning nuclear system. In this work, we extended the amount of available correlated mass and TKE data to incident neutron energies up to $E_n = 30$ MeV. Prior to this work, data was only available up to $E_n = 9$ MeV [4] [5] or had large uncertainties [6] for ^{235}U and only one unpublished measurement was available above $E_n = 7$ MeV for ^{238}U [7]. We established the over-all decreasing behavior of the average $\overline{TKE}$ with increasing E_n for both isotopes of uranium with a Frisch-gridded Ionization Chamber at the WNR white neutron source covering 100's of keV to 100's of MeV in a single measurement.

Some interesting features that came out of this work were the turnover between $E_n = 0-5$ MeV in the TKE, which had only been hinted at previously, was confirmed for ^{235}U and suggested for ^{238}U. The pre-neutron evaporation $\overline{TKE}$ also confirmed the turnover behavior for ^{235}U from the LADFM model [66]. Both isotopes' $\overline{TKE}$ exhibit structure at the multi-chance fission thresholds, namely the first- and second-chance thresholds, which confirms the validity of the Lestone model for post-neutron evaporation [35]. The width of the TKE distribution, σ_{TKE}, increased overall and showed structure corresponding to multi-chance fission thresholds at higher orders (third- and fourth-chance) than the $\overline{TKE}$. There is very little variation between the two uranium isotopes in the behavior of the observables.

The mass distributions both pre- and post-neutron evaporation were derived using the 2E method to about 4-5 AMU resolution. The results showed good agreement with England and Rider evaluations [10] for both ^{235}U and ^{238}U. The ^{238}U showed good agreement with previous measurement [7]. This was the first measurement to show the evolution of mass distributions with neutron energy in the 3D mass surface. Establishing how the mass and energy is distributed between the fragments remains one of the open questions in fission

physics.

Regarding the 2E method, incorporation of multi-chance fission probabilities into the 2E method is a novel feature. With better simulations of the probabilites and thresholds, this could likely be improved in future measurements. Further, the measurement of the neutron sawtooth should be a priority for experimentalists as that would enable better accuracy in 2E calculations. An improved method for the pulse height defect correction would further improve the energy resolution of the detector.

Further studies of $\overline{TKE}$ with E_n should include more nuclides. For example, establishing if other elements beside uranium that have the low energy turnover between E_n = 0-3 MeV have anything interesting in common (e.g. shape before fission or strength of the symmetric fission channel). Additional correlated TKE and fission fragment mass information would allow us to test the fission codes, fine tune the parameters, make a predictive fission model with both macroscopic and microscopic effects. More finely tuned models and simulations would, in turn, support civil and defense applications.

REFERENCES CITED

[1] M.B. Chadwick, M. Herman, P. Obloinsk, M.E. Dunn, Y. Danon, A.C. Kahler, D.L. Smith, B. Pritychenko, G. Arbanas, R. Arcilla, R. Brewer, D.A. Brown, R. Capote, A.D. Carlson, Y.S. Cho, H. Derrien, K. Guber, G.M. Hale, S. Hoblit, S. Holloway, T.D. Johnson, T. Kawano, B.C. Kiedrowski, H. Kim, S. Kunieda, N.M. Larson, L. Leal, J.P. Lestone, R.C. Little, E.A. McCutchan, R.E. MacFarlane, M. MacInnes, C.M. Mattoon, R.D. McKnight, S.F. Mughabghab, G.P.A. Nobre, G. Palmiotti, A. Palumbo, M.T. Pigni, V.G. Pronyaev, R.O. Sayer, A.A. Sonzogni, N.C. Summers, P. Talou, I.J. Thompson, A. Trkov, R.L. Vogt, S.C. van der Marck, A. Wallner, M.C. White, D. Wiarda, and P.G. Young. ENDF/B-VII.1 Nuclear Data for Science and Technology: Cross Sections, Covariances, Fission Product Yields and Decay Data. *Nuclear Data Sheets*, 112(12):2887 – 2996, 2011. ISSN 0090-3752. doi: 10.1016/j.nds.2011.11.002. URL `http://www.sciencedirect.com/science/article/pii/S009037521100113X`. Special Issue on ENDF/B-VII.1 Library.

[2] L. Meitner and O.R. Frisch. Disintegration of Uranium by Neutrons: A New Type of Nuclear Reaction. *Nature*, 143(3615):142 – 143, 1939. URL `http://www.nature.com/physics/looking-back/meitner/meitner.pdf`.

[3] R. Serber. *The Los Alamos Primer : The First Lectures on How to Build an Atomic Bomb*. University of California Press, Berkeley, 1992. ISBN 978-0-520-07576-4.

[4] J. W. Meadows and C. Budtz-Jørgensen. The Fission-Fragment Angular Distributions and Total Kinetic Energies for ^{235}U(n,f) from 0.18 to 8.34 MeV. Technical Report ANL/NDM-64, Argonne National Laboratory, January 1982.

[5] Ch. Straede, C. Budtz-Jrgensen, and H.-H. Knitter. ^{235}U(n, f) Fragment Mass-, Kinetic Energy- and Angular Distributions for Incident Neutron Energies Between Thermal and 6 MeV. *Nuclear Physics A*, 462(1):85 – 108, 1987. ISSN 0375-9474. doi: http://dx.doi.org/10.1016/0375-9474(87)90381-2. URL `http://www.sciencedirect.com/science/article/pii/0375947487903812`.

[6] R. Yanez, L. Yao, J. King, W. Loveland, F. Tovesson, and N. Fotiades. Excitation Energy Dependence of the Total Kinetic Energy Release in $^{235}u(n,f)$. *Phys. Rev. C*, 89: 051604, May 2014. doi: 10.1103/PhysRevC.89.051604. URL `http://link.aps.org/doi/10.1103/PhysRevC.89.051604`.

[7] C.M. Zöller. *Untersuchung der Neutroneninduzierten Spaltung von ^{238}U im Energiebereich von 1 MeV bis 500 MeV*. PhD thesis, Technische Hochschule Darmstadt, 1995. URL `http://www-win.gsi.de/charms/data.htm`.

[8] Florence Vivès. *Mesure des Propriétés des Fragments de Fission de la Réaction $^{238}U(n,f)$ /'a des Énergies de Neutrons Incidents Jusqu'à 5.8 MeV*. PhD thesis, L'Universite Bordeaux I, 1998.

[9] Evert Birgersson. *Determination of Binary Fission-Fragment Yields in the Reaction $^{251}Cf(n_{th},f)$ and Verification of Nuclear Reaction Theory Predictions of Fission-Fragment Distributions in the Reaction $^{238}U(n,f)$*. PhD thesis, Örebro universitet, 2007. URL `http://www.dissertations.se/about/Evert+Birgersson/`.

[10] T. R. England and B. F. Rider. ENDF-349: Evaluation and Compilation of Fission Product Yields 1993. Technical report, Los Alamos National Laboratory, October 1994. URL `http://ie.lbl.gov/fission/endf349.pdf`.

[11] M. B. Chadwick. Future Challenges for Nuclear Data Research in Fission. *Journal of the Korean Physical Society*, 59(2):752–754, 2011. doi: 10.3938/jkps.59.752. URL `http://jkps.kps.or.kr/home/journal/library/journal.asp?journaluid={3988%F18F-8ECC-44CC-8E51-3890B9091D41}&globalmenu=3&localmenu=10&journaltype={C0176%11D-EF29-4B30-8714-B9265F5AFF31}`.

[12] O. Hahn and F. Strassmann. Proof of the formation of active isotopes of barium from uranium and thorium irradiated with neutrons. *Die Naturwissenschaften*, 27(6):89–95, Februaury 1939. URL `http://www.chemteam.info/Chem-History/Hahn-fission-1939b/Hahn-Fission-1939b.html`.

[13] Niels Bohr and John Archibald Wheeler. The Mechanism of Nuclear Fission. *Phys. Rev.*, 56:426–450, Sep 1939. doi: 10.1103/PhysRev.56.426. URL `http://link.aps.org/doi/10.1103/PhysRev.56.426`.

[14] C. Wagemans. *The Nuclear Fission Process*. Taylor & Francis, Boca Raton, 1991. ISBN 9780849354342. URL `http://books.google.com/books?id=ERD3yypjgD4C`.

[15] D.G. Madland. Total Prompt Energy Release in the Neutron-Induced Fission of ^{235}U, ^{238}U, and ^{239}Pu. *Nuclear Physics A*, 772(34):113 – 137, 2006. ISSN 0375-9474. doi: 10.1016/j.nuclphysa.2006.03.013. URL `http://www.sciencedirect.com/science/article/pii/S0375947406001503`.

[16] Robert Vandenbosch. *Nuclear Fission*. Academic Press, New York, 1973. ISBN 0-12-710850-5.

[17] Kenneth S. Krane. *Introductory Nuclear Physics*. John Wiley and Sons, Inc., 1988.

[18] S. Bjørnholm and J. E. Lynn. The Double-Humped Fission Barrier. *Rev. Mod. Phys.*, 52:725–931, Oct 1980. doi: 10.1103/RevModPhys.52.725. URL `http://link.aps.org/doi/10.1103/RevModPhys.52.725`. from fredrik.

[19] David Lawrence Hill and John Archibald Wheeler. Nuclear Constitution and the Interpretation of Fission Phenomena. *Phys. Rev.*, 89:1102–1145, Mar 1953. doi: 10.1103/PhysRev.89.1102. URL http://link.aps.org/doi/10.1103/PhysRev.89.1102.

[20] S.G. Nilsson. Binding States of Iindividual Nucleons in Strongly Deformed Nuclei. *Kgl. Danske Videnskab. Selskab., Mat.-fys Medd.*, 29(16), Jan 1955. URL http://www.osti.gov/scitech/biblio/4376487.

[21] B. R. Mottelson and S. G. Nilsson. Classification of the Nucleonic States in Deformed Nuclei. *Phys. Rev.*, 99:1615–1617, Sep 1955. doi: 10.1103/PhysRev.99.1615. URL http://link.aps.org/doi/10.1103/PhysRev.99.1615.

[22] V.M. Strutinsky. Shell Effects in Nuclear Masses and Deformation Energies. *Nuclear Physics A*, 95(2):420 – 442, 1967. ISSN 0375-9474. doi: http://dx.doi.org/10.1016/0375-9474(67)90510-6. URL http://www.sciencedirect.com/science/article/pii/0375947467905106.

[23] V.M. Strutinsky. shells in Deformed Nuclei. *Nuclear Physics A*, 122(1):1 – 33, 1968. ISSN 0375-9474. doi: http://dx.doi.org/10.1016/0375-9474(68)90699-4. URL http://www.sciencedirect.com/science/article/pii/0375947468906994.

[24] Peter Möller and Arnold J. Sierk. Nuclear Physics: Into the Fission Valley. *Nature*, 422(6931):485–486, April 2003. ISSN 0028-0836. URL http://dx.doi.org/10.1038/422485a.

[25] Takatoshi Ichikawa, Akira Iwamoto, Peter Möller, and Arnold J. Sierk. Contrasting fission potential-energy structure of actinides and mercury isotopes. *Phys. Rev. C*, 86:024610, Aug 2012. doi: 10.1103/PhysRevC.86.024610. URL http://link.aps.org/doi/10.1103/PhysRevC.86.024610.

[26] Jørgen Randrup and Peter Möller. Brownian Shape Motion on Five-Dimensional Potential-Energy Surfaces : Nuclear Fission-Fragment Mass Distributions. *Phys. Rev. Lett.*, 106:132503, Mar 2011. doi: 10.1103/PhysRevLett.106.132503. URL http://link.aps.org/doi/10.1103/PhysRevLett.106.132503. current advances in fission.

[27] R. Bernard, H. Goutte, D. Gogny, and W. Younes. Microscopic and Nonadiabatic Schrödinger Equation Derived from the Generator Coordinate Method Based on Zero- and Two-Quasiparticle States. *Phys. Rev. C*, 84:044308, Oct 2011. doi: 10.1103/PhysRevC.84.044308. URL http://link.aps.org/doi/10.1103/PhysRevC.84.044308.

[28] W. Younes and D. Gogny. Microscopic Calculation of ^{240}Pu Scission with a Finite-range Effective Force. *Phys. Rev. C*, 80:054313, Nov 2009. doi: 10.1103/PhysRevC.80.054313. URL http://link.aps.org/doi/10.1103/PhysRevC.80.054313.

[29] Andrzej Staszczak, Jacek Dobaczewski, and Witold Nazarewicz. Fission Barriers of Superheavy Nuclei in the Skyrme-Hartree-Fock Model. *International Journal of Modern Physics E*, 15(02):302–310, 2006. doi: 10.1142/S0218301306004132. URL http://www.worldscientific.com/doi/abs/10.1142/S0218301306004132.

[30] A. J. Sierk. Dynamical model for fission fragment properties. Presentation LA-UR-14-27056, Los Alamos National Laboratory, Sept. 2014.

[31] E. Weissenberger, P. Geltenbort, A. Oed, F. Gnnenwein, and H. Faust. Energy Calibration of Surface barrier detectors for fission fragments. *Nuclear Instruments and Methods in Physics Research Section A: Accelerators, Spectrometers, Detectors and Associated Equipment*, 248(23):506 – 515, 1986. ISSN 0168-9002. doi: 10.1016/0168-9002(86)91041-7. URL http://www.sciencedirect.com/science/article/pii/0168900286910417.

[32] C. Budtz-Jrgensen, H.-H. Knitter, Ch. Straede, F.-J. Hambsch, and R. Vogt. A Twin Ionization Chamber for Fission Fragment Detection. *Nuclear Instruments and Methods in Physics Research Section A: Accelerators, Spectrometers, Detectors and Associated Equipment*, 258(2):209 – 220, 1987. ISSN 0168-9002. doi: http://dx.doi.org/10.1016/0168-9002(87)90058-1. URL http://www.sciencedirect.com/science/article/pii/0168900287900581.

[33] F. Vivès, F.-J. Hambsch, H. Bax, and S. Oberstedt. Investigation of the Fission Fragment Properties of the Reaction ^{238}U(n,f) at Incident Neutron Energies up to 5.8 MeV. *Nuclear Physics A*, 662(12):63 – 92, 2000. ISSN 0375-9474. doi: 10.1016/S0375-9474(99)00413-3. URL http://www.sciencedirect.com/science/article/pii/S0375947499004133.

[34] E. Birgersson, A. Oberstedt, S. Oberstedt, and F.-J. Hambsch. Properties of the Reaction ^{238}U at the Vibrational Resonances. *Nuclear Physics A*, 817(14):1 – 34, 2009. ISSN 0375-9474. doi: http://dx.doi.org/10.1016/j.nuclphysa.2008.12.001. URL http://www.sciencedirect.com/science/article/pii/S0375947408007975.

[35] J.P. Lestone and T.T. Strother. Energy Dependence of Plutonium and Uranium Average Fragment Total Kinetic Energies. *Nuclear Data Sheets*, 118(0):208 – 210, 2014. ISSN 0090-3752. doi: http://dx.doi.org/10.1016/j.nds.2014.04.038. URL http://www.sciencedirect.com/science/article/pii/S0090375214000684.

[36] P. Talou, B. Becker, T. Kawano, M. B. Chadwick, and Y. Danon. Advanced Monte Carlo Modeling of Prompt Fission Neutrons for Thermal and Fast Neutron-Induced Fission Reactions on ^{239}Pu. *Phys. Rev. C*, 83:064612, Jun 2011. doi: 10.1103/PhysRevC.83.064612. URL http://link.aps.org/doi/10.1103/PhysRevC.83.064612.

[37] J.P. Lestone. Energy Dependence of Plutonium Fission-Product Yields. *Nuclear Data Sheets*, 112(12):3120 – 3134, 2011. ISSN 0090-3752. doi: http://dx.doi.org/10.1016/j.nds.2011.11.008. URL http://www.sciencedirect.com/science/article/pii/S0090375211001190. Special Issue on ENDF/B-VII.1 Library.

[38] I. V. Ryzhov, S. G. Yavshits, G. A. Tutin, N. V. Kovalev, A. V. Saulski, N. A. Kudryashev, M. S. Onegin, L. A. Vaishnene, Yu. A. Gavrikov, O. T. Grudzevich, V. D. Simutkin, S. Pomp, J. Blomgren, M. Österlund, P. Andersson, R. Bevilacqua, J. P. Meulders, and R. Prieels. Fragment-Mass Distributions in Neutron-Induced Fission of ^{232}Th and ^{238}U at 33, 45, and 60 MeV. *Phys. Rev. C*, 83:054603, May 2011. doi: 10.1103/PhysRevC.83.054603. URL http://link.aps.org/doi/10.1103/PhysRevC.83.054603. uppsala. simutkin interviewed.

[39] C.W. Arnold, F. Tovesson, K. Meierbachtol, T. Bredeweg, M. Jandel, H.J. Jorgenson, A. Laptev, G. Rusev, D.W. Shields, M. White, R.E. Blakeley, D.M. Mader, and A.A. Hecht. Development of Position-Sensitive Time-of-Flight Spectrometer for Fission Fragment research. *Nuclear Instruments and Methods in Physics Research Section A: Accelerators, Spectrometers, Detectors and Associated Equipment*, July 2014. ISSN 01689002. doi: 10.1016/j.nima.2014.07.001. URL http://linkinghub.elsevier.com/retrieve/pii/S0168900214008432.

[40] M. Heffner, D.M. Asner, R.G. Baker, J. Baker, S. Barrett, C. Brune, J. Bundgaard, E. Burgett, D. Carter, M. Cunningham, J. Deaven, D.L. Duke, U. Greife, S. Grimes, U. Hager, N. Hertel, T. Hill, D. Isenhower, K. Jewell, J. King, J.L. Klay, V. Kleinrath, N. Kornilov, R. Kudo, A.B. Laptev, M. Leonard, W. Loveland, T.N. Massey, C. McGrath, R. Meharchand, L. Montoya, N. Pickle, H. Qu, V. Riot, J. Ruz, S. Sangiorgio, B. Seilhan, S. Sharma, L. Snyder, S. Stave, G. Tatishvili, R.T. Thornton, F. Tovesson, D. Towell, R.S. Towell, S. Watson, B. Wendt, L. Wood, and L. Yao. A time projection chamber for high accuracy and precision fission cross-section measurements. *Nuclear Instruments and Methods in Physics Research Section A: Accelerators, Spectrometers, Detectors and Associated Equipment*, 759(0):50 – 64, 2014. ISSN 0168-9002. doi: http://dx.doi.org/10.1016/j.nima.2014.05.057. URL http://www.sciencedirect.com/science/article/pii/S0168900214005890.

[41] S. Mosby, F. Tovesson, A. Couture, D.L. Duke, V. Kleinrath, R. Meharchand, K. Meierbachtol, J.M. O'Donnell, B. Perdue, D. Richman, and D. Shields. A Fission Fragment Detector for Correlated Fission Output Studies. *Nuclear Instruments and Methods in Physics Research Section A: Accelerators, Spectrometers, Detectors and Associated Equipment*, 757(0):75 – 81, 2014. ISSN 0168-9002. doi: http://dx.doi.org/10.1016/j.nima.2014.04.066. URL http://www.sciencedirect.com/science/article/pii/S0168900214004793.

[42] W. Loveland and J.D. Baker. Target Preparation for the Fission TPC. *Journal of Radioanalytical and Nuclear Chemistry*, 282(2):361–363, 2009. ISSN 0236-5731. doi: 10.1007/s10967-009-0146-z. URL http://dx.doi.org/10.1007/s10967-009-0146-z.

[43] Glenn Knoll. *Radiation Detection and Measurement*. John Wiley, Hoboken, N.J, 2010. ISBN 0470131489.

[44] A. Al-Adili, F.-J. Hambsch, R. Bencardino, S. Oberstedt, and S. Pomp. Ambiguities in the Grid-Inefficiency Correction for Frisch-Grid Ionization Chambers. *Nuclear Instruments and Methods in Physics Research Section A: Accelerators, Spectrometers, Detectors and Associated Equipment*, 673(0):116 – 121, 2012. ISSN 0168-9002. doi: 10.1016/j.nima.2011.01.088. URL http://www.sciencedirect.com/science/article/pii/S0168900211001744.

[45] V.A. Khriachkov, A.A. Goverdovski, V.V. Ketlerov, V.F. Mitrofanov, and N.N. Semenova. Direct experimental determination of frisch grid inefficiency in ionization chamber. *Nuclear Instruments and Methods in Physics Research Section A: Accelerators, Spectrometers, Detectors and Associated Equipment*, 394(12):261 – 264, 1997. ISSN 0168-9002. doi: 10.1016/S0168-9002(97)00601-3. URL http://www.sciencedirect.com/science/article/pii/S0168900297006013.

[46] A. G$\acute{}$o$\acute{}$ok, F.-J. Hambsch, A. Oberstedt, and S. Oberstedt. Application of the shockleyramo theorem on the grid inefficiency of frisch grid ionization chambers. *Nuclear Instruments and Methods in Physics Research Section A: Accelerators, Spectrometers, Detectors and Associated Equipment*, 664(1):289 – 293, 2012. ISSN 0168-9002. doi: http://dx.doi.org/10.1016/j.nima.2011.10.052. URL http://www.sciencedirect.com/science/article/pii/S0168900211020043.

[47] Paul W. Lisowski and Kurt F. Schoenberg. The Los Alamos Neutron Science Center. *Nuclear Instruments and Methods in Physics Research Section A: Accelerators, Spectrometers, Detectors and Associated Equipment*, 562(2):910 – 914, 2006. ISSN 0168-9002. doi: http://dx.doi.org/10.1016/j.nima.2006.02.178. URL http://www.sciencedirect.com/science/article/pii/S0168900206003792. Proceedings of the 7th International Conference on Accelerator Applications AccApp05 7th International Conference on Accelerator Applications.

[48] P.W. Lisowski, C.D. Bowman, G.J. Russel, and S.A. Wender. The Los Alamos National Laboratory Spallation Neutron Sources. *Nuclear Science and Engineering*, 106(2):208–218, OCT 1990. ISSN 0029-5639. URL http://library.lanl.gov/cgi-bin/getfile?00740250.pdf.

[49] A. Al-Adili. *Measurements of the ^{234}U(n,f) Reaction with a Frisch-Grid Ionization Chamber up to E_n=5 MeV*. PhD thesis, Uppsala University, Applied Nuclear Physics, 2013. URL http://uu.diva-portal.org/smash/record.jsf;jsessionid=78c8ce46c907adfe019b229282f9?searchId=1&pid=diva2:573126.

[50] F. Tovesson and T. S. Hill. Neutron Induced Fission Cross Section of ^{237}Np from 100 keV to 200 MeV. *Phys. Rev. C*, 75:034610, Mar 2007. doi: 10.1103/PhysRevC.75.034610. URL http://link.aps.org/doi/10.1103/PhysRevC.75.034610.

[51] John Taylor. *Modern Physics for Scientists and Engineers*. Pearson Prentice Hall, Upper Saddle River, NJ, 2004. ISBN 0-13-805715-x.

[52] John Taylor. *An Introduction to Error Analysis : The Study of Uncertainties in Physical Measurements*. University Science Books, Sausalito, Calif, 1997. ISBN 0935702423.

[53] J.B. Marion and F.C. Young. *Nuclear Reaction Analysis Graphs and Tables*. John Wiley, 1968. URL http://astro.uconn.edu/Info/MaryonYoung_Nuclear_Reaction_Analysis.pdf.

[54] P. Talou. "private communication". Jan. 2015.

[55] B. Jurado and K.-H. Schmidt. A General Description of Fission Observables (GEF), version 2015/1.1, Jan. 2015. URL http://www.khs-erzhausen.de/GEF.html.

[56] James Terrell. Neutron Yields from Individual Fission Fragments. *Phys. Rev.*, 127: 880–904, Aug 1962. doi: 10.1103/PhysRev.127.880. URL http://link.aps.org/doi/10.1103/PhysRev.127.880.

[57] Arthur C. Wahl. Nuclear-Charge Distribution and Delayed-Neutron Yields for Thermal-Neutron-Induced Fission of ^{235}U, ^{233}U, and ^{239}Pu and for Spontaneous Fission of ^{252}Cf. *Atomic Data and Nuclear Data Tables*, 39(1):1 – 156, 1988. ISSN 0092-640X. doi: http://dx.doi.org/10.1016/0092-640X(88)90016-2. URL http://www.sciencedirect.com/science/article/pii/0092640X88900162.

[58] A. A. Naqvi, F. Käppeler, F. Dickmann, and R. Müller. Fission Fragment Properties in fast-neutron-induced fission of ^{237}np. *Phys. Rev. C*, 34:218–225, Jul 1986. doi: 10.1103/PhysRevC.34.218. URL http://link.aps.org/doi/10.1103/PhysRevC.34.218.

[59] R. Müller, A. A. Naqvi, F. Käppeler, and F. Dickmann. Fragment velocities, energies, and masses from fast neutron induced fission of ^{235}U. *Phys. Rev. C*, 29:885–905, Mar 1984. doi: 10.1103/PhysRevC.29.885. URL http://link.aps.org/doi/10.1103/PhysRevC.29.885.

[60] Karl-Heinz Schmidt and Beatriz Jurado. Entropy Driven Excitation Energy Sorting in Superfluid Fission Dynamics. *Phys. Rev. Lett.*, 104:212501, May 2010. doi: 10.1103/PhysRevLett.104.212501. URL http://link.aps.org/doi/10.1103/PhysRevLett.104.212501.

[61] Karl-Heinz Schmidt and Beatriz Jurado. Final Excitation Energy of Fission Fragments. *Phys. Rev. C*, 83:061601, Jun 2011. doi: 10.1103/PhysRevC.83.061601. URL http://link.aps.org/doi/10.1103/PhysRevC.83.061601.

[62] C. Manailescu, A. Tudora, F.-J. Hambsch, C. Morariu, and S. Oberstedt. Possible reference method of total excitation energy partition between complementary fission fragments. *Nuclear Physics A*, 867(1):12 – 40, 2011. ISSN 0375-9474. doi: http://dx.doi.org/10.1016/j.nuclphysa.2011.08.001. URL http://www.sciencedirect.com/science/article/pii/S0375947411005641.

[63] A. Al-Adili, F.-J. Hambsch, S. Pomp, and S. Oberstedt. Impact of Prompt-Neutron Corrections on Final Fission-Fragment Distributions. *Phys. Rev. C*, 86:054601, Nov 2012. doi: 10.1103/PhysRevC.86.054601. URL http://link.aps.org/doi/10.1103/PhysRevC.86.054601.

[64] G. Simon, J. Trochon, F. Brisard, and C. Signarbieux. Pulse Height Defect in an Ionization Chamber Investigated by Cold Fission Measurements. *Nuclear Instruments and Methods in Physics Research Section A: Accelerators, Spectrometers, Detectors and Associated Equipment*, 286(12):220 – 229, 1990. ISSN 0168-9002. doi: http://dx.doi.org/10.1016/0168-9002(90)90224-T. URL http://www.sciencedirect.com/science/article/pii/016890029090224T.

[65] F.-J. Hambsch, J. Van Aarle, and R. Vogt. Is there a pulse height defect for methane? *Nuclear Instruments and Methods in Physics Research Section A: Accelerators, Spectrometers, Detectors and Associated Equipment*, 361(12):257 – 262, 1995. ISSN 0168-9002. doi: http://dx.doi.org/10.1016/0168-9002(95)00190-5. URL http://www.sciencedirect.com/science/article/pii/0168900295001905.

[66] A. J. Sierk. "private communication". April 2015.

[67] N.I. Akimov, V.G. Vorobéva, and V.N. Kabenin. Effect of Excitation Energy on Yields and Kinetic Energies of Fragments at the Fission of ^{239}Pu by Neutrons. *Yadern. Fiz.*, 13:484–91, March 1971.